DEPARTMENT OF AEROSPACE ENGINEERING
COLLEGE OF ENGINEERING & TECHNOLOGY
OLD DOMINION UNIVERSITY
NORFOLK, VIRGINIA 23529

NUMERICAL SIMULATION OF THE NONLINEAR RESPONSE OF COMPOSITE PLATES UNDER COMBINED THERMAL AND ACOUSTIC LOADING

By

Chuh Mei, Principal Investigator
Jayashree Moorthy, Graduate Research Assistant

Final Report
For the period ended March 15, 1995

Prepared for
National Aeronautics and Space Administration
Langley Research Center
Hampton, VA 23681-0001

Under
Research Grant NAG-1-1358
Travis L. Turner, Technical Monitor
FMAD-Structural Acoustics Branch

Submitted by the
Old Dominion University Research Foundation
P.O. Box 6369
Norfolk, VA 23518

January 1995

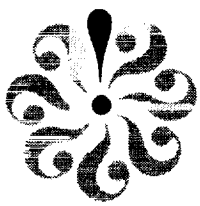

ABSTRACT

NUMERICAL SIMULATION OF THE NONLINEAR RESPONSE OF COMPOSITE PLATES UNDER COMBINED THERMAL AND ACOUSTIC LOADING

Jayashree Moorthy[1] and Chuh Mei[2]

A time-domain study of the random response of a laminated plate subjected to combined acoustic and thermal loads is carried out. The features of this problem also include given uniform static inplane forces. The formulation takes into consideration a possible initial imperfection in the flatness of the plate. High decibel sound pressure levels along with high thermal gradients across thickness drive the plate response into nonlinear regimes. This calls for the analysis to use von Karman large deflection strain-displacement relationships. A finite element model that combines the von Karman strains with the first-order shear deformation plate theory is developed. The development of the analytical model can accommodate an anisotropic composite laminate built up of uniformly thick layers of orthotropic, linearly elastic laminae. The global system of finite element equations is then reduced to a modal system of equations. Numerical simulation using a single-step algorithm in the time-domain is then carried out to solve for the modal coordinates. Nonlinear algebraic equations within each time-step are solved by the Newton-Raphson method. The random gaussian filtered white noise load is generated using Monte Carlo simulation. The acoustic pressure distribution over the plate is capable of accounting for a grazing incidence wavefront. Numerical results are presented to study a variety of cases.

[1] Graduate Research Assistant.

[2] Professor, Department of Aerospace Engineering, Old Dominion University, Norfolk, Virginia 23529–0247.

FOREWORD

The research results contained in this final technical report were performed under a NASA Langley Research Center Grant NAG-1–1358 entitled "Nonlinear Analyses of Composite Aerospace Structures in Sonic Fatigue". The report is based essentially on a Ph.D. dissertation prepared by Ms. Jayashree Moorthy under the guidance of Dr. Chuh Mei. The study was conducted at the Structural Acoustics Branch. The work was monitored under the supervision of Mr. Travis L. Turner, Structural Acoustics Branch, FMAD, NASA Langley Research Center.

The authors wish to acknowledge Dr. Steve Rizzi and Dr. Glenn Lasseigne for their resourceful and enlightening discussions. A very special thank to Jay Robinson, for the innumerable discussions and consultations during the research. The authors are grateful to him for the introduction to the use of PATRAN and the use of some of the statistical routines adapted in this work. The authors are also indebted to Dr. C.K. Chiang and Travis Turner who helped in so many ways.

TABLE OF CONTENTS

LIST OF TABLES

LIST OF FIGURES

NOMENCLATURE

a	x-direction plate dimension
a_j	nodal degree of freedom vector
b	y-direction plate dimension
c	speed of sound in air
c_{pr}	modal damping matrix
d_n	redefined unknown 'corrector' in modal displacement, $q_{n+1}(t)$
f	frequency in hertz (hz)
f_c	upper cut-off frequency of load spectrum
f_l	lower cut-off frequency of filter
f_u	Nyquist frequency
g_k	global time-lag array
h	plate thickness
k	kurtosis
k_{pr}	modal linear stiffness matrix
$k1_{prs}$	modal nonlinear quadratic stiffness tensor
$k2_{prst}$	modal nonlinear cubic stiffness tensor
m_{pr}	modal mass matrix
nf	number of filters used

$\mathbf{p}(t)$	pressure time-history
$\bar{p}_n(t)$	approximate random pressure at time, t_n
$p_p(t)$	modal random load vector
p_{av}^2	magnitude of pressure spectral density
p_{ref}	reference pressure level
p_{rms}	root mean square pressure
$q(t)$	modal displacement coordinate
$\dot{q}(t)$	modal velocity variable
$\ddot{q}(t)$	modal acceleration variable
$\tilde{\mathbf{q}}_\mathbf{n}$	known 'predictor' vector of variables q, $\dot{q}$, $\ddot{q}$, at time, t_n
s	skewness
t	time variable
t_1	initial time for integration
t_2	final time for integration
Δt	time-step size or sampling interval
u	mid-plane x-direction displacement
v	mid-plane y-direction displacement
w	mid-plane z-direction displacement
w_o	initial z-direction imperfection in flatness
x, y, z	laminate coordinate system
A_{ij}	laminate extensional stiffness matrix
A_{mn}	laminate shear stiffness matrix
$A0_i$, A_{ij}, $A1_{ijk}$, $A2_{ijkl}$	constant coefficients of d_j in nonlinear algebraic equation
B_{ij}	laminate bending-extension coupling stiffness matrix
B_{mj}^w	element shear strain matrix from deflection, $w(x,y)$

B^{ψ}_{ml}	element shear strain matrix from rotations, ψ_x & ψ_y
$[C]$	Lamina stiffness matrix in constitutive relations
C_{ij}	global system damping matrix
C_{il}	element strain matrix from membrane displacements and rotations
C^{o}_{il}	element strain matrix from initial imperfection, $w_o(x,y)$
C^{w}_{ijk}	nonlinear element strain tensor from deflection, $w(x,y)$
D	dissipative energy due to structural damping
D_{ij}	laminate bending stiffness matrix
E_1	Young's modulus in 1-direction of laminae
E_2	Young's modulus in 2-direction of laminae
F_i	global load vector for unit pressure
G_{12}, G_{13}, G_{23}	shear moduli of laminae
$H(f)$	frequency response function of filter
I_1, I_2, I_3	mass inertia terms in kinetic energy expression
$\mathcal{K}$	shear correction factor
K_{ij}	global system linear stiffness matrix
K^{T}_{ir}	tangent stiffness matrix in Newton-Raphson scheme
$K1_{ijk}$	global system nonlinear quadratic stiffness tensor
$K2_{ijkl}$	global system nonlinear cubic stiffness tensor
L	number of layers in laminate
M_i	moment resultants for laminate
M_{ij}	global system mass matrix
N	number of time-steps used in integration
N_{bc}	no. of global degrees of freedom suppressed as

	kinematic boundary conditions
N_{cr}	critical biaxial compressive buckling load
N_{df}	total global degrees of freedom of system
N_i	force resultants for laminate
N_j	Lagrangian interpolation functions
$P_i(t)$	global random load vector
Q_{ij}	reduced stiffness matrix for each lamina
$\bar{Q}_{ij}$	transformed reduced stiffness matrix for each lamina
Q_m	shear force resultants for laminate
R	number of modal coordinates used
$[R]$	Reuter matrix to transform tensor strain to engineering strain
T	kinetic energy of plate
T_o, T_1	constant and linear coefficients in temperature polynomial in z
$[T]$	laminate coordinate transformation matrix
$\Delta T(x, y, z)$	temperature distribution over plate
$\Delta T_{cr1,cr2,cr3}$	buckling temperatures for first three modes
U	strain energy of plate
U	displacement in x-direction
V	potential due to external work done
V	displacement in y-direction
W	displacement in z-direction
$W(t)$	weighting function in numerical integration
$\mathbf{X_n}$	filtered normally distributed process
$\mathbf{Y_k}$	broadband normally distributed process

Greek Symbols

α_1, α_2	thermal expansion coefficients for lamina material
α_n	unknown 'corrector' term in modal coordinate expressions
$\{\alpha_x \quad \alpha_y \quad \alpha_{xy}\}$	transformed thermal expansion coefficient vector
β	angle of incidence of pressure plane-wave
γ	total shear strain
γ^w	shear strain component from deflection
γ^ψ	shear strain component from rotations
δ	variational
ϵ_i	total strain vector
ε	Lagrangian strain tensor
ζ	damping coefficient
θ	free parameters in numerical integration
κ	curvature strain components vector
λ	eigenvalue
μ	mean value of a random variable
ν	Poisson's ratios
ξ, η	natural coordinates in isoparametric integration
ρ	density of lamina material
σ	standard deviation of a random variable
$\{\sigma_1 \quad \sigma_2 \quad \sigma_6\}$	stress vector for each lamina coordinates
$\{\sigma_x \quad \sigma_y \quad \sigma_{xy}\}$	stress vector in laminate coordinates
τ	time variable within each time-step
ϕ_r	mode-shape at r^{th} natural frequency
ψ_x	rotation about y-axis
ψ_y	rotation about x-axis
ω	natural frequency in radians per second

$[\Phi]$	modal transformation matrix
Ψ^p	nonlinear algebraic equation at p^{th} iteration

Superscripts

e	element level quantities
m	membrane quantities
o	initial imperfection
s	initial stress
u, v, w	corresponding to displacements u, v and w
ΔT	thermal load quantities
ψ, ψ_x, psi_y	curvature quantities

Only key superscripts have been listed.

Subscripts

Almost all lower-case alphabets have been used to denote indices of vectors, matrices and tensors. These and other subscripts not defined here are to be understood according to most recent definitions in text.

Chapter 1

INTRODUCTION

Acoustic fatigue and reliability have been serious considerations in the design of aircraft structural components for many years now. Reports of aircraft skin damage near jet engine exhausts, prompted the industry to go into an intensive study of this problem. Experimental activities were carried out on scaled models as well as on prototype assemblies. Analytical studies were performed using simple plate models under random pressure fluctuations. Given the limitations of computational abilities, these were simplistic linear models of panel response. The predictions of panel behavior from these models quite often overestimated response levels. The results from analytical work showed very poor agreement with test data. The design processes were, therefore, based on empirical relations derived using results from tests to modify the simple analytical models. These design guidelines, together with improved jet engine configurations, seemed to have alleviated the need for further analytical development for some time.

As modern day aircraft pushed their performance envelope further, the operating environment made greater demands on their structures. Apart from large pressure fluctuations in their vicinity, aerodynamic heating of exterior skin panels implied a high temperature environment. Failure and reliability had to be understood under combined high thermal and acoustic loading conditions. Moreover, the advent of advanced composite laminated structures brought on a new crop of

design problems. Their ability to sustain large displacements without yielding, moved panel response and behavior into the nonlinear regime.

All these changes reinvigorated and stepped up new research in the area of sonic fatigue. Although, this time around, there was a growing need to develop reasonably accurate analytical models. With the use of composites, it is impractical as well as inefficient to experimentally evaluate every conceivable design configuration. Analytical models, as close to being realistic as possible, could be used to numerically experiment with a multitude of configurations and predict a potentially good design. Towards this goal, a great deal of recent research has tried to refine models used for prediction of structural response of panels under random acoustic loading. There are fewer instances of work involving both acoustic and thermal loading. The explosive growth in the computational power of present day computers along with indepth knowledge in the application of finite element techniques in structural mechanics has greatly facilitated this development.

1.1 Literature Review

A discussion of the literature on acoustic fatigue must be preceded by a review of the research into causes and types of loading. One of the earliest works done in this area is a thoeretical study by Lighthill [1], establishing the relationship between jet exhaust velocities and intensity of sound radiation. Later on, Lansing et al. [2] studied the influence of impinging jet plumes on structures in increasing the pressure loads. Another related case occurs when ground reflections of pressure waves affect the pressure distribution near a structure. This has been studied by Scholton [3]. The second factor giving rise to pressure fluctuations is the presence of turbulent boundary layers. The earliest work giving pressure measurements in subsonic flow was by Bull [4]. The nature of the pressure spectrum in such a case was given by Coe and Chyu [5]. In the same study, the two authors also demonstrated

the interaction between boundary layers and high velocity jet exhaust. Pressure fluctuations are created due to instabilities such as cavities and shock waves, that arise from such mixing. These studies primarily established the sources of acoustic excitation in aircraft. Further research has grown into a whole new discipline in this area (computational aeroacoustics) and will not be dealt with here.

1.1.1 Experimental Work

Investigations into the response of simple structures to loading as discussed above, started predominantly as experimental work [6-9]. These, along with many more tests were compiled into 'nomographs' and design guides [10-12]. Test results on honeycomb sandwich panels using fiber reinforced and titanium bonded plates were produced by Holehouse [13], and Jacobson and van der Hyde [14]. Composite panels were tested by Wolfe and Jacobson [15], and White [16]. Test data were compared with linear predictions in [15], and by White and Mousley [17]. Further experimental work [18-20,22], when compared with theoretical results, served to demonstrate the shortcomings of linear theories in accurate predictions. This initiated the necessity to account for nonlinearities in modelling response behaviors, especially for composite structures. Later work [23-29] studied the large deformation aspects more thoroughly. A comprehensive review of existing test data to show the presence of large deformation was given by Mei [29]. Of these, Bennouna and White [25] compared nonlinear analytical and experimental results for beams. The paper by van der Hyde and Kolb [23] contains test data for a stiffened panel. Mei and Wentz [24] compared results from the equivalent linearization method with tests on rectangular panels. White and Teh [27] also studied the nonlinear behavior of a panel under in-plane compressive loads (less than buckling) and acoustic excitation using test results and Rayleigh-Ritz solutions. Robinson et al. [28] also tried to match simulation strain spectra with test results for flat and stiffened carbon panels under

high intensity acoustic loading. This study observed an 'overprediction in the effect of nonlinearity' in the nonlinear simulation model. The boundary conditions used allowed for elastic supports. The pressure time-history used was obtained directly from the test readings.

1.1.2 Analytical Work

Linear Response:

The earliest theoretical papers, apart from those with experimental work mentioned above, were all based on linear theories [30-39]. A normal-mode method to determine multi-mode response under a space and time correlated pressure distribution was given by Powell [31]. This was simplified by Clarkson [34]. The studies by Samuels and Eringen [32], Bogdanoff and Goldberg [36], Crandall and Yildiz [37] and Mercer [38] all dealt with beam structures. The first paper amongst these [32], used a generalized Fourier series in combination with a Timoshenko beam model. The latter two [36,37] showed that infinite values for mean-square responses under infinite mean-squared input existed only for particular models of excitation. Miles [30], Eringen [33] and Elishakoff [39] presented results for plates. The Galerkin approach was used by Elishakoff [39].

Nonlinear Response:

Among the various methods available for solving nonlinear random vibration problems, the approach based on the Fokker-Planck-Kolmogorov (FPK) equation was an early entrant. The mathematical background for the application of the FPK equation has been given by Caughey [40]. This method generates a governing differential equation for the probability density function of a Markov process. The solution to the FPK equation as applied to the Duffing oscillator has been studied by Crandall [41], Caughey [42] and Lyon [43,44], among others. Caughey and Ma [45] have given exact solutions to a few nonlinear single-degree-of-freedom systems.

In the case of continuous nonlinear systems, approximate solutions have been obtained [46-50]. Nash [46] has compared approximate solutions, using four different methods, to a single-degree-of-freedom reduction of the large amplitude vibration of plates and shells. He has numerically integrated the reduced equation; represented the equation of motion as well as the compatibility equation by a finite-difference model and subsequently integrated them; used the FPK exact solution; and finally, also used the equivalent linearization approximation. Ahmadi et al. [47] compare the FPK approach and the equivalent linearization technique against a perturbation method for the nonlinear response of plates under random loads.

The perturbation technique was extended to stochastic vibration problems by Crandall [51]. In addition, multi-degree-of-freedom systems [52,53] and continuous systems [46,47,54] have been studied using this method. Another technique for solution is the stochastic averaging method, used when there is narrow-band excitation of a lightly-damped system [55-58]. A normal-mode approach directly applied to stresses has been used by Maymon [59] .

The one technique that proved to be very effective and convenient in applications for nonlinear structural systems is the equivalent linearization technique [60-91]. The pioneers in adapting this method to stochastic systems are Booton [60] and Caughey [61]. It was then refined and made less cumbersome, for gaussian processes in particular [62,63]. Initial application of the equivalent linearization method was for single-degree-of-freedom systems [64, 65]; the Duffing oscillator under broad-band loading [66,67]; and under narrow-band loading [68]. A comparison with perturbation solutions for systems with small linearities was given by Crandall [64]. Closed form solutions were obtained by Lyon [66], and Iwan and Yang [67]. A significant advantage of this method is its easy extension to multi-degree-of-freedom systems [69-73]. Spanos [73] and Roberts [74] showed good agreement with results from direct simulation solutions.

The equivalent linearization technique has been used to study the nonlinear random response of beams [75-79] and isotropic plates [46,47,80-84]. These include single-mode as well as multiple-mode solutions. Langley [76] presents a formulation that directly solves for the response transfer function by using a Cholesky factorization of the equivalent linear equation. Miles [84] modifies the equivalent linearization procedure such that the response need no longer be assumed gaussian. He compares single-mode results of the fatigue-life for a plate with those obtained from numerical simulation and from the probabilistic estimate for damage rate. The analytical solutions for the response of composite laminated plates under acoustic loading have primarily been presented by Mei and his associates [85-91]. All these papers give single-mode solutions. The paper by Mei and Wentz [87] studies anti-symmetric angle-ply laminates and the rest pertain to symmetric laminates. Of these, Ref.[88] deals with nonlinear damping, Ref.[89] studies the effect of transverse shear, Ref.[90] uses elastically restrained edges, and Ref.[91] uses mixed boundary conditions.

Some excellent review papers bring up to date the developments in random vibrations until the mid-eighties [92-95].

Finite Element Methods:

Probably the earliest effort to model a random vibration problem using finite elements was by Jacobs and Lagerquist [96]. This was followed by a few more which were still restricted to linear theory [97-100]. Olson [98] modelled the excitation cross spectral density over each element with a polynomial function and then proceeded with the spatial integration. Dey [99] presents solutions using a matrix inversion method and the normal mode method. The global matrices are formed using the finite element package ASKA, and subsequently used as inputs in the formulation that follows. Apart from these, initial applications of finite elements relied on large programs like NASTRAN [18,22,35]. The first instance of a finite element model applied to a nonlinear random response problem seems to be in the

paper by Hwang and Pi [101]. A conforming triangular element has been used to develop all the global matrices for a plate system. The inplane displacement equations are eliminated by static condensation and the equivalent linearization technique is then applied. This was followed by work on isotropic beams and plates by Mei and his associates [102-105]. All these studies were based on the equivalent linearization method. Random response of beams was studied by Mei and Chiang [102] and Chiang and Mei [103]. This was followed up by a study of thermally buckled beams by Locke and Mei [104]. The coupled thermo-acoustic problem was treated in two steps. Thermal buckling analysis solutions were used for the random vibration analysis as initial deflections. The study on beams was then extended to plates by Locke [105]. The formulations were similar in the two cases. A uniform white noise gaussian pressure distribution of increasing decibel levels was used. A 24-degree-of-freedom rectangular plate element was utilized. Solutions were compared to their earlier classical single-mode solutions. A convergence study on the number of modes active in the solution used up to four symmetric modes. The formulation used a static reduction or static condensation concept to eliminate inplane equations. The mode-shapes for the thermally buckled plate were used to carry out a modal reduction of the system equations.

The next level of advancement was the inclusion of composite laminated plates in random vibration analysis [106-108]. Robinson [106] studied the nonlinear random vibration of a particular laminated plate using a time-domain approach. A symmetric quarter-plate model of 48-degree-of-freedom rectangular elements was subjected to a spatially uniform high-decibel pressure distribution. The nonlinear equations were carried through every time-step and a Newton-Raphson iteration scheme was adopted to obtain converging solutions within each time-step. This simulation, of the nonlinear system of equations, has been implemented using a

modified single-step integration algorithm. Chen [107,108] also worked on composite plates using the equivalent linearization technique. His formulation includes consideration of nonwhite gaussian processes and processes with non-zero means. He has also presented results for different types of loading assumptions, including spatially random gaussian processes. A normal-modes reduction combined with an equivalent linearization approach has been verified against solutions from Monte-Carlo simulations.

Numerical Simulations:

Simulation techniques seemed to have been used popularly as a tool to verify analytical results obtained from other methods [46,73,74,84,107,109]. The first attempt at formulating a Monte-Carlo technique for a geometrically nonlinear system was likely by Dowell [110]. Most efforts at applying the Monte-Carlo simulation technique for a random vibration problem concentrate on developing suitable methods of load generation. Some of the research in load modelling was not in combination with numerical simulation, although they did lay the groundwork for further study [33,111,112]. The paper by Dyer [111] models a correlated pressure field which is convecting and at the same time decaying over a plate. As the scale of correlation distances grows much smaller than the plate dimensions, the pressure field reduces to a purely uncorrelated random 'raindrop' process as mentioned by Eringen [33]. The last of these papers [112] offers another model for the pressure load by treating it as a correlated stream of impulses arriving randomly.

A digitally generated gaussian random load is used by Belz [113] to study the nonlinear vibration of a beam. The power-residue method has been used to generate a sequence of 'pseudo-random' numbers. These are then transformed to a set of gaussian numbers, which in turn are scaled suitably to give the random load vector. A finite-difference form of the equation of motion is solved assuming that the load is a concentrated point load. Robinson [106] uses a similar method for load generation

and goes on to use the single-step algorithm developed by Zienkiewicz et al. [114] to solve a system of finite element equations. Other than these works, a major contribution to the field of Monte-Carlo simulation has come from Shinozuka, Vaicaitis, et al. The simulation of a multivariate, multidimensional random process using a combination of cosine functions with random phase was developed by Shinozuka [115-118]. Each of the functions has a weighting amplitude and the random phase angles are distributed uniformly between 0 and 2π. This series of cosine functions is summed at constant frequency and wave-number intervals. The weighting amplitude is determined from the cross-spectral density prescribed. The simulation process can be applied to non-homogeneous processes, too, the 'non-homogeneity' being defined by a constant spectral-density that may be made 'transient' by a deterministic function of time and space. Another method based on the generation of discrete frequency functions corresponding to the desired random process was given by Wittig and Sinha [119]. A quick FFT of this generated series then results in the actual random process. Sengupta [120] formulated a procedure to derive the spectrum of a decaying, non-homogeneous field. This modelling is particularly directed at propeller-driven aircraft excitation, where the excitation signal has dominant harmonic components at the blade-passage frequency.

Solutions based on the Shinozuka approach for various types of panels were given by Vaicaitis and others [121-126]. The formulation for the plate governing equations is based on an analytical Galerkin method. A fifth-order Runge-Kutta integration scheme is then utilized. Results generated cover a broad range of statistical characteristics including variances, probability densities, peak probability densities, crossing-rates, damage estimates, etc. The papers include response data for stiffened panels and composite panels. A variety of loading possibilities due to turbulent boundary layers, exhaust noise, unsteady aerodynamic pressure, cavity

pressure, shock wave impingement, parametric excitations as well as aerodynamic heating have been considered.

1.1.3 Thermal Effects

High performance military aircraft of today and the future high speed civil transport planes can have high acoustic and thermal loads occurring simultaneously for significant durations. The effects of high temperature loading on random response, therefore, have become a very relevant concern in aircraft structural design. Thermal loading conditions in combination with acoustic loading have been experimentally studied before [20,109,127-130]. Random vibration experiments were conducted on initially buckled beams by Seide and Adami [109]. An attempt was made at predicting the onset of the 'snap-through' phenomenon. The earlier activities [127-130] showed a decrease in the life of all types of panels (isotropic, stiffened, composite), at a particular stress level, with increasing temperature. All these tests reaffirmed the existence of the 'snap-through' phenomenon near critical buckling loads and the necessity to develop better analytical models.

More recently, Ng along with his partners [26,131,132] studied plates under thermal [131,132] as well as static in-plane [26] loading. The tests in Ref.[131] seem to indicate that severe snap-through and chaotic motion occur more with rigidly clamped edge conditions. A little leeway in in-plane motion, as is usually the case in everyday structural assemblies, may alleviate such extreme stress cycles. Ng and White [26] used the Rayleigh-Ritz method to study a composite plate under inplane compressive loads in the buckling/postbuckling range. Comparisons were made against test data. Thermal effects on random response were also studied by Lee [83]. Apart from temperature variation over an isotropic plate surface, he also considers thermal gradients across thickness, or, thermal moments. The analysis is a single-mode representation of the equations of motion, solved using the equivalent

linearization technique. He notes that the influence of temperature variation on the rms displacement and stress values steadily drops off as the intensity of acoustic loading increases. In addition, he concludes that although thermal moments make little difference in the displacement solutions, normal stresses depend on the temperature gradient. This becomes significant when considering fatigue life aspects for a structure.

A good overview of research discussed in the above sections is available in a report by Clarkson [133] and a recent paper by Vaicaitis [134].

1.2 Outline of Present Study

A Monte Carlo simulation of a laminated plate under simultaneous acoustic and thermal loading is the main focus of this study. As mentioned before, the combination of temperature loads and high-intensity acoustic pressure fluctuations is a very legitimate concern in the development of the high speed transport aircraft. Existing literature on this problem still leaves room for good numerical models for prediction of structural response under such conditions. Of the very few published works that relate to the combined problem, only one [83] considers thermal gradients, using an analytical single-mode plate model. None of them utilize the advantages of a finite element model. The flexibility in modelling an arbitrarily laminated plate under complicated boundary conditions is exclusively a feature of finite element methods. As has been demonstrated in earlier research, neither test setups nor real life assemblies show purely simply-supported or purely clamped boundary conditions. A certain amount of in-plane motion is allowed. This can be attempted in a straight forward manner using finite elements.

The plate theory to be used accounts for transverse shear rotations and strains. This helps application of the formulation irrespective of plate thickness. Furthermore, accuracy is improved when bending-extension coupling exists, particularly

when the laminate has only a few layers. In addition, higher frequencies are predicted more accurately as plate flexibility is assumed to be greater in a transverse shear model.

The use of a numerical simulation technique provides a more detailed picture of the results than, say, the equivalent linearization technique. A variety of statistical information including higher-order moments, probability densities, peak probability densities, etc. can be extracted from response time-histories. Moreover, the spectral densities obtained, more accurately show the widening of peaks expected in nonlinear responses. With the computational speed and size of today's computers, an attempt to generate a broad database of results considering various parameters relevant to random vibration is a viable project.

Nevertheless, a modal reduction of the large system of displacement equations is carried out. This has the advantage of representing the desired plate system with a fewer number of time-dependent equations. A multiple mode analysis for a nonlinear system will show the interaction between modes, which is not available otherwise. For instance, the relative drop in the rms modal displacement value of the first mode in a multi-mode solution, as compared to a single-mode solution, as occurs in some cases, can only be observed by multiple mode approximations. A further advantage of using a simulation technique is the flexibility available in load modelling. A spatially correlated pressure distribution, in the case of a travelling-wave acoustic field that is not normally incident, is generated and its effects on the response studied.

As stated above, the temperature distribution is assumed to be more general, including gradients across the thickness. The surface distribution is restricted to being symmetric, in keeping with data from test setups. The formulation also accommodates initial imperfections in the plate as well as initial stresses. The

numerical integration scheme used in this study follows the method implemented by Robinson [106].

An outline of the material in the following pages is now presented. Chapter 2 develops the finite element formulation of the governing equations and then transforms them to a modal system of equations, ready for integration in time. In Chapter 3, the single-step algorithm in combination with the Newton-Raphson iteration scheme is developed. The details of generating a gaussian random pressure time-history, correlated in one spatial dimension, are explained in Chapter 4. The methods used to generate the response statistics and spectrum are briefly explained. Other considerations that come up during implementation of the finite element program are also discussed here. These include the determination of mode-shapes for systems where in-plane degrees-of-freedom may or may not be coupled with bending degrees-of-freedom. Finally, Chapter 5 presents various numerical examples and offers inferences. Concluding remarks are presented in Chapter 6.

Chapter 2

FINITE ELEMENT FORMULATION

Governing differential equations modelling the nonlinear behavior of a plate under random dynamic and thermal loads are derived in this chapter. The equations of motion are formulated based on the first-order shear deformation plate theory.

2.1 Assumptions

The following are the assumptions and restrictions that go into defining the problem.

- von Karman large deflections
- small strains and rotations
- rotatory inertia included
- orthotropic, linear elastic lamina of uniform thickness
- plane stress
- proportional damping

The application of the first-order theory, including shear deformation, implies that inplane displacements are linear functions of the transverse coordinate, z. Also, straight lines normal to the mid-plane before deformation remain straight *but not normal* after deformation. Further, transverse normals are inextensible, i.e., transverse normal strain is zero. As part of the plane stress assumption, transverse normal stress is treated negligible compared to the inplane and the transverse shear

stresses. As a consequence of the inplane displacements being linear in z, transverse shear strains, and therefore stresses, turn out to be constant through the thickness of the plate (hence not satisfying the free surface zero stress boundary conditions). To partially rectify this discrepancy, a *shear correction factor* is used.

2.2 Strain-Displacement Relationships

The displacement field over any element of a shear deformable plate is represented by

$$\begin{aligned} \mathrm{U}(x,y,z,t) &= u(x,y,t) + z\psi_x(x,y,t) \\ \mathrm{V}(x,y,z,t) &= v(x,y,t) + z\psi_y(x,y,t) \\ \mathrm{W}(x,y,z,t) &= w(x,y,t) + w_o(x,y), \end{aligned} \tag{2.2.1}$$

where u,v,w are the plate mid-plane displacements along x,y,z respectively and ψ_x, ψ_y are the rotations about y and x axes respectively. $w_o(x,y)$ is the initial imperfection or the deviation from flatness of the plate. It must be noted here that $w_o(x,y)$ has no restrictions to being smaller than w.

The above five degrees of freedom, u, v, w, ψ_x, ψ_y, are expressed in terms of element shape functions, N_j (see Appendix A), i.e.,

$$\begin{aligned} u(x,y,t) &= N_j a_j^u(t) \\ v(x,y,t) &= N_j a_j^v(t) \\ w(x,y,t) &= N_j a_j^w(t) \\ \psi_x(x,y,t) &= N_j a_j^{\psi_x}(t) \\ \psi_y(x,y,t) &= N_j a_j^{\psi_y}(t), \end{aligned} \tag{2.2.2}$$

where $a_j^u, a_j^v, a_j^w, a_j^{\psi_x}, a_j^{\psi_y}$ are the values of the displacements u, v, w, ψ_x, ψ_y at the j^{th} node of the element (see Fig.1).

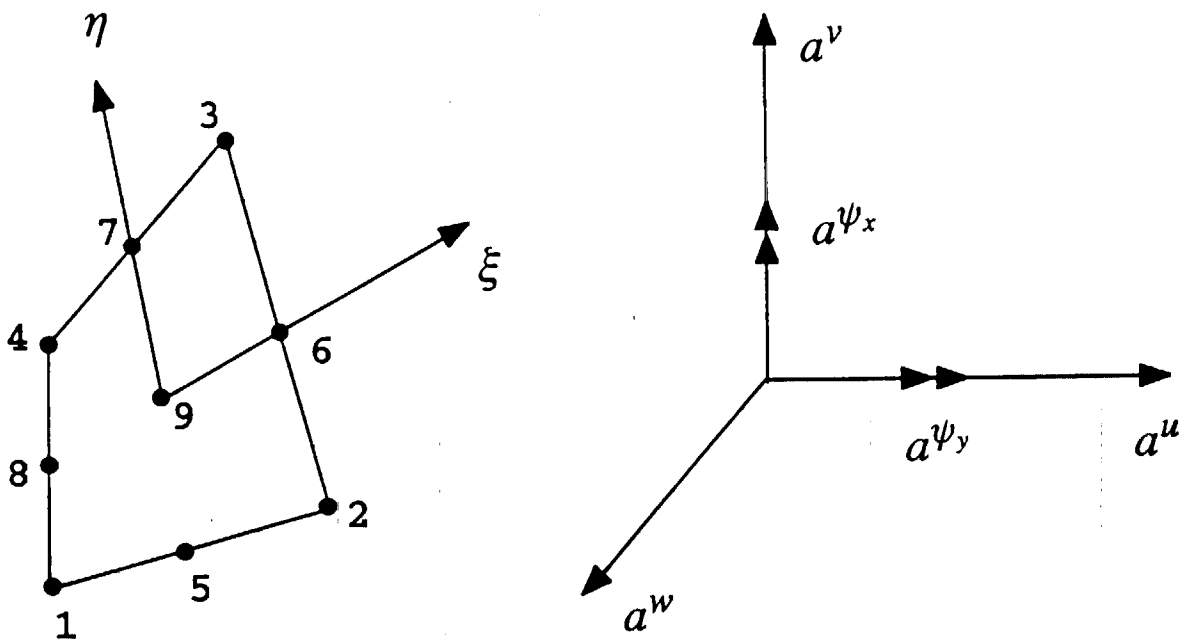

Fig.1 Lagrangian Quadratic 9-node Element

The shape functions, N_j, are chosen to be Lagrangian quadratic interpolation polynomials [135]. The same shape functions are used for all the five degrees of freedom, since isoparametric integration is to be used over each element.

In general the strain-displacement relationships are written as,

$$\varepsilon_{ij} = \frac{1}{2}(u_{i,j} + u_{j,i} + u_{k,i}\,u_{k,j}), \qquad i;j;k = 1,2,3 \tag{2.2.3}$$

where a 'comma' followed by a subscript denotes differentiation with respect to that coordinate. The notation ε_{ij} represents the Lagrangian nonlinear strain tensor.

Using deflections in the von Karman sense, it is assumed that components of strains due to inplane displacements are much smaller than those corresponding to transverse deflection, $w(x,y,t)$. Thus, the expressions for strains reduce to,

$$\begin{aligned}
\varepsilon_1 &= \varepsilon_{11} = U_{,x} + \frac{1}{2}(W_{,x})^2 \\
\varepsilon_2 &= \varepsilon_{22} = V_{,y} + \frac{1}{2}(W_{,y})^2 \\
\varepsilon_4 &= 2\varepsilon_{23} = V_{,z} + W_{,y} \\
\varepsilon_5 &= 2\varepsilon_{31} = W_{,x} + U_{,z} \\
\varepsilon_6 &= 2\varepsilon_{12} = U_{,y} + V_{,x} + W_{,x}\,W_{,y}
\end{aligned} \tag{2.2.4}$$

Strains with contracted notation subscripts have been simultaneously defined to facilitate further derivation which uses index notation extensively. Substituting for U, V, W from Eq.(2.2.1) and writing the shear strain terms separately, we have,

$$\begin{Bmatrix} \varepsilon_1 \\ \varepsilon_2 \\ \varepsilon_6 \end{Bmatrix} = \begin{Bmatrix} u_{,x} \\ v_{,y} \\ u_{,y} + v_{,x} \end{Bmatrix} + z \begin{Bmatrix} \psi_{x,x} \\ \psi_{y,y} \\ \psi_{x,y} + \psi_{y,x} \end{Bmatrix} + \frac{1}{2} \begin{Bmatrix} {w_{,x}}^2 \\ {w_{,y}}^2 \\ 2\,w_{,x}\,w_{,y} \end{Bmatrix}$$

$$+ \begin{Bmatrix} w_{,x}\,w_{o,x} \\ w_{,y}\,w_{o,y} \\ w_{,x}\,w_{o,y} + w_{o,x}w_{,y} \end{Bmatrix}$$

and

$$\begin{Bmatrix} \varepsilon_5 \\ \varepsilon_4 \end{Bmatrix} = \begin{Bmatrix} \psi_x \\ \psi_y \end{Bmatrix} + \begin{Bmatrix} w_{,x} \\ w_{,y} \end{Bmatrix} \tag{2.2.5}$$

Or, in other words,

$$\epsilon_i = \epsilon_i^m + z\kappa_i + \epsilon_i^w + \epsilon_i^o, \qquad i = 1,2,6$$

and

$$\gamma_m = \gamma_m^\psi + \gamma_m^w, \qquad m = 5,4 \tag{2.2.6}$$

where ϵ^w is the geometrically nonlinear strain term and the rest are all linear functions of displacements. Note that in writing strain components from $(w + w_o)$ there is no contribution from derivatives of w_o alone since the plate was strain-free with initial imperfection, w_o. Next, the displacement functions above are represented in terms of their shape functions. As mentioned earlier, all matrices and tensors (rank greater than 2) are described using index subscripts henceforth. Using Eqs.(2.2.2) and Eqs.(2.2.5) and Eq.(2.2.6), we get,

$$\epsilon_i^m = \begin{bmatrix} N_{j,x} & 0 \\ 0 & N_{j,y} \\ N_{j,y} & N_{j,x} \end{bmatrix} \begin{Bmatrix} a_j^u \\ a_j^v \end{Bmatrix} \qquad j = 1,\ldots,npe$$

$$= C_{il}\, a_l^m, \qquad l = 1,\ldots,2j \tag{2.2.7}$$

Similarly,

$$\kappa_i = \begin{bmatrix} N_{j,x} & 0 \\ 0 & N_{j,y} \\ N_{j,y} & N_{j,x} \end{bmatrix} \begin{Bmatrix} a_j^{\psi_x} \\ a_j^{\psi_y} \end{Bmatrix}$$

$$= C_{il}\, a_l^\psi \tag{2.2.8}$$

where *npe* denotes the number of nodes per element which is the maximum value j can attain. Since the shape functions N_j are common for all degrees of freedom, the matrix C_{il} is the same for ϵ_i^m and κ_i.

In like fashion we can write

$$\epsilon_i^o = \begin{bmatrix} N_{j,x}\, w_{o,x} \\ N_{j,y}\, w_{o,y} \\ N_{j,y}\, w_{o,x} + N_{j,x}\, w_{o,y} \end{bmatrix} \{a_j^w\}$$

$$= C_{ij}^o\, a_j^w, \tag{2.2.9}$$

$$\epsilon_i^w = \frac{1}{2} \begin{Bmatrix} N_{j,x} N_{k,x} \\ N_{j,y} N_{k,y} \\ 2\, N_{j,x} N_{k,y} \end{Bmatrix} \{a_j^w\} \{a_k^w\}$$

$$= C_{ijk}^w\, a_j^w a_k^w, \qquad j;k = 1,\ldots,npe \tag{2.2.10}$$

$$\gamma_m^\psi = \begin{bmatrix} N_j & 0 \\ 0 & N_j \end{bmatrix} \begin{Bmatrix} a_j^{\psi_x} \\ a_j^{\psi_y} \end{Bmatrix}$$

$$= B_{ml}^\psi\, a_l^\psi, \qquad m = 5,4 \tag{2.2.11}$$

and

$$\gamma_m^w = \begin{bmatrix} N_{j,x} \\ N_{j,y} \end{bmatrix} \{a_j^w\}$$

$$= B_{mj}^w\, a_j^w \tag{2.2.12}$$

2.3 Stress Resultants

Constitutive relations first need to be developed for individual lamina under plane stress, as assumed. Additionally, the lamina stiffnesses are restricted to those for an orthotropic lamina.

2.3.1 Constitutive Relations

The thermoelastic stress-strain relationship for an orthotropic material is given by

$$\begin{Bmatrix} \sigma_1 \\ \sigma_2 \\ \sigma_3 \\ \sigma_4 \\ \sigma_5 \\ \sigma_6 \end{Bmatrix} = \begin{bmatrix} C_{11} & C_{12} & C_{13} & 0 & 0 & 0 \\ C_{12} & C_{22} & C_{23} & 0 & 0 & 0 \\ C_{13} & C_{23} & C_{33} & 0 & 0 & 0 \\ 0 & 0 & 0 & C_{44} & 0 & 0 \\ 0 & 0 & 0 & 0 & C_{55} & 0 \\ 0 & 0 & 0 & 0 & 0 & C_{66} \end{bmatrix} \begin{Bmatrix} \varepsilon_1 - \alpha_1 \Delta T \\ \varepsilon_2 - \alpha_2 \Delta T \\ \varepsilon_3 - \alpha_3 \Delta T \\ \varepsilon_4 \\ \varepsilon_5 \\ \varepsilon_6 \end{Bmatrix} \tag{2.3.1}$$

These are the lamina stresses given in terms of the strains and the independent material constants $[C]$ for any ply in its own principal material directions [136].

Using the above equation, the stress-strain relations for a lamina under plane stress, result in a *reduced stiffness matrix*, Q_{ij}. Rewriting the constitutive relation therefore, we obtain

$$\begin{Bmatrix} \sigma_1 \\ \sigma_2 \\ \sigma_6 \\ \sigma_4 \\ \sigma_5 \end{Bmatrix} = \begin{bmatrix} Q_{11} & Q_{12} & 0 & 0 & 0 \\ Q_{12} & Q_{22} & 0 & 0 & 0 \\ 0 & 0 & Q_{66} & 0 & 0 \\ 0 & 0 & 0 & Q_{44} & 0 \\ 0 & 0 & 0 & 0 & Q_{55} \end{bmatrix} \begin{Bmatrix} \varepsilon_1 - \alpha_1 \Delta T \\ \varepsilon_2 - \alpha_2 \Delta T \\ \varepsilon_6 \\ \varepsilon_4 \\ \varepsilon_5 \end{Bmatrix} \tag{2.3.2}$$

where in terms of the engineering constants,

$$\begin{aligned} Q_{11} &= \frac{E_1}{1 - \nu_{12}\nu_{21}} \\ Q_{12} &= \frac{\nu_{12} E_2}{1 - \nu_{12}\nu_{21}} = \frac{\nu_{21} E_1}{1 - \nu_{12}\nu_{21}} \\ Q_{22} &= \frac{E_2}{1 - \nu_{12}\nu_{21}} \end{aligned}$$

and $Q_{44} = G_{23}$, $Q_{55} = G_{31}$, $Q_{66} = G_{12}$, remain unchanged.

For a laminate of many plies, each having its material axes oriented differently with respect to the laminate axes, the constitutive relations must be transformed from the principal material directions, 1,2 and 6, to the global coordinates x, y, z of the laminate (Fig.2). Upon transformation, the *transformed reduced stiffnesses* for a given layer are

$$[\bar{Q}] = [T]^{-1} [Q] [T]^{-T}$$

where

$$[T]^{-T} = [R][T][R]^{-1}$$

with $[R]$ being the Reuter's matrix as defined by Jones [136]. Transforming the thermal strain tensor from the principal material directions to the laminate coordinates as follows

$$\epsilon_i^{\Delta T^k} = \left\{ \begin{array}{c} \alpha_x \Delta T \\ \alpha_y \Delta T \\ \alpha_{xy} \Delta T \end{array} \right\}^k = [T]^T \left\{ \begin{array}{c} \alpha_1 \Delta T \\ \alpha_2 \Delta T \\ 0 \end{array} \right\}$$

We are now ready to compute the stress resultants with

$$\left\{ \begin{array}{c} \sigma_x \\ \sigma_y \\ \sigma_{xy} \\ \sigma_{yz} \\ \sigma_{xz} \end{array} \right\}^k = \left[\begin{array}{ccccc} \bar{Q}_{11} & \bar{Q}_{12} & \bar{Q}_{16} & 0 & 0 \\ \bar{Q}_{12} & \bar{Q}_{22} & \bar{Q}_{26} & 0 & 0 \\ \bar{Q}_{16} & \bar{Q}_{26} & \bar{Q}_{66} & 0 & 0 \\ 0 & 0 & 0 & \bar{Q}_{44} & \bar{Q}_{45} \\ 0 & 0 & 0 & \bar{Q}_{45} & \bar{Q}_{55} \end{array} \right]^k \left\{ \begin{array}{c} \epsilon_x - \alpha_x^k \Delta T \\ \epsilon_y - \alpha_y^k \Delta T \\ \gamma_{xy} - \alpha_{xy}^k \Delta T \\ \gamma_{yz} \\ \gamma_{xz} \end{array} \right\} \tag{2.3.3}$$

for the k^{th} layer of the laminate. The expression for strain can be substituted from Eqs.(2.2.6) in Eq.(2.3.3) and the final form of the constitutive relations for the k^{th} layer is given by

$$\sigma_i^k = \bar{Q}_{ij}^k \left(\epsilon_j^m + z\kappa_j + \epsilon_j^w + \epsilon_j^o - \epsilon_i^{\Delta T^k} \right) + \sigma_i^s \tag{2.3.4}$$

$$\sigma_m^k = \bar{Q}_{mn}^k \left(\gamma_n^\psi + \gamma_n^w \right) \tag{2.3.5}$$

with i, j, m, n as defined in section 2.2. Implicit is the condition that the plate is strain-free under $w_o(x, y)$ and σ_i^s. The additional stress term σ_i^s relates to the specified initial stress distribution, as had been stated in the problem definition.

Henceforth all the stresses denoted with index subscripts are in laminate coordinates, x, y, z.

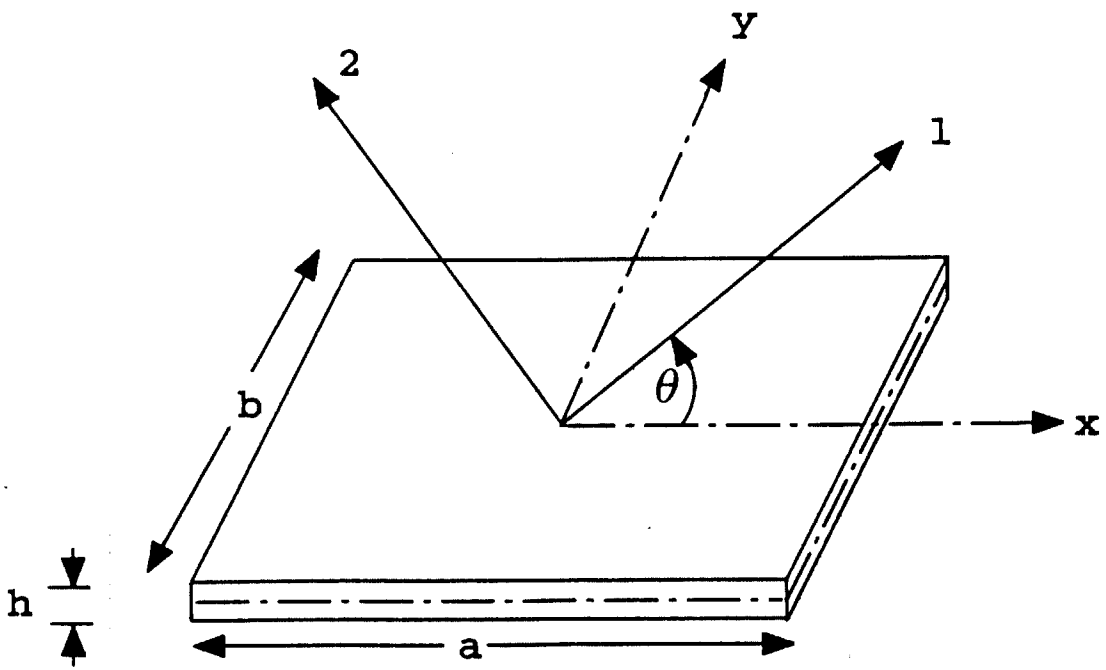

Fig.2 Rectangular Laminated Plate

2.3.2 Force and Moment Resultants

Having written down the expressions for stresses in any ply, the various resultant forces and moments that are to be used in formulating the governing equations of motion for the laminate are to be defined. These are in units of force or moment *per unit length*, as stresses are integrated over the thickness only. The resultant forces, N_i and Q_m, and the resultant moments, M_i are

$$N_i = \int_{-h/2}^{h/2} \sigma_i \, dz = \sum_{k=1}^{L} \int_{z_{k-1}}^{z_k} \sigma_i^k \, dz \qquad i = 1,2,6 \quad (2.3.6)$$

$$M_i = \int_{-h/2}^{h/2} \sigma_i \, z \, dz = \sum_{k=1}^{L} \int_{z_{k-1}}^{z_k} \sigma_i^k \, z \, dz \quad (2.3.7)$$

and

$$\begin{Bmatrix} Q_5 \\ Q_4 \end{Bmatrix} = \int_{-h/2}^{h/2} \mathcal{K}^2 \begin{Bmatrix} \sigma_5 \\ \sigma_4 \end{Bmatrix} dz = \sum_{k=1}^{L} \int_{z_{k-1}}^{z_k} \mathcal{K}^2 \begin{Bmatrix} \sigma_5 \\ \sigma_4 \end{Bmatrix}^k dz \quad (2.3.8)$$

where $1,2,6,5,4$ now correspond to x, y, xy, xz, yz directions respectively, and $\mathcal{K}^2$ is a constant shear correction factor. Integration over the thickness is carried out by summing up the integrations over L layers. The distance from the midplane of the plate to the bottom of the k^{th} layer is z_{k-1}, with $z_o = -h/2$.

Substituting for stresses from Eqs.(2.3.4-5) into Eqs.(2.3.6-8) above, the stress resultants in terms of *laminate stiffnesses* are as follows.

$$N_i = A_{ij} \left(\epsilon_j^m + \epsilon_j^w + \epsilon_j^o \right) + B_{ij}\kappa_j - N_i^{\Delta T} + N_i^s \quad (2.3.9)$$

$$M_i = B_{ij} \left(\epsilon_j^m + \epsilon_j^w + \epsilon_j^o \right) + D_{ij}\kappa_j - M_i^{\Delta T} + M_i^s \quad (2.3.10)$$

and the shear force resultants

$$Q_m = \mathcal{K}^2 A_{mn} \gamma_n, \qquad m;n = 5,4 \quad (2.3.11)$$

where

$$A_{ij} = \sum_{k=1}^{L} \int_{z_{k-1}}^{z_k} \bar{Q}_{ij}\, dz$$

$$= \sum_{k=1}^{L} \bar{Q}_{ij}^{k} \left(z_k - z_{k-1} \right) \qquad i;j = 1,2,6$$

are the laminate extensional stiffnesses,

$$B_{ij} = \sum_{k=1}^{L} \int_{z_{k-1}}^{z_k} \bar{Q}_{ij}\, z\, dz$$

$$= \sum_{k=1}^{L} \bar{Q}_{ij}^{k} \left(\frac{z_k^2 - z_{k-1}^2}{2} \right)$$

are the laminate bending-stretching coupling stiffnesses,

$$D_{ij} = \sum_{k=1}^{L} \int_{z_{k-1}}^{z_k} \bar{Q}_{ij}\, z^2\, dz$$

$$= \sum_{k=1}^{L} \bar{Q}_{ij}^{k} \left(\frac{z_k^3 - z_{k-1}^3}{3} \right)$$

are the laminate bending stiffnesses,

$$N_i^{\Delta T} = \sum_{k=1}^{L} \int_{z_{k-1}}^{z_k} \bar{Q}_{ij}\, \epsilon_j^{\Delta T}(z)\, dz$$

is the thermal force resultant, and

$$M_i^{\Delta T} = \sum_{k=1}^{L} \int_{z_{k-1}}^{z_k} \bar{Q}_{ij}\, z\, \epsilon_j^{\Delta T}(z)\, dz$$

is the thermal moment resultant. A_{mn}, the laminate shear stiffnesses, are defined identical to extensional stiffnesses, A_{ij}.

2.4 Hamilton's Principle

The governing equations for the problem are derived based on Hamilton's Variational Principle, modified by a weighting function, $W(t)$, to be used for numerical integration in the time-domain. This can be mathematically expressed as

$$\delta \int_{t_1}^{t_2} W(t) \left(T - U - V + D \right) dt = 0 \qquad (2.4.1)$$

where

T = Kinetic energy of plate

U = Strain energy of plate

V = Potential due to external loads on the plate

D = Dissipative energy of plate; and

t_1 and t_2 imply initial and final time of the time domain. Each of these expressions will be derived in the following sections. The dissipated energy is due to structural damping, which is assumed directly proportional to the inertia of the plate.

2.4.1 Kinetic Energy

The kinetic energy of the plate in terms of the three velocity components can be written as

$$T = \int_{\mathrm{V}} \frac{1}{2} \rho (\dot{U}^2 + \dot{V}^2 + \dot{W}^2) d\mathrm{V} \tag{2.4.2}$$

where ρ is the density of the plate and U, V and W are the displacements as defined in Eqs(2.2.1). A dot over the variables indicates differentiation with respect to time. On substituting from Eqs.(2.2.1) for the overall displacements and carrying out the variation operation, we obtain

$$\delta T = \int_{-h/2}^{h/2} \int_{\mathrm{A}} \rho \big[(\dot{u} + z\dot{\psi}_x)(\delta\dot{u} + z\delta\dot{\psi}_x) + (\dot{v} + z\dot{\psi}_y)(\delta\dot{v} + z\delta\dot{\psi}_y) + (\dot{w}\,\delta\dot{w}) \big] \, d\mathrm{A}\, dz \tag{2.4.3}$$

Note that w_o does not contribute since it is constant in time. All the dependent variables in the integrand are independent of z. The following inertias can hence be defined

$$(I_1 , I_2 , I_3) = \int_{-h/2}^{h/2} \rho (1 , z , z^2) \, dz$$

As ρ is uniform for the laminate, $I_2 = 0$. Next, the kinetic energy term of Eq.(2.4.2) is integrated by parts with respect to time using the boundary conditions

$$\delta(U)_{t_1} = \delta(U)_{t_2} = 0$$

$$\delta(V)_{t_1} = \delta(V)_{t_2} = 0$$

$$\delta(W)_{t_1} = \delta(W)_{t_2} = 0$$

to obtain

$$\delta \int_{t_1}^{t_2} T\,dt = -\int_{t_1}^{t_2} \int_{\mathrm{A}} \left[I_1 \ddot{u}\,\delta u + I_1 \ddot{v}\,\delta v + I_1 \ddot{w}\,\delta w + I_3 \ddot{\psi}_x\,\delta\psi_x + I_3 \ddot{\psi}_y\,\delta\psi_y \right] d\mathrm{A}\,dt$$

Note that with I_3 not assumed zero rotatory inertia is included as stated in the assumptions. Upon substituting for displacements and rotations from Eqs.(2.2.2), in terms of nodal degrees of freedom and shape functions, the variation of kinetic energy can be written as

$$\delta \int_{t_1}^{t_2} T\,dt = -\int_{t_1}^{t_2} M_{ij}\,\ddot{a}_j\,\delta a_i\,dt \qquad i,j = 1,2,\ldots,N_{df} \tag{2.4.4}$$

where N_{df} includes the total number of global degrees of freedom for the system and M_{ij} is the mass matrix of the finite element model for the whole plate as given in Appendix B. It is understood that the area integration over the plate is actually the summation of element integrations, or assembly of finite element matrices, over all the elements in the finite element model.

The dissipative energy, D, is now represented in a similar way, as

$$\delta \int_{t_1}^{t_2} D\,dt = -\int_{t_1}^{t_2} C_{ij}\,\dot{a}_j\,\delta a_i\,dt \tag{2.4.5}$$

where C_{ij} is proportional to M_{ij}.

2.4.2 External Work

This term comprises the work done on the plate by the applied dynamic transverse load. If $\mathbf{p}(t)$ is the random dynamic pressure on the plate, then

$$\delta V = \int_{\mathrm{A}} -\mathbf{p}(t)\,\delta(w + w_o)\,d\mathrm{A}$$

Carrying out the variation and substituting for w from Eq.(2.2.2), the work done term in Hamilton's principle, Eq.(2.4.1) can be described as

$$\delta \int_{t_1}^{t_2} V\, dt \;=\; -\int_{t_1}^{t_2} P_i(t)\, \delta a_i^w\, dt \qquad i;j \;=\; 1,2,\ldots,N_{df} \tag{2.4.6}$$

where P_i is the load vector [see Appendix B]. The details of simulating this random load time-history are to be described in Chapter 4.

2.4.3 Strain Energy

The strain energy in a plate whose material shows linear Hookean behavior can be written in terms of its stresses and strains as

$$U \;=\; \int_{\mathrm{V}} \frac{1}{2}\, \sigma_i \epsilon_i\, d\mathrm{V}, \qquad\qquad i \;=\; 1,2,\ldots,6 \tag{2.4.7}$$

Using the constitutive relation for σ_i (Eq.2.3.3) and carrying out the variation, we have

$$\begin{aligned}
\delta U \;&=\; \delta \int_{\mathrm{V}} \frac{1}{2} \left[\, \bar{Q}_{ij}\, \epsilon_j \epsilon_i \;+\; \bar{Q}_{mn}\, \gamma_n \gamma_m \,\right] d\mathrm{V} \\
&=\; \int_{\mathrm{V}} \left[\, \bar{Q}_{ij} \epsilon_j\, \delta\epsilon_i \;+\; \bar{Q}_{mn} \gamma_n\, \delta\gamma_m \,\right] d\mathrm{V} \\
&=\; \int_{\mathrm{A}} \left[\, N_i\, \delta\,(\,\epsilon_i^m \;+\; \epsilon_i^w \;+\; \epsilon_i^o\,) \;+\; M_i\, \delta\kappa_i \;+\; Q_m\, \delta\gamma_m \,\right] d\mathrm{A}
\end{aligned} \tag{2.4.8}$$

where i takes on values 1, 2 and 6, and m takes on values 5 and 4.

Substituting for the stress resultants N_i, M_i, Q_m from Eqs.(2.3.9-11) and for the strains from Eqs.(2.2.6) the expression for the variation of strain energy now becomes

$$\begin{aligned}
\int_{\mathrm{A}} \Big\{ &\left[\, A_{ij}\,(\,\epsilon_j^m \;+\; \epsilon_j^w \;+\; \epsilon_j^o\,) \;+\; B_{ij}\kappa_j \;-\; N_i^{\Delta T} \;+\; N_i^s \,\right] \delta(\,\epsilon_i^m \;+\; \epsilon_i^w \;+\; \epsilon_i^o\,) \\
&+\; \left[\, B_{ij}\,(\,\epsilon_j^m \;+\; \epsilon_j^w \;+\; \epsilon_j^o\,) \;+\; D_{ij}\kappa_j \;-\; M_i^{\Delta T} \;+\; M_i^s \,\right] \delta\kappa_i \\
&+\; \mathcal{K}^2 A_{mn}\,(\,\gamma_n^\psi \;+\; \gamma_n^w\,)\, \delta(\,\gamma_m^\psi \;+\; \gamma_m^w\,) \Big\}\, d\mathrm{A}
\end{aligned} \tag{2.4.9}$$

$$= \int_A \Big\{ A_{ij}\epsilon_j^m \delta\epsilon_i^m + \underline{A_{ij}\epsilon_j^w \delta\epsilon_i^m} + A_{ij}\epsilon_j^o \delta\epsilon_i^m + B_{ij}\kappa_j \delta\epsilon_i^m + (N_i^s - N_i^{\Delta T})\delta\epsilon_i^m$$
$$+ \underline{A_{ij}\epsilon_j^m \delta\epsilon_i^w} + \underline{A_{ij}\epsilon_j^w \delta\epsilon_i^w} + \underline{A_{ij}\epsilon_j^o \delta\epsilon_i^w} + \underline{B_{ij}\kappa_j \delta\epsilon_i^w} + (N_i^s - N_i^{\Delta T})\delta\epsilon_i^w$$
$$+ A_{ij}\epsilon_j^m \delta\epsilon_i^o + \underline{A_{ij}\epsilon_j^w \delta\epsilon_i^o} + A_{ij}\epsilon_j^o \delta\epsilon_i^o + B_{ij}\kappa_j \delta\epsilon_i^o + (N_i^s - N_i^{\Delta T})\delta\epsilon_i^o$$
$$+ B_{ij}\epsilon_j^m \delta\kappa_i + \underline{B_{ij}\epsilon_j^w \delta\kappa_i} + B_{ij}\epsilon_j^o \delta\kappa_i + D_{ij}\kappa_j \delta\kappa_i + (M_i^s - M_i^{\Delta T})\delta\kappa_i$$
$$+ \mathcal{K}^2 \left(A_{mn}\gamma_n^\psi \delta\gamma_m^\psi + A_{mn}\gamma_n^w \delta\gamma_m^\psi + A_{mn}\gamma_n^\psi \delta\gamma_m^w + A_{mn}\gamma_n^w \delta\gamma_m^w \right) \Big\} dA \qquad (2.4.10)$$

where i, j range over 1,2,6 and m, n each take on values 5,4. The strain energy components that are functions of ϵ^w, are underlined so as to easily distinguish the geometrically nonlinear terms among all the above. Naturally, the one expression symmetric in ϵ^w forms the cubic nonlinear tensor in the a^w nodal displacements. The rest of the terms that depend on ϵ^w are quadratic functions of a^w.

The next step is to expand all the strains in terms of nodal displacements and the corresponding shape function matrices as in Eqs.(2.2.7-12). Once again the integration over the complete area of the plate is actually carried out by summing up the integrands of every element integration over the number of elements in the finite element model. The details of every element stiffness matrix and tensor generated as coefficients of nodal displacements are described in Appendix B.

2.5 Equations of Motion

With the various energy quantities for Hamilton's Principle now ready, they can be put together as follows to obtain the system governing differential equations of motion. Eq.(2.4.1) becomes

$$\int_{t_1}^{t_2} W(t) \Big\{ M_{ij}\ddot{a}_j + C_{ij}\dot{a}_j + \left(K_{ij} + K_{ij}^s - K_{ij}^{\Delta T}\right) a_j + K1_{ijk}\, a_j a_k$$
$$+ K2_{ijkl}\, a_j a_k a_l - P_i(t) + P_i^s - P_i^{\Delta T} \Big\} \delta a_i \, dt = 0 \qquad (2.5.1)$$

where

M_{ij}, C_{ij} are global mass and damping matrices;

K_{ij} is the global linear stiffness matrix (including w_o terms);

K^s_{ij} is the global stiffness matrix due to N^s;

$K^{\Delta T}_{ij}$ is the global stiffness matrix due to ΔT;

$K1_{ijk}$ is the global quadratic nonlinear tensor;

$K2_{ijkl}$ is the global cubic nonlinear tensor;

$P_i(t)$ is the global random load vector;

P^s_i is the global constant vector due to N^s (including w_o terms); and

$P^{\Delta T}_i$ is the global constant vector due to ΔT (including w_o terms).

All the above matrices and tensors are of order N_{df}. All of them, including those derived from the terms in Eq.(2.4.10), are detailed in Appendix B. All, including the two nonlinear tensors, are constants independent of displacements. The system is now ready for the imposition of kinematic boundary conditions.

The computational cost in satisfying a weighted average of the above multi-degree-of-freedom system over small time intervals until final time, t_2, will be astronomical. In order to circumvent this difficulty, the displacement vector, a_i, is represented in terms of a series expansion that is then suitably truncated. An appropriate choice for this truncated series approximation is a linear combination in the mode-shapes of free vibration for the plate.

The global system mass and linear stiffness matrices are used upon imposition of boundary conditions. The mode-shapes required are obtained from the solution to

$$M_{ij}\ddot{a}_j + K_{ij}a_j = 0 \qquad i;j = 1,2,\ldots,N_{df} - N_{bc} \tag{2.5.2}$$

where N_{bc} is the number of kinematic boundary conditions. This is the governing equation for undamped free vibration of the same structural system represented in

Eq.(2.5.1). The solution, a_j, to this system of equations is assumed to have the form

$$a_j(t) \;=\; \hat{a}_j e^{i\omega t}, \qquad\qquad i \;=\; \sqrt{-1}$$

Substituting this expression in Eq.(2.5.2), results in an eigenvalue system

$$\left[\, K_{ij} \;-\; \omega^2 \, M_{ij} \,\right] \hat{a}_j \;=\; 0 \tag{2.5.3}$$

that gives an array of eigenvalues, ω^2, which correspond to the natural frequencies of vibration for this system. However the *amplitudes* of vibration, $\hat{a}_j$ are indeterminate. Information regarding the *shape* of the response is still obtained by assigning one of the amplitudes as a fixed value, usually, unity. A scaled nondimensionalized expression of this amplitude vector for each eigenvalue is nothing but the eigenvector, also the mode-shape of the response at that eigenfrequency. By determining the mode-shape at each eigenfrequency, a square matrix consisting of all the mode-shapes can be written as follows

$$[\Phi] \;=\; [\,\{\phi_1\}\;\{\phi_2\} \quad \ldots \quad \{\phi_r\} \quad \ldots \quad]$$

where $\{\phi_r\}$ is the mode-shape corresponding to the r^{th} frequency of vibration and is directly proportional to $\hat{a}_j^r$. The degrees of freedom eliminated while imposing boundary conditions are now reinserted to make the number of rows in each eigenvector N_{df}. By doing this the boundary conditions are accounted for when transforming the system in Eqs.(2.5.1).

The matrix $[\Phi]$ is called the *modal transformation matrix* for the $N_{df} \times N_{df}$ system. This modal transformation matrix now can be used to form the series expansion for a_j as mentioned before, i.e.;

$$a_j \;=\; \phi_{j1}\, q_1(t) \;+\; \phi_{j2}\, q_2(t) \;+\; \ldots \;+\; \phi_{jr}\, q_r(t) \;+\; \ldots$$

where the *modal* or *normal coordinate*, q_r, gives the amplitude information at the r^{th} mode of vibration. These are the new unknowns to solve for in order to determine a_j.

The truncation, is in using a combination of a few of these modes, say, 3 to 6 (*much less than* N_{df}), to approximate all the N_{df} components of a_j. Physically, such an approximation would be consistent with the nature of vibration response of a structure. The dynamic response of a system to any kind of excitation is largely concentrated in the neighborhood of the first few natural frequencies of the system. Even when the random white noise excitation extends to high frequency regions, most of the energy in the response is distributed within the lower frequency range. Further, if it is known beforehand that there will be no response at particular natural frequencies due to the characteristics of the excitation, that corresponding modal coordinate may be dropped from the series approximation. In effect, the transformation to modal space lets one *tailor* the displacement assumption to suit the application. The exact considerations involved in choosing the appropriate modes to represent the system accurately will be discussed in Chapter 4 under implementation.

Thus, let's say R mode-shapes are used to express

$$a_j = \phi_{jr}\, q_r(t), \qquad j = 1,\ldots,N_{df}; \quad r = 1,\ldots,R; \quad R \ll N_{df} \tag{2.5.4}$$

Then

$$\dot{a}_j = \phi_{jr}\, \dot{q}_r(t) \tag{2.5.5}$$

and

$$\ddot{a}_j = \phi_{jr}\, \ddot{q}_r(t) \tag{2.5.6}$$

To obtain the reduced modal equations, the above transformations are substituted for the displacement, velocity and acceleration in Eq.(2.5.1), such that

$$M_{ij}\,\ddot{a}_j \;=\; M_{ij}\phi_{jr}\,\ddot{q}_r \;, \tag{2.5.7}$$

$$C_{ij}\,\dot{a}_j \;=\; C_{ij}\phi_{jr}\,\dot{q}_r \;, \tag{2.5.8}$$

$$\left(K_{ij} + K^s_{ij} - K^{\Delta T}_{ij}\right) a_j \;=\; \left(K_{ij} + K^s_{ij} - K^{\Delta T}_{ij}\right)\phi_{jr}\,q_r \;, \tag{2.5.9}$$

$$K1_{ijk}\,a_j a_k \;=\; K1_{ijk}\phi_{jr}\phi_{ks}\,q_r q_s \;, \qquad \text{and} \tag{2.5.10}$$

$$K2_{ijkl}\,a_j a_k a_l \;=\; K2_{ijkl}\phi_{jr}\phi_{ks}\phi_{lt}\,q_r q_s q_t \tag{2.5.11}$$

where r, s, t now range from 1,..., R. In addition, to reduce the matrices in their i coordinate (which still goes from 1,..., N_{df}), the whole equation in Eq.(2.5.1) is premultiplied by the transpose of $[\Phi]$. If ϕ_{ip} is used to denote the transpose (index i must be used this way, to be consistent with the index in all the system matrices), then Eq.(2.5.1), upon substitution of Eqs.(2.5.7-11) and multiplication, becomes

$$\begin{aligned}\int_{t_1}^{t_2} W(t) \Big\{ & \left[M_{ij}\phi_{jr}\phi_{ip}\right]\ddot{q}_r \;+\; \left[C_{ij}\phi_{jr}\phi_{ip}\right]\dot{q}_r \\ & + \left[\left(K_{ij} + K^s_{ij} - K^{\Delta T}_{ij}\right)\phi_{jr}\phi_{ip}\right] q_r \\ & + \left[K1_{ijk}\phi_{jr}\phi_{ks}\phi_{ip}\right] q_r q_s \\ & + \left[K2_{ijkl}\phi_{jr}\phi_{ks}\phi_{lt}\phi_{ip}\right] q_r q_s q_t \\ & - P_i(t)\phi_{ip} \;+\; P^s_i\phi_{ip} \;-\; P^{\Delta T}_i\phi_{ip} \Big\}\, dt \;=\; 0 \end{aligned} \tag{2.5.12}$$

It must be clarified that unlike in the case of the familiar matrix notation it is not required for ϕ_{ip} to be placed *before* the matrices it 'premultiplies'. All that is essential in the index notation is for the index assignments to be consistent so that the right elements of two matrices multiply each other.

Therefore, the final form of Eq.(2.5.1) transformed, and thereby reduced, from the global system physical degrees of freedom to the new modal degrees of freedom-can be now written as

$$\int_{t_1}^{t_2} W(t) \left\{ m_{pr}\ddot{q}_r + c_{pr}\dot{q}_r + \left(k_{pr} + k^s_{pr} - k^{\Delta T}_{pr}\right) q_r \right.$$

$$\left. + k1_{prs}\, q_r\, q_s + k2_{prst}\, q_r\, q_s\, q_t - p_p(t) + p^s_p - p^{\Delta T}_p \right\} dt = 0 \quad (2.5.13)$$

where p, r, s, t range from $1, \ldots, R$.

The matrices m_{pr}, c_{pr}, k_{pr}, ..., etc. are the modal equivalents of the global system matrices as shown in Eq.(2.5.12) above. In actual implementation the modal transformations are not done at the global level. There is no possibility of storing an $N_{df} \times N_{df} \times N_{df} \times N_{df}$ cubic tensor on most machines and neither is it efficient. Instead, transformations are carried out at a much smaller element individual degrees-of-freedom-level. Details of the implementation process will be discussed in Chapter 4.

This is the set of equations that will be integrated from initial to final time. The solution vector $q_r(t)$ obtained is then used to approximate the displacement vector, a_j, as in Eq.(2.5.4).

Chapter 3

NUMERICAL INTEGRATION

The integration technique used to march forward in time is described here. A single step algorithm, as put forth by Zienkiewicz et al. [114], has been adapted to generate a system of nonlinear algebraic equations that are solved iteratively within each time-step. The salient features of this procedure are detailed in the following sections.

3.1 Single Step Algorithm

Within a single time-step, say, between time t_n and t_{n+1}, the modal coordinate, q, is expressed as a polynomial series of degree p, in τ, as follows

$$q(\tau) = \sum_{m=0}^{p-1} \frac{d^m q_n}{d\tau^m} + \alpha_n^{(p)} \frac{\tau^p}{p!} \tag{3.1.1}$$

with

$$t_{n+1} = t_n + \Delta t \quad \text{and} \quad 0 \leq \tau \leq \Delta t$$

Or, on expansion,

$$q(\tau) = q_n + \dot{q}_n \tau + \ddot{q}_n \frac{\tau^2}{2!} + \ldots + \alpha_n{}^{(p)} \frac{\tau^p}{p!} \tag{3.1.2}$$

the dot denoting differentiation with respect to time. This series expression for $q(\tau)$ is exact.

For a second order system of differential equations, with initial displacement and velocity being the natural initial conditions, a cubic degree polynomial is the lowest applicable. Any polynomial of higher degree requires initial conditions for higher derivatives of $q(\tau)$ and does not have unconditional stability characteristics even for a linear system. So, when degree of polynomial in Eq.(3.1.2), $p = 3$,

$$\begin{aligned} q_{n+1} &= q_n + \dot{q}_n \tau + \ddot{q}_n \frac{\tau^2}{2!} + \alpha_n{}^{(3)} \frac{\tau^3}{6} \\ \dot{q}_{n+1} &= \dot{q}_n + \ddot{q}_n \tau + \alpha_n{}^{(3)} \frac{\tau^2}{2} \\ \ddot{q}_{n+1} &= \ddot{q}_n + \alpha_n{}^{(3)} \tau \end{aligned} \tag{3.1.3}$$

When $\tau = \Delta t$, this becomes

$$\begin{aligned} q_{n+1} &= q_n + \dot{q}_n \Delta t + \ddot{q}_n \frac{\Delta t^2}{2!} + \alpha_n{}^{(3)} \frac{\Delta t^3}{6} \\ &= \tilde{q}_n + \alpha_n{}^{(3)} \frac{\Delta t^3}{6} \\ \dot{q}_{n+1} &= \dot{q}_n + \ddot{q}_n \Delta t + \alpha_n{}^{(3)} \frac{\Delta t^2}{2} \\ &= \dot{\tilde{q}}_n + \alpha_n{}^{(3)} \frac{\Delta t^2}{2} \\ \ddot{q}_{n+1} &= \ddot{q}_n + \alpha_n{}^{(3)} \Delta t \\ &= \ddot{\tilde{q}}_n + \alpha_n{}^{(3)} \Delta t \end{aligned} \tag{3.1.4}$$

which can be generalized as

$$\{\mathbf{q}\}_{n+1} = \{\tilde{\mathbf{q}}\}_n + \{\alpha\}_n$$

where the right-hand sides above consist of a known function from the previous time-step, $\{\tilde{\mathbf{q}}\}_n$, analogous to a 'predictor', and the unknown $\{\alpha\}_n$, the 'corrector'. This corrector, with the only unknown, $\alpha_n{}^{(3)}$, is determined by a weighted satisfaction of the modal system of equations, Eqs.(2.5.13), over every time-step. The weighting function, W, is defined such that

$$\frac{\int_0^{\Delta t} W(\tau)\tau^m \, d\tau}{\int_0^{\Delta t} W(\tau) \, d\tau} = \theta_m \Delta t^m \tag{3.1.5}$$

where θ_m are free parameters chosen based on stability criteria. These parameters can correspond to any of the various numerical integration algorithms such as the Houbolt algorithm, the Bossack-Newmark algorithm, the Wilson-θ algorithm, etc. In this work the θ_m values were chosen based on the Wilson-θ integration algorithm [137]. For a second order linear system, the cubic algorithm ($p = 3$) needs three free parameters, θ_1, θ_2, θ_3, which for Wilson's algorithm, take on the following values

$$\begin{aligned} \theta_1 &= \theta_W \\ \theta_2 &= {\theta_W}^2 \\ \theta_3 &= {\theta_W}^3, \qquad \theta_W \geq 1.366 \end{aligned} \tag{3.1.6}$$

where θ_W corresponds to the Wilson-θ parameter. The convenient fashion in which the three free parameters above are defined in terms of the Wilson-θ parameter is the reason this algorithm was chosen over the others. This is particularly useful for the nonlinear system we have, where the quadratic and cubic terms in $q(t)$ when expressed in terms of Eqs.(3.1.3), will result in more than three free parameters (see Appendix C). Thus for the nonlinear system of equations, the definitions in Eqs.(3.1.6) are extended as follows

$$\theta_m = {\theta_W}^m, \qquad m = 1, 2, \ldots, 3p \quad \textit{and} \quad \theta_0 = 1 \tag{3.1.7}$$

In our case $3p$ is 9.

The only other function of time in the weighted integral equation (2.5.13) is the dynamic load, $p(t)$, which needs to be interpolated appropriately within the time

interval, Δt. It is reasonable to approximate that it varies linearly between t_n and t_{n+1} to give

$$\bar{p}_n(t) \;=\; \theta_1\, p(t_{n+1}) \;+\; (1 - \theta_1)\, p(t_n) \tag{3.1.8}$$

The system of modal equations in Eqs.(2.5.13) is now rewritten with Eqs.(3.1.3) substituted for the unknown modal coordinates, $q(t)$. The resulting expression and its integration is detailed in Appendix C. As shown in Appendix C, after integration has been carried out, the quantity $\alpha_n^{(3)}$ is replaced by a new variable defined as

$$d_n \;=\; \alpha_n^{(3)}\, \frac{\Delta t^3}{6} \tag{3.1.9}$$

This has been done for the sake of implementation. For a random dynamic problem, $\alpha_n^{(3)}$, analogous to the rate of change of acceleration, is a very large quantity and Δt is usually a small quantity. By solving for d_n we are dealing with quantities on the order of displacements and are directly obtaining the increments in modal displacement, $q(t)$.

Thus the numerical integration algorithm used herein results in a set of *coupled nonlinear algebraic* equations in d as given below.

$$A2_{ijkl}\, d_j\, d_k\, d_l \;+\; A1_{ijk}\, d_j\, d_k \;+\; A_{ij}\, d_j \;+\; A0_i \;\equiv\; \Psi_i(d) \;=\; 0 \tag{3.1.10}$$

where

$A2_{ijkl}$ – arises out of the cubic modal tensor, $k2_{ijkl}$

$A1_{ijk}$ – arises out of quadratic functions of d_j in $k2_{ijkl}$ and the quadratic modal tensor, $k1_{ijk}$

A_{ij} – arises out of linear functions of d_j in $k2_{ijkl}$ and $k1_{ijk}$; the linear modal stiffness matrices, k_{ij}, k_{ij}^s, $k_{ij}^{\Delta T}$; and the mass and damping matrices, M_{ij} and C_{ij}

$A0_i$ – arises out of all the constant terms from all the above tensors and matrices that are functions of solutions from the previous time-step, $\{\tilde{\mathbf{q}}\}$, as well as from the modal load vectors at the current time-step, $\bar{p}_i(t)$, $p_i^{\Delta t}$ and p_i^s.

3.2 Iteration Procedure

The solution procedure for the nonlinear equations obtained above can be chosen to suit the degree of nonlinearity of the problem. When a system is weakly nonlinear it may be sufficient to solve a linearized set of equations at every time-step, using the solution from the previous time-step. In this work, however, nonlinear equations are retained, so as not to restrict the scope of this formulation to problems with small nonlinearities. Accordingly, the well-known Newton-Raphson iterative scheme has been utilized within each time-step.

If it is required that Eqs.(3.1.10) be satisfied at the $(p+1)^{th}$ iteration, then we can write

$$\Psi_i^{p+1}(d) \equiv 0$$

which can be expanded as a Taylor's series about Ψ_i from the p^{th} iteration as follows

$$\Psi_i^{p+1}(d) = \Psi_i^p(d) + \frac{\partial \Psi_i^p}{\partial d_r} \Delta d_r + \quad \ldots \quad \equiv 0 \tag{3.2.1}$$

By truncating this series to second-order errors, the above is rewritten as

$$\frac{\partial \Psi_i^p}{\partial d_r} \Delta d_r^p = -\Psi_i^p(d)$$

i.e.,

$$K_{ir}^T(d^p)\,\Delta d_r^p = -\Psi_i^p(d) \tag{3.2.2}$$

where

$$d_r^{p+1} = d_r^p + \Delta d_r^p \tag{3.2.3}$$

and K_{ir}^T is the *tangent stiffness matrix*.

It is obtained by substitution of Eqs.(3.1.10) and differentiation (as in Appendix B). i.e.,

$$K_{ir}^T \Delta d_r^p = \frac{\partial \Psi_i^p}{\partial d_r} \Delta d_r^p$$

$$= \frac{\partial}{\partial d_r} \left[A2_{ijkl}\, d_j^p\, d_k^p\, d_l^p + A1_{ijk}\, d_j^p\, d_k^p + A_{ij}\, d_j^p + A0_i(\tilde{\mathbf{q}}) \right] \Delta d_r^p$$

$$= \left\{ \left[A2_{irkl} + A2_{ilrk} + A2_{iklr} \right] d_k^p\, d_l^p \right.$$

$$\left. + \left[A1_{irk} + A1_{ikr} \right] d_k^p + A_{ir} \right\} \Delta d_r^p \qquad (3.2.4)$$

The corresponding right-hand side vector, $-\Psi_i^p$, is computed using d_r^p and the new system of equations in Eqs.(3.2.2) is iteratively solved for Δd_r^p. The value of d_r^{p+1} is now updated using Eqs.(3.2.3). The iterations are carried out until a certain convergence level is met. Convergence is said to have been achieved when the error between solutions of two successive iterations is within some predetermined bound. The error norm chosen here is the maximum norm. i.e.,

$$max \left| \frac{d_r^{p+1} - d_r^p}{d_r^{p+1}} \right| \leq err \qquad (3.2.5)$$

where err is a sufficiently small positive number.

The startup of the iterations needs a suitable guess value, which in this case can either be zero (giving the linear solution at every time-step) or the modal displacement from the previous time-step, $\tilde{q}_n$.

Chapter 4

IMPLEMENTATION AND SOLUTION PROCEDURE

The previous two chapters have described how the plate vibration problem has been modelled. In order to proceed with solutions to specific problems various preparatory computations need to be carried out. These include solving eigensystems to determine the fundamental frequency, the modal transformation matrix as well as the critical buckling temperature all of which are subsequently required. Apart from these, time-histories of random gaussian acoustic pressure distributions at different decibel levels need to be generated. Furthermore, post-processing of the resultant displacement and strain time-histories requires computation of the power spectra, the probability distributions and also the various statistical parameters such as mean, variance and other higher order moments. This chapter deals with these above-mentioned aspects and certain implementational considerations that need to be highlighted. The load generation details will be discussed first.

4.1 Random Load Generation

Since we are dealing with a *random stationary process*, a Monte Carlo simulation is used to generate the random pressure time-history. A Monte Carlo simulation evaluates the required function at a number of sample points all lying within some domain of interest. These values are then used to represent a close approximation

of the actual function itself. The error in the estimate of the function is greatly dependent on the number of samples used.

The pressure time-history is a filtered normal distribution whose sound pressure level (SPL) is suitably scaled. A *uniform* random array of numbers is first created. This uniform array is then transformed to a normal distribution of numbers with zero mean and variance unity. The method used is the *KR algorithm* as given by Kinderman and Ramage [138].

4.1.1 Filtered Random Process

The array of normally distributed numbers, $\mathbf{Y}$, is passed through a recursive linear filter. The filtering process is based on the *bilinear transformation method* [139]. This technique maps the frequencies, f, into a new variable, w, using the equation

$$w \equiv tan[\pi(f\Delta t)] \tag{4.1.1}$$

where Δt is the sampling interval or time-step. This results in a frequency response function for the filter as follows

$$|H(f)|^2 = \left(\frac{w^2}{w^2 + a^2}\right)\left(\frac{b^2}{w^2 + b^2}\right) \tag{4.1.2}$$

where w is as defined in Eq.(4.1.1), and a and b are the values of w corresponding to the lower cut-off frequency, f_l, and the upper cut-off frequency, f_u, respectively.

The filtered process can be represented as

$$\mathbf{X_n} = \sum_{k=0}^{m} c_k \mathbf{Y_{n-k}} + \sum_{j=1}^{n} d_j \mathbf{X_{n-j}} \tag{4.1.4}$$

where there are $m+1$ coefficients c_k and n coefficients d_j that are constant for the filter and define the relationship between the broadband input, $\mathbf{Y_k}$ and the filtered

output $\mathbf{X_n}$. These constants are determined using the poles of Eq.(4.1.2) that result in a stable $H(f)$. They are

$$
\begin{aligned}
c_0 &= -\frac{b}{(1+a)(1+b)} \\
c_1 &= 0 \\
c_2 &= \frac{b}{(1+a)(1+b)} \\
d_1 &= \frac{(1+a)(1-b)+(1-a)(1+b)}{(1+a)(1+b)} \\
d_2 &= -\frac{(1-a)(1-b)}{(1+a)(1+b)}
\end{aligned}
\tag{4.1.5}
$$

With these constants and the input array, $\mathbf{Y}$, we can generate the output filtered, *band-limited* process, $\mathbf{X}$, using Eq.(4.1.4). This filter as such does not produce sharp cut-offs. The filtering process can be repeated until the desired drop-off is achieved.

The filtered process, $\mathbf{X}$, now needs to be scaled to a *gaussian pressure time-history*. In order to do this the *root mean square* value of the pressure distribution, p_{rms}, needs to be computed. If the level of the acoustic pressure, supplied in decibels, dB, is SPL, then

$$p_{av}^2 = p_{ref}^2 10^{SPL/10} \tag{4.1.6}$$

is the magnitude of the power spectrum levels for the broadband gaussian acoustic pressure distribution, in psi^2/hz. It is a constant through the frequency spectrum. The reference pressure level is p_{ref}. The expression for p_{rms} is therefore given by

$$p_{rms}^2 = \int_{f_l}^{f_u} |H(f)|^{2\,nf}\, p_{av}^2\, df \tag{4.1.7}$$

where nf is the number of filters used. The limits f_l and f_u are as defined before. When nf is 1, the expression reduces to the familiar mean-square relationship between any input and output process. As mentioned earlier, the filtering process needs to be repeated in order to produce a more 'ideal' band-limited output which has a steep drop-off at f_u. This repetition is equivalent to applying the magnitude of the frequency response function, $|H(f)|^2$, nf number of times. Hence the equation for mean-square of the output process is as given in Eq.(4.1.7) above.

The pressure time-history vector is thus obtained by

$$\mathbf{p} = p_{rms}\,\mathbf{X} + \mu \tag{4.1.8}$$

where μ is the bias or mean, if any. The notation $\mathbf{p}$ stands for an array of acoustic pressure values. It represents

$$\mathbf{p} = \{\, p(t_1) \quad p(t_2) \quad \dots \quad p(t_N) \,\}^T \equiv \{\, p_1 \quad p_2 \quad \dots \quad p_N \,\}^T$$

which is the expression for pressure used in deriving Eq.(2.4.6). The subscript N here denotes the final time-step in the time-marching scheme.

4.1.2 Normal Random Load

The random *pressure* time-history is now ready. The *load* on the plate must now be computed. This load is modelled in two ways. The simpler of the two, due to waves along the z-axis, perpendicular to the surface of the plate, is treated as being due to uniform pressure over the whole surface area at any given time. This model will be dealt with first.

The global load vector corresponding to unit pressure, $\{F\}$, is defined in Eq.(2), Appendix B. It will be used here as F_i, where subscript i ranges over the global

degree of freedom numbers. As shown in the same equation, Eq.(2), the final form of the global load vector is given by

$$P_i^n(t) \;=\; \mathbf{p}_n(t)\, F_i\,, \qquad\qquad i = 1,2,\ldots,N_{df}, \quad \text{and} \quad n = 1,2,\ldots,N \quad (4.1.9)$$

It must be made clear that N_{df} is the total number of degrees of freedom in the global system and N is the total number of time-steps. This is the load vector, $P_i(t)$, used in Eq.(2.5.1). It is obtained simply by scaling F_i by the p_{rms} value from the vector $\mathbf{p}$ for the corresponding time-step.

The entire formulation so far has been based on this load model. At a particular time-step, a *single* p_{rms} value is used over the whole plate. But if the waves were incident at an angle to the plate, say tangential to the surface, then this would no longer be an accurate model.

4.1.3 Space-Time Correlation

A pressure field at an angle to the plate is treated as a series of plane waves incident on the plate at a certain angle, β, as shown in Fig.3. It is assumed that the waves travel from left to right over the plate. Therefore the spatial direction of interest is along the x-axis only. The pressure distribution along the y-direction is restricted to being uniform.

The above plane wave acoustic pressure field satisfies the one-dimensional wave equation. The d'Alembert solution to the wave equation results in an expression for the pressure, p, at any point as follows (outgoing wave term only)

$$p \;=\; p\big(t \;-\; \frac{s}{c}\big) \qquad (4.1.10)$$

where s is the distance measured *along wave direction*; c is the speed of sound in air.

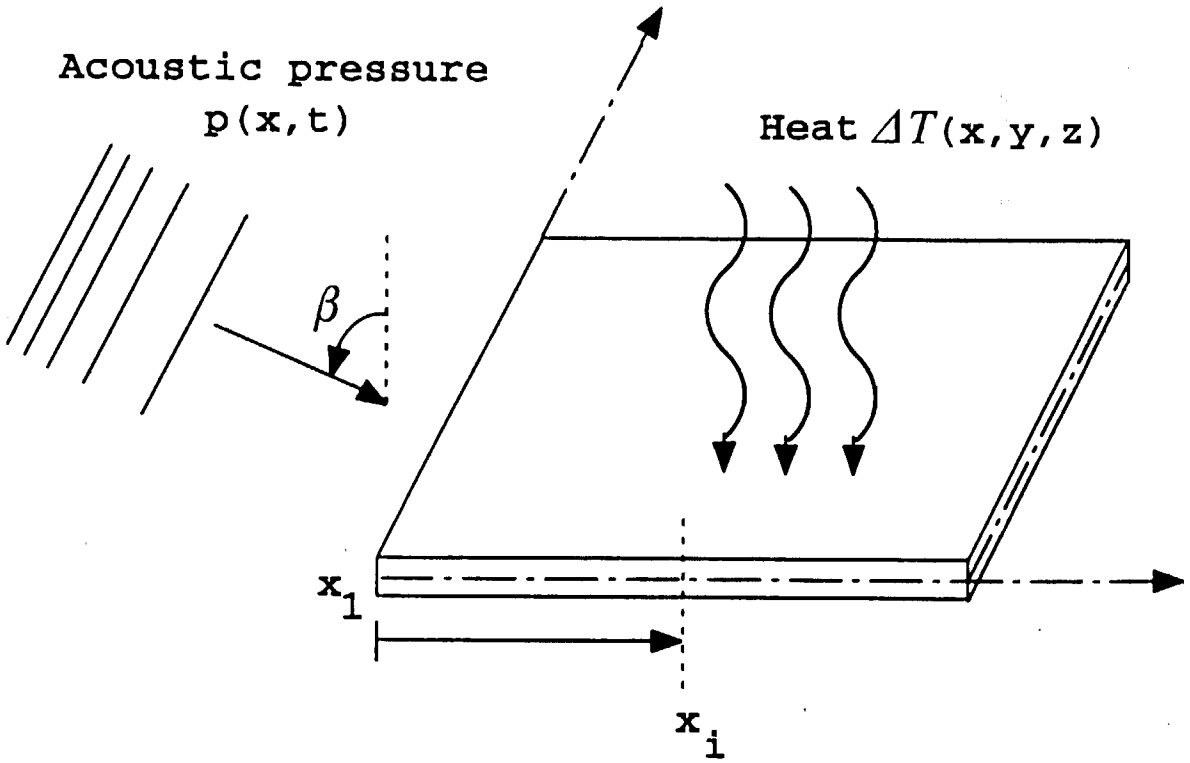

Fig.3 Loading Conditions of the Plate

In terms of the plate coordinate x, this becomes

$$p = p\left(t - \frac{x\,sin\beta}{c}\right) \tag{4.1.11}$$

This expression essentially correlates pressure values along the $x-$axis with time. The time-lag in travelling a distance x is given by $xsin\beta/c$. In other words, the magnitude of pressure at the 'leading edge' is the same as the magnitude at a distance x from the leading edge after a time interval $xsin\beta/c$.

Thus in order to create the global *correlated* pressure vector over the surface of the plate, we first define a global array, g_k, as follows

$$g_k = \textbf{integer}\left[\frac{x_k\,sin\beta/c}{\Delta t}\right], \qquad k = 1,2,\ldots,N_N \tag{4.1.12}$$

where N_N is the number of nodes in the mesh ($N_{df} = 5N_N$). This array contains the *integer values* of the time-lag in multiples of the time-step, Δt. For example, let

$$g_k = \{0 \quad 0 \quad 1 \quad 2 \quad 2 \quad 3 \quad 4 \quad \ldots\}^T$$

correspond to global nodal x-coordinate values

$$x_k = x_1,\ x_2,\ x_3,\ x_4,\ x_5,\ x_6,\ \cdots\ , \qquad x_1 \equiv 0.0$$

In this instance, node 3 at a distance x_3 from node 1 has a corresponding g_3 value of 1. This implies that the time-lag in a wave travelling from node 1 to node 3 is approximately equal to Δt. Similarly, a wave reaches node 4 after a time span of $2\Delta t$ seconds.

With this array, g_k, defined, the load vector at the n^{th} time-step can now be determined. Using the same notation as in section 4.1.2, it can be written as

$$P_i^n(t) = \mathbf{p}_{n-g_k}(t)\,F_i\,, \qquad i = 1,2,\ldots,N_{df}, \qquad k = 1,2,\ldots,N_N \tag{4.1.13}$$

with $\mathbf{p}_{n-g_k} = 0$ for all $n - g_k < 0$ (negative subscripts).

Note that the subscript i represents the global degree of freedom number whereas k stands for the global *node* number. It is understood that g_k values remain unchanged for all the five degrees of freedom at one particular node. Again the example from above is used to explain Eq.(4.1.13). For the degrees of freedom corresponding to the first four nodes, whose x-coordinates are x_1, x_2, x_3, x_4, and g_k values are 0,0,1,2 respectively, the final form of P_i at the n^{th} time-step is

$$\begin{Bmatrix} P_1 \\ P_2 \\ P_3 \\ P_4 \\ P_5 \\ \\ \vdots \\ \\ \\ \vdots \\ \\ \\ \vdots \\ \\ \\ P_{18} \\ P_{19} \\ P_{20} \end{Bmatrix} = \begin{Bmatrix} 0 \\ 0 \\ \mathbf{p}_n F_3 \\ 0 \\ 0 \\ \\ 0 \\ 0 \\ \mathbf{p}_n F_8 \\ 0 \\ 0 \\ \\ 0 \\ 0 \\ \mathbf{p}_{n-1} F_{13} \\ 0 \\ 0 \\ \\ 0 \\ 0 \\ \mathbf{p}_{n-2} F_{18} \\ 0 \\ 0 \end{Bmatrix}$$

The elements of P_i and F_i are grouped as 5 degrees of freedom per node, with the entries corresponding to the a^w degree of freedom being the only non-zero entries. i.e., $F^w \neq 0$, and $F^u = F^v = F^{\psi_x} = F^{\psi_y} = 0$.

Thus, Eq.(4.1.13) gives the expression for the *correlated* random load vector. Had the angle of incidence, β, been zero, implying normal incidence, all g_k values would have been zero, resulting in Eq.(4.1.9) for $P_i(t)$.

4.2 Implementation

As mentioned earlier, the preparatory computations that need to be carried out include the determination of the modal transformation matrix and the corresponding eigenvalues. The appropriate 'modes' or eigenvectors are extracted from this matrix to represent the relevant degrees of freedom in the response of the plate system.

It is extremely important that care be exercised in choosing the appropriate modes to represent the structural response adequately. There are particularly significant factors which influence the choice of mode-shapes during implementation. Important considerations are the damping, spacing between modes and the frequency range of interest. Also to be included are the properties of the plate, the type of dynamic loading and the nature of the stiffness matrix, $[K]$. The last will be discussed in detail in the following sub-sections.

The geometry of the plate and the boundary conditions on its edges affect the frequency content in the vibration response of the plate. There are two planes of symmetry of concern, namely, the $x-z$ and $y-z$ planes. If the plate were to be a simple rectangular symmetric laminate with symmetric boundary conditions, then it is symmetric about both these planes. Its response to a normal random load would be restricted to modes that are symmetric in x and y-coordinates. In the case of a load that is correlated along the x-coordinate as described in section 4.1.3, the only plane of symmetry is the $x-z$ plane even for a fully symmetric plate. This still permits the use of a half-plate model, and correspondingly, mode-shapes that are symmetric in the y-coordinate. For the case of a plate that has no plane of symmetry as in the case of mixed boundary conditions or non-rectangular plates, no assumptions in choosing mode-shapes can be made. All the predominant lower modes may need to be included.

4.2.1 Uncoupled Linear Stiffness Matrix

In Eq.(30) of Appendix B, the element linear stiffness matrix, $[K^e]$, is a fully loaded matrix only if bending-extension coupling, arising due to matrix B_{ij} in the laminate stiffnesses, and initial imperfection, $w_o(x,y)$, are non-zero. In the case both are zero,

$$[K^e] = \begin{bmatrix} k^{mm} & 0 & 0 \\ 0 & ks^{ww} & ks^{w\psi} \\ 0 & ks^{\psi w} & k^{\psi\psi} + ks^{\psi\psi} \end{bmatrix}$$

where the membrane displacement sub-matrix, $[k^{mm}]$, is completely independent of the other sub-matrices that correspond to bending and curvature. In this case when solving Eq.(2.5.2)

$$M_{ij}\ddot{a}_j + K_{ij}a_j = 0, \qquad i;j = 1,2,\ldots,N_{df} - N_{bc}$$

at the global level, to obtain the transformation matrix, $[\Phi]$, the eigenvectors corresponding to inplane displacements, $\{a^m\}$, will be independent of those corresponding to bending and curvature, $\{a^w\}, \{a^\psi\}$. Thus it is important that $\{a^m\}$ be represented by an adequate number of its eigenvectors in the truncated series for a_j, Eq.(2.5.4).

In effect, for the case of an uncoupled stiffness matrix, Eq.(2.5.2) splits to two smaller systems as follows

$$[M^{mm}]\{\ddot{a}^m\} + [K^{mm}]\{a^m\} = 0 \quad (4.2.1)$$

and

$$\begin{bmatrix} M^{ww} & 0 \\ 0 & M^{\psi\psi} \end{bmatrix} \begin{Bmatrix} \ddot{a}^w \\ \ddot{a}^\psi \end{Bmatrix} + \begin{bmatrix} Ks^{ww} & Ks^{w\psi} \\ Ks^{\psi w} & K^{\psi\psi} + Ks^{\psi\psi} \end{bmatrix} \begin{Bmatrix} a^w \\ a^\psi \end{Bmatrix} = 0 \quad (4.2.2)$$

The global sub-matrices used in this equation are used as direct assembled extensions of the element sub-matrices defined in Appendix B. Solutions of these two

eigenvalue systems result in expressions for the nodal degrees of freedom as given below

$$\{a^m\} = [\Phi^m]\{q^m\} \tag{4.2.3}$$

$$\begin{Bmatrix} a^w \\ a^\psi \end{Bmatrix} = [\Phi^{(w\psi)}]\{q^{(w\psi)}\} \tag{4.2.4}$$

where $[\Phi^m]$ is the modal matrix for the membrane system, Eq.(4.2.1), and $\{q^m\}$ are the corresponding membrane modal coordinates. Similarly, $[\Phi^{(w\psi)}]$ is the modal matrix for the bending system (a^w, a^ψ) and $\{q^{(w\psi)}\}$ its modal coordinates. The equations above imply that the following series expressions can each be truncated to represent the membrane and bending degrees of freedom, respectively.

$$\{a^m\} = \{\phi^m\}_1 q_1^m + \{\phi^m\}_2 q_2^m + \{\phi^m\}_3 q_3^m + \cdots$$

and

$$\begin{Bmatrix} a^w \\ a^\psi \end{Bmatrix} = \{\phi^{(w\psi)}\}_1 q_1^{(w\psi)} + \{\phi^{(w\psi)}\}_2 q_2^{(w\psi)} + \{\phi^{(w\psi)}\}_3 q_3^{(w\psi)} + \cdots$$

These two equations when put together in matrix form result in

$$\begin{Bmatrix} \{a^m\} \\ \begin{Bmatrix} a^w \\ a^\psi \end{Bmatrix} \end{Bmatrix} = \left[\begin{Bmatrix} \{\phi^m\}_1 \\ 0 \end{Bmatrix} \begin{Bmatrix} \{\phi^m\}_2 \\ 0 \end{Bmatrix} \cdots \begin{Bmatrix} 0 \\ \{\phi^{(w\psi)}\}_1 \end{Bmatrix} \begin{Bmatrix} 0 \\ \{\phi^{(w\psi)}\}_2 \end{Bmatrix} \cdots \right] \times \begin{Bmatrix} q^m \\ q^{(w\psi)} \end{Bmatrix} \tag{4.2.5}$$

which is the same as

$$\{a\} = [\{\phi\}_1 \quad \{\phi\}_2 \quad \{\phi\}_3 \quad \{\phi\}_4 \quad \cdots] \begin{Bmatrix} q_1 \\ q_2 \\ \vdots \end{Bmatrix}$$

The length of each mode-shape vector, $\{\phi\}$, is $N_{df} - N_{bc}$. They are brought back up to length N_{df} by inserting the kinematic boundary conditions at the appropriate degrees of freedom. Then the transformation is similar in form to Eq.(2.5.4) repeated here for reference

$$a_j = \phi_{jr}\, q_r(t), \qquad j = 1,2,\ldots,N_{df}, \qquad r = 1,2,\ldots,R; \quad R \ll N_{df}$$

The actual number of modes used, R, is decided based on convergence studies for both the menbrane and bending modes, done separately. The minimum number of membrane modes required for each problem is determined based on the convergence of solutions with increasing number of modes. Once that is fixed, those bending modes over which a significant response level is observed are retained and the rest discarded. This is again done by checking the convergence of solutions.

For plates with stiffness matrices as discussed above (symmetric laminates), there are associated buckling problems. A buckling eigenvalue problem is solved to determine the critical buckling temperatures using the equation

$$\left[K_{ij} - K_{ij}^{\Delta T}\right] a_j = 0 \tag{4.2.6}$$

where a nominal value of ΔT is used to compute $K_{ij}^{\Delta T}$. The critical buckling temperature is determined by scaling the ΔT value used, with the lowest eigenvalue. These buckling temperatures are used to evaluate the response of a plate under thermal and acoustic loads around these critical values.

4.2.2 Coupled Linear Stiffness Matrix

In the case of a laminate with non-zero bending-extension coupling ($B_{ij} \neq 0$) and/or with a prescribed initial imperfection, $w_o(x,y)$, the element linear stiffness matrix, $[K^e]$, has the form

$$[K^e] = \begin{bmatrix} k^{mm} & k^{mo} & k^{m\psi} \\ k^{om} & k^{oo} + ks^{ww} & k^{o\psi} + ks^{w\psi} \\ k^{\psi m} & k^{\psi o} + ks^{\psi w} & k^{\psi\psi} + ks^{\psi\psi} \end{bmatrix}$$

as given in Appendix B. The sub-matrices in the membrane positions, $[k^{mo}]$ and $[k^{om}]$ arise due to $w_o(x,y)$, and $[k^{m\psi}]$ and $[k^{\psi m}]$ arise due to B_{ij}. Either way, the membrane components in $[K^e]$ are no longer independent of the bending components. In this case, therefore, the complete *coupled* system given in Eq.(2.5.2) is solved to give

$$\begin{Bmatrix} a^m \\ a^w \\ a^\psi \end{Bmatrix} = [\{\phi\}_1 \quad \{\phi\}_2 \quad \{\phi\}_3 \quad \{\phi\}_4 \quad \ldots] \begin{Bmatrix} q_1 \\ q_2 \\ q_3 \\ \vdots \end{Bmatrix} \tag{4.2.7}$$

which is in the same form as Eq.(2.5.4). The required number of modes are used again based on modal convergence studies of solutions to the random vibration problem.

4.2.3 Assembly of Modal Matrices

Once the required modal transformation matrix is ready, all the matrices and tensors in the random vibration problem need to be reduced to their modal equivalents. As stated at the end of chapter 2, it is physically impossible to assemble $K1_{ijk}$ or $K2_{ijkl}$ to the global *nodal* degrees of freedom level. In fact it is impractical even at the *element* assembly level to store, say, $K1^e_{ijk}$, as a $45 \times 45 \times 45$ tensor. Therefore, at the programming stage, the modal matrices and tensors are all prepared at the element *sub-matrix* level. For instance, $[k2^{ww}]$, a $9 \times 9 \times 9 \times 9$ tensor for the a^w degree of freedom is transformed to its modal counterpart as follows

$$[k2^{ww}]^{modal} = [\phi^{w^e}]^T [k2^{ww}] [\phi^{w^e}][\phi^{w^e}][\phi^{w^e}]$$

and, likewise

$$[k1^{mw}]^{modal} = [\phi^{m^e}]^T [k1^{mw}] [\phi^{w^e}][\phi^{w^e}] \tag{4.2.8}$$

where $[\phi^{w^e}]$ and $[\phi^{m^e}]$ contain the element modal transformation matrix components for the a^w and a^m degrees of freedom, respectively. All the other element sub-matrices defined in Appendix B, are transformed to their modal equivalents in a similar fashion. Once all the stiffness, mass and thermal matrices and tensors are in modal form, they are then assembled at element level. Since they are no longer coefficients of 'nodal' degrees of freedom, the 'assembly' is simply a straight forward summation. The same procedure follows when summing up modal contributions from every element to give the 'global' modal matrices and tensors.

The advantage in using modal transformations is evident right here. All the way from the sub-matrices level we are dealing with arrays whose maximum size is set by the number of modal coordinates used. This smaller system is going to be integrated forward in time. The variables of interest, including strains and stresses, can be written out at any instant of time desired.

Assembly of Load Vector

As described in section 4.1.3 of this chapter, the exception to the above transformation and assembly procedure, is the formation of the correlated load vector. In order to account for the space-time correlation, the global array assembled from all elements, F_i, is still in 'nodal coordinates', calculated for unit pressure per unit area. This vector is then prepared for each time-step using the method described. Then, a modal transformation is carried out at *every time-step*.

4.2.4 Step-Size Considerations

One of the important aspects of numerical simulations is the time-step size or sampling interval, Δt. It is required that Δt be small enough to capture the response up to the upper frequency cut-off, f_c. This cut-off frequency or *Nyquist frequency* is the "highest frequency that can be reproduced from data sampled at equal intervals

Δt" [140]. Therefore, in order to avoid *aliasing* (where two disparate frequencies become indistinguishable), a sampling interval of

$$\Delta t \leq \frac{1}{2f_c} \tag{4.2.1}$$

must be used.

A good estimate of the f_c value to be used can be obtained from the natural frequencies of the plate. It is generally known that the major response of a vibrating system falls within about its first six modes of vibration (six symmetric modes in case of a symmetric system). If the sixth natural frequency is known, then an f_c value greater than this can be used. The sampling interval can be determined accordingly. The load spectrum also is set to span all these frequencies.

A greater constraint on the step-size for numerical integration is its *stability*. Although there are no guarantees for a nonlinear system, an adequately small value has to be used. This usually results in a sampling interval smaller than that needed to accommodate the Nyquist frequency. A point to mention in this context refers to some work on stability of nonlinear systems. There are some proofs for stability of nonlinear structural dynamics based on the principle of energy conservation [141,142].

One more note regarding the step-size refers to the membrane plate responses. The inplane degrees of freedom for a thin plate are typically active at very high frequencies. A Δt value that captures such high frequencies (at modes that couple in case of a nonlinear problem) will have to be extremely small. This results in a computationally enormous task. Since the response at this range is negligibly small, it is not critical if the vibrations at these frequencies are ignored. All we really need, again for a nonlinear problem, is the effect of membrane coupling on the lower bending modes. Hence, the step-size required is computed based on the significant bending modes only.

A change of variable brought about by implementation considerations is the replacement of $\alpha_n^{(3)}$ by d_n in the expressions for acceleration, velocity and displacement at any time-step, see Eqs.(3.1.4). Here,

$$d_n = \alpha_n^{(3)} \frac{\Delta t^3}{6}$$

As mentioned earlier, $\alpha_n^{(3)}$ is usually very large and Δt^3 is very small. This change of variable avoids the possibility of errors induced by computations involving such large number of significant digits in both these quantities.

4.3 Postprocessing

The large number of samples that form the time-history data sets for each output variable in the solution need to be processed to extract meaningful information regarding plate response characteristics. Each of the parameters used will be discussed below.

The **power spectrum estimate, P(f)**, is based on the description in [139]. For a data set, $c_j(t)$, of N samples, the FFT using a 'Parzen window' function, is

$$C_k = \sum_{j=0}^{N-1} c_j \, w_j \, e^{2\pi i j k/N} \quad , \qquad k = 0, \ldots, N-1 \tag{4.3.1}$$

where

$$w_j = 1 - \left| \frac{j - \frac{1}{2}(N-1)}{\frac{1}{2}(N+1)} \right| \tag{4.3.2}$$

is the window function. The power spectrum estimate, therefore, is

$$P(f_k) = \frac{1}{W} \left(|C_k|^2 + |C_{N-k}|^2 \right) , \qquad k = 1, 2, \ldots, (\frac{N}{2} - 1) \tag{4.3.3}$$

where

$$W = N \sum_{j=0}^{N} w_j^2 \tag{4.3.4}$$

Frequencies f_k are defined only for zero and positive frequencies as

$$f_k = \frac{k}{N\Delta t}, \qquad k = 0, 1, \ldots, \frac{N}{2} \tag{4.3.5}$$

The power spectrum is finally obtained by averaging together K estimates at M frequency values between 0 and f_c. The number of segments in the data set, K is defined as N/4M. It is desired that N and M be in powers of 2.

The statistical properties are next computed. The parameters used are the mean, μ, standard deviation, σ (root mean square when the mean is close to zero), skewness, s, and kurtosis, k [139]. The mean for a data set, $c_j(t)$, of length N, is given by

$$\mu = \frac{1}{N}\sum_{j=1}^{N} c_j \tag{4.3.6}$$

Similarly, the moments are as follows

$$\sigma = \left[\frac{1}{N}\sum_{j=1}^{N}(c_j - \mu)^2\right]^{1/2} \tag{4.3.7}$$

$$s = \frac{1}{N}\sum_{j=1}^{N}\left[\frac{c_j - \mu}{\sigma}\right]^3 \tag{4.3.8}$$

and

$$k = \frac{1}{N}\sum_{j=1}^{N}\left[\frac{c_j - \mu}{\sigma}\right]^4 - 3.0 \tag{4.3.9}$$

The kurtosis moment ratio is usually 3 for an ideal gaussian process. Thus for a normal distribution the value of kurtosis is zero. A negative kurtosis implies a wide distribution shaped like a loaf of bread and a positive value relates to a sharply peaked distribution. A broad sense of the degree of nonlinearity in the response data can be obtained by observing how far this value is from zero.

The mean is for the most part close to zero, although it may be significant in the cases where thermal and acoustic loading are combined. The value of σ from the above equation is checked against the root mean square value obtained from the power spectrum estimate. They should be close.

The **peak probability distributions** for the responses will be presented in a few cases. The probability densities of all the *positive peaks* in the response time-histories are computed. A peak is treated as a value of magnitude greater than its preceding and succeeding values. This may not be an accurate measure of the peak probability, say, when snap-through motion occurs. The number of sample points per 'cycle' in the time-history must not be too sparse.

Apart from these, a few figures showing the probability distribution functions, PDF, are presented. The PDF shows the density of distribution of random samples about their mean. Again, this is a graphical check of the skewness - the deviation from the classic 'bell' shaped distribution - in case of nonlinear responses. A plot of the load PDF will be displayed for reference.

Chapter 5

RESULTS AND DISCUSSION

Numerical results are presented for numerous cases to illustrate the problem analysis and formulation discussed in earlier chapters. The random load model to be used is first described. The accuracy of the present formulation is verified by comparisons against existing solutions. Mesh and modal convergence studies are first presented for an unsymmetric cross-ply laminate. Most of the numerical examples that follow are for a symmetric laminate. The modal analysis for this laminate is detailed before random response results are presented. A modal convergence study under random load is carried out for this baseline laminate. Variation of responses under increasing load levels is tabulated. Temperature distributions considered include a simple uniform temperature assumption and a complete generalized non-constant distribution. Responses under uniform normal loading, as well as grazing-wave loading are then compared. Additional data to display the effects of other parameters, such as, plate thickness, initial stress, etc, are presented.

5.1 Random Load

The random pressure time-history generated has a frequency response function as given by Eq.(4.1.2). In this study, the sampling interval is set at $\Delta t = 10^{-4} s$ and, thus, $f_c = 5000\, hz$. The Nyquist frequency, f_c, easily includes the lower natural frequencies. Furthermore, the sampling interval, or the time-step size, is small enough to maintain low amplitude decay and period elongation. The number of

time-steps or samples obtained is set to $N = 2^{15} = 32768$. The pressure spectrum has a bandwidth up to f_u which is chosen to be $4900\,hz$, and $f_l = 1/N\Delta t = 0.30517\,hz$, is the lower cut-off frequency. The value of f_u was set at 4900hz to cover the whole range of responses possible. A single filter was found to be sufficient. The spectrum of the resulting pressure time-history at 130db sound pressure level (SPL) is given in Fig.4. Its probability density histogram is shown in Fig.5.

5.2 Verification of Formulation

The finite element formulation presented in this study is first evaluated for accuracy using previously published results. The various intermediate stages in developing the program, were checked using simple free vibration and static nonlinear bending results. Linear forced vibration solutions (deterministic) were compared against solutions obtained from exact formulas. This helped verify the numerical integration algorithm. The final verification step is the only one detailed here, involving linear and nonlinear random vibration responses.

5.2.1 Normal Random Load at $\Delta T = 0$

Comparisons of results from the present formulation are made against those from Ref.[89] and Ref.[105]. Mei and Prasad, in Ref.[89], compute, using an analytical Galerkin single-mode approach and the equivalent linearization technique, random response solutions for square simply-supported symmetric cross-ply laminates of various length-to-thickness (a/h) ratios. Results with and without transverse shear effects have been listed. The classical formulation of the governing equations uses the Airy stress function, thereby neglecting membrane inertia terms. All comparisons made here are for transverse shear deformable behavior. The material properties for the graphite-epoxy laminate used here are as follows

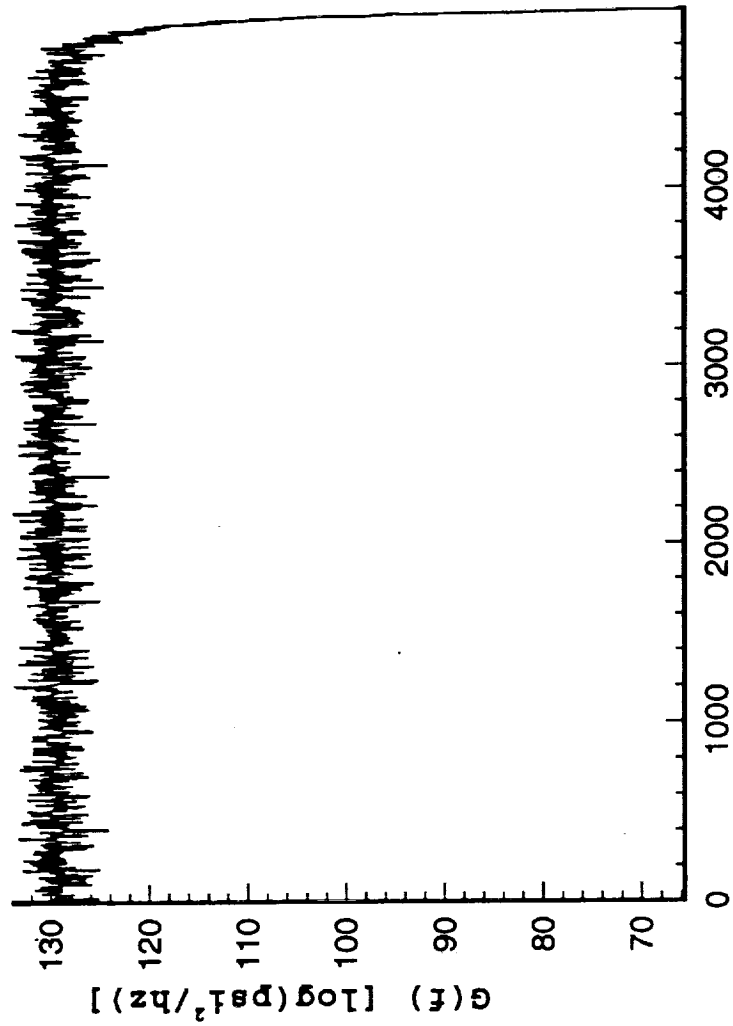

Fig.4 Acoustic Pressure Power Spectrum

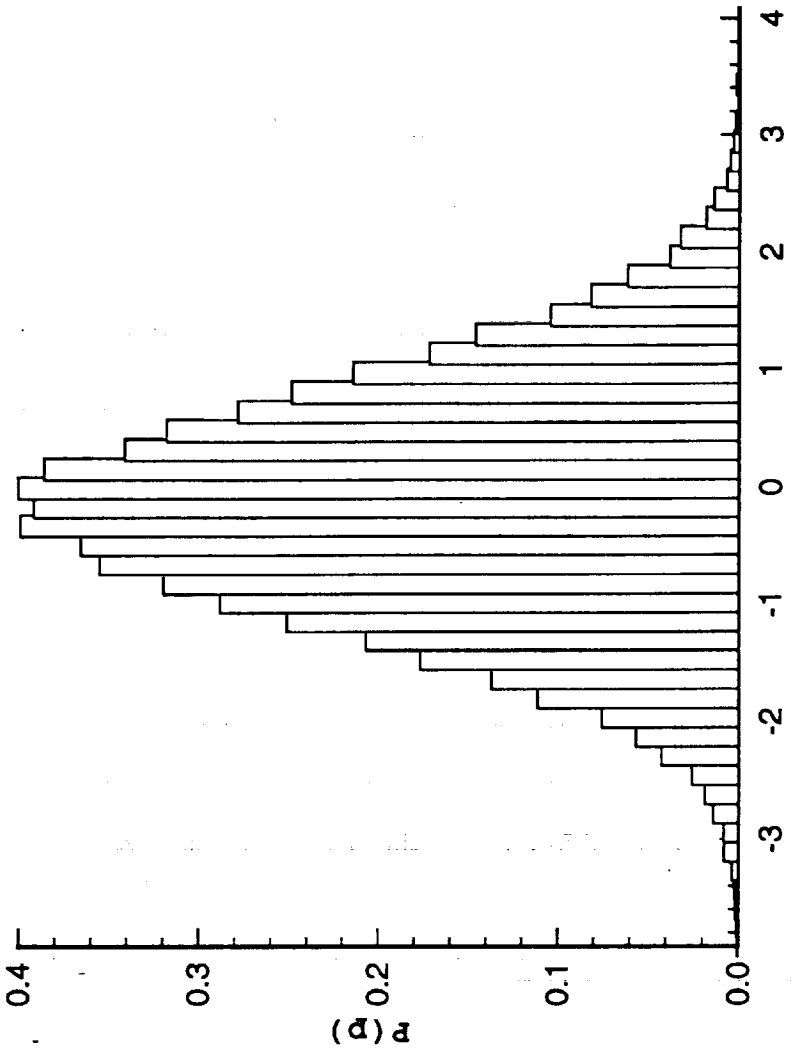

Fig.5 PDF of Acoustic Pressure

$E_2 = 0.75 \times 10^6\, psi$

$E_1/E_2 = 40$

$G_{23}/E_2 = 0.5$

$G_{12}/E_2 = G_{13}/E_2 = 0.6$

$\nu_{12} = 0.25$

$\rho = 2.4 \times 10^{-4}\, lb - s^2/in.^4$

$a = 12in.,\quad a/h = 200$

damping ratio, $\zeta = 1\%$, with modal damping, $c_i = 2\zeta\omega_i$.

A shear correction factor of $\mathcal{K} = 1$ is used, to coincide with the unit 'tracing constant' used in Ref.[89]. The boundary conditions used are for a plate simply-supported on all sides, with immovable inplane boundary conditions as shown in Fig.6. Since the plate is symmetric, consisting of cross-ply layers only, a 4×4 quarter-plate model is used. The analysis leading to the mesh size used here is detailed in section 5.3.1. The fundamental frequency obtained is at 69.992 hz, which exactly matches the frequency corresponding to the nondimensionalized parameter $\bar{\omega}_o = 18.88$ given in Ref.[89].

The nonlinear simulation to be done requires the use of membrane mode-shapes. Of the lowest few membrane modes, the first mode was found to be inactive, i.e., its presence made no difference to the deflection rms values. Therefore, the next 3 membrane modes are used. As seen in results below, sufficient agreement in the deflection results is obtained with these three membrane modes. Thus, simulation is performed with a total number of modes $R = 4$, with 1 bending mode and 3 membrane modes.

Numerical values are compared at 130db SPL, for $\bar{\sigma}$, a nondimensional root-mean-square (rms) deflection parameter for the maximum deflection at the center of the plate, given by

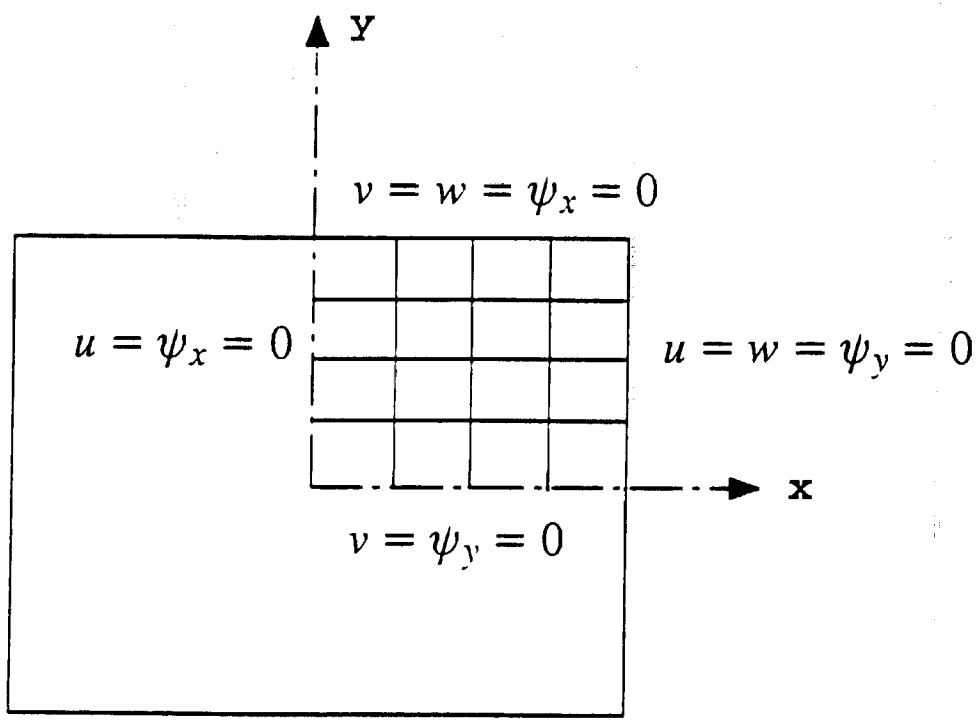

Fig.6 Simply-Supported Quarter-plate Boundary Conditions

$$\bar{\sigma} = \frac{10\,\sigma E_2 h^3}{a^4\sqrt{PSD\,f_1}}$$

where σ is used to represent the standard deviation for maximum deflection, (same as rms since the mean is negligible), f_1 denotes the fundamental frequency, and PSD stands for the magnitude of the power spectral density (psi^2/hz) for 130db SPL (see [89]). Using a reference pressure level value

$$p_{ref} = 2 \times 10^{-5}\,Pa = 2.9 \times 10^{-9}\,psi$$

we have,

$$PSD = p_{ref}^2\, 10^{SPL/10} = 8.425 \times 10^{-5}\,psi^2/hz$$

The results for linear and nonlinear responses are given in Table 1. A graphical representation of responses at various load levels is shown in Fig.7. As shown in the table, the difference from Ref.[89] is within 4%.

	linear		nonlinear	
	Ref.[89]	present	Ref.[89]	present
σ (in.)	0.3955	0.3800	0.0955	0.0917
$\bar{\sigma}$	0.4024	0.3860	0.0972	0.0933
σ/h	6.592	6.333	1.592	1.53
Difference	-	3.8%	-	3.7%

Table 1. Cross-Ply Laminate Rms Deflection

There seems to be very good agreement between the results in both Table 1 as well as Fig.7. Some of the factors in the computation procedure that differ between the two methods need to be highlighted. The Lagrangian quadratic element used in this study, is known to converge to the exact deflection from below (frequency from above). The numerical integration algorithm as well as the Newton-Raphson

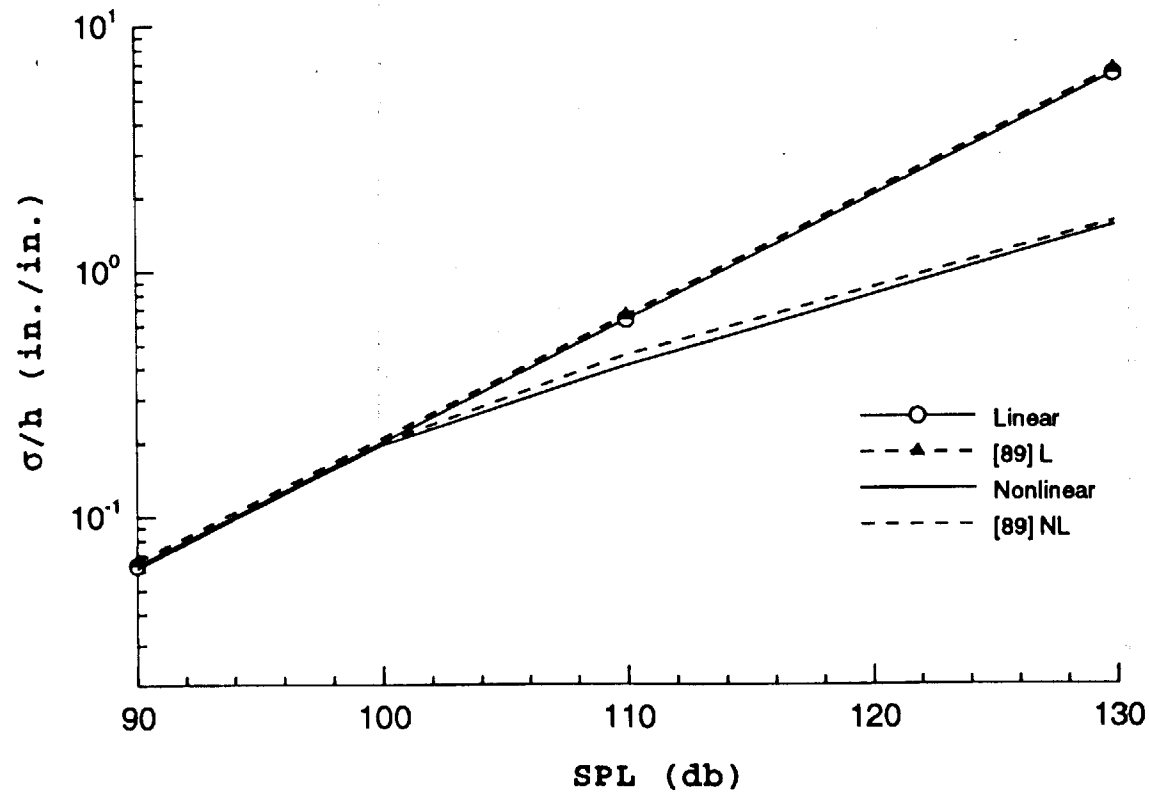

Fig.7 Rms w_{max} vs SPL, Cross-ply Laminate

iteration technique are known to produce conservative results. However, this influence is rather small for a system with moderate nonlinearity (note that $\sigma/h \approx 1.6$). These are, however, factors that could predict lower values than a classical equivalent linearization method. A point to mention is the level of membrane contribution for this case. The ratio of membrane modal rms values to the fundamental mode rms value were in the order of 10^{-3}.

At this stage, the numerical simulation formulation has been verified for nonlinear deflection responses. This confirms the accuracy of the formulation in the absence of thermal loads. A numerical comparison of strain data is presented next.

A verification for the strain values was made against data from Ref.[105]. In Locke's study, a thermally buckled isotropic plate under a symmetric acoustic load is analyzed using a post-buckling formulation in conjunction with the equivalent linearization method. The membrane stiffnesses were eliminated by static reduction. A quarter-plate finite element model with 36 24-degree-of-freedom rectangular elements was used. The results for simply-supported boundary conditions with immovable edges, as in Fig.6, are used here. The properties of the plate are (with a shear correction factor included for the present formulation)

$$
\begin{aligned}
E &= 10.5 \times 10^6\, psi \\
\nu &= 0.3 \\
\rho &= 2.588 \times 10^{-3}\, lb - s^2/in.^4 \\
a \times b \times h &= 15 \times 12 \times 0.04 \quad (in.) \\
\zeta &= 1\% \\
\mathcal{K} &= \pi^2/12 \\
f_1 &= 44.078\, hz
\end{aligned}
$$

Single-mode finite element results were compared with classical solutions by Locke in Ref.[105]. Verification here is for a plate with no thermal load. The

finite element model used here again has a quarter-plate 4×4 mesh. The numerical simulation used the lowest few membrane modes, of which the first mode is relatively weak; its influence on the deflection results being negligible. The next 2 membrane modes were used along with one bending mode. i.e.,

$R = 3$; 1 bending mode and 2 membrane modes.

The single-mode nonlinear random responses at 95db and 125db SPLs are compared below in Table 2. The maximum strain is in the y-direction and its rms value is denoted by ϵ_{rms}, given in micro-strain units, $10^{-6}\, in./in.$ The rms and standard deviation for strain are not identical, since the mean is no longer small.

	95db		125db	
	σ/h	ϵ_{rms} $(\mu\epsilon)$	σ/h	ϵ_{rms} $(\mu\epsilon)$
Classical [105]	0.391	22.41	2.771	362.95
FEM [105]	0.390	22.58	2.766	366.49
present	0.380	21.42	2.6925	301.82
Difference	2.77%	4.4%	2.8%	16.8%

Table 2. Rms Deflections and Strains for Isotropic Plate

The difference above has been computed against the equivalent linearization classical solutions given in the first row of the table. The rms deflection values agree very well and so does the strain at 95db. The difference in strain values at the higher load has possible cause in a few factors. The differences in the membrane formulations between the two methods is a possible factor, since membrane action is stronger at high load levels. The interpolation functions and the finite element mesh used also influence the displacement derivatives. The displacement and rotation interpolations in this study are C^o continuous, resulting in their derivatives being

discontinuous across element boundaries. In Ref.[105], the bending displacement function has C^1 continuity. The strain computations are, therefore, likely to be more accurate. The inplane displacement functions used are C^o continuous. But the same interpolations are again used to calculate the strains and curvatures, making these continuous. The figures posted here for strains are actually the maximum *elemental strain values*, at the centroid of the element and not at a particular node. In effect, an average over an element is being compared with the maximum occurring at one of its nodes.

5.2.2 Normal Random Load with Constant ΔT

The verification for this case is done against the thermal post-buckling solutions of Ref.[105]. Equivalent linearization results for single-mode rms deflection and strain responses are generated at multiples of the critical buckling temperatures. The present simulation results are compared against these, at the critical buckling temperature, ΔT_{cr}.

The lowest non-zero eigenvalue of the buckling eigenvalue problem corresponds to ΔT_{cr}, scaled by the ΔT value used to build up the thermal stiffness matrix, $K_{\Delta T}$ (see Eq.4.2.6). The value of ΔT_{cr}, using the same material properties and boundary conditions listed in section 5.2.1, was found to be $\Delta T_{cr} = 0.9^o F$. Again, a single bending mode is used with two membrane modes in the simulation. Using a uniform temperature distribution at $\Delta T = \Delta T_{cr}$ and a 95db acoustic load, the rms values obtained are listed in Table 3 below. Comparisons were made at a lower decibel load, since the effect of thermal loading is more pronounced than at higher levels.

There seems to be reasonably good agreement given the differences between the two methods of formulation discussed earlier. A major difference between the two formulations that affect combined loading results, is in the post-buckling solution

used by Ref.[105] for both the classical and finite element methods. The static deflection shape obtained from the thermal loading problem is used as an initial deflection in the random vibration problem. The membrane action is accounted for by this static mode, making the model stiffer than a multiple-mode-assumption. In the case of the simulation, the thermal and acoustic loading occur simultaneously, which amounts to the thermal load also being treated as part of a dynamic problem. This is an important difference as it results in higher buckling eigenvalues being involved in the response. Their effect will be studied later.

	σ/h	$\epsilon_{rms}\ (\mu\epsilon)$
Classical Ref.[105]	0.497	29.22
FEM Ref.[105]	0.496	29.42
Present	0.4965	26.0
difference	0.1%	11%

Table 3. Rms Deflections and Strains for Combined Load

5.3 Numerical Examples

The following sections present responses for various acoustic and thermal load cases for a specified baseline plate model. A mesh and modal convergence analysis is first performed on an unsymmetric laminate. The baseline plate used is a symmetric laminate. Results are presented for response under varying decibel levels. Further simulation for various temperature distributions, the grazing incidence acoustic load, etc., is performed at a baseline load level of 130db SPL.

5.3.1 Mesh Convergence

Different mesh sizes are tested to represent a full-plate model of an unsymmetric laminate. The changes in the natural frequencies, nonlinear random deflections and strains are observed. An unsymmetric laminate is used, since separate membrane modes are not necessary when $B_{ij} \neq 0$ (see section 4.2.2). The unsymmetric laminate used is a two-layer cross-ply graphite-epoxy panel of a (0/90) lay-up. The plate is assumed fully clamped on all edges with immovable inplane displacements, i.e.,

$$u = v = w = \psi_x = \psi_y = 0, \quad \text{on all 4 edges}$$

The material properties for the laminate are

$$E_1 = 22.5 \times 10^6\, psi$$
$$E_2 = 1.17 \times 10^6\, psi$$
$$G_{23} = 0.66 \times 10^6\, psi$$
$$G_{12} = G_{13} = 0.4 \times 10^6\, psi$$
$$\nu_{12} = 0.22$$
$$\rho = 1.458 \times 10^{-4}\, lb - s^2/in.^4$$
$$a \times b = 15 \times 12\,(in.)$$
$$h = 2 \times 0.024\,(in.) = 0.048\,(in.)$$
$$\zeta = 2\%, \quad c_i = 2\zeta\omega_i$$
$$\mathcal{K} = \pi^2/12$$

Free-vibration eigenvalues and eigenvectors are obtained for three different mesh sizes. The mesh sizes used are a 6×6, 8×8 and 10×10 grid of rectangular 45-degree-of-freedom elements over the full plate. The number of mode-shapes required to obtain converged nonlinear rms maximum deflection and rms maximum strain values were determined using the 8×8 mesh model. The details of this modal convergence study will follow in section 5.3.2. A total of seven modes ($R = 7$) is

used for nonlinear random simulation at 130db SPL for all the three mesh models. The highest of these modes is mode (4,1). Table 4 below shows results for three parameters, namely, the frequency for mode (4,1), the center deflection, σ, and the maximum strain (y-axis), ϵ_{rms}. The strain values are, as mentioned before, given at the element *centroid*. They represent an averaged value over the area of the element. With a changing mesh, the location of the element where strain is maximum changes. Results from the 10×10 mesh are used as a basis for comparison of results from the smaller meshes. This mesh was selected as a reference mesh, based on linear random response convergence studies by Robinson [143].

mesh size	mode (4,1)	σ	ϵ_{rms}
6×6	4.4%	3.8%	14.3%
8×8	0.7%	-0.8%	-10.2%

Table 4. Mesh Convergence for (0/90) Plate

The minus signs above indicate that the values were lower than the 10×10 mesh values. As can be seen, mesh convergence for the nonlinear quantities, deflection and strain, is not monotonic. Robinson [143] shows monotonic mesh convergence in linear random deflection response. Locke [144] conducted mesh convergence studies for thermal post-buckling nonlinear deflections and stresses for a clamped isotropic plate. All these converged monotonically. The added change in the present case is the modal transformation combined with nonlinear random simulation. Therefore, the possible factor in the present convergence behavior is the modal cross-correlation in the transformed equations of motion.

The 6×6 mesh shows a fair amount of difference even in the natural frequency results. Therefore, this mesh will not accurately model the required mode-shapes.

The 8×8 mesh shows excellent comparison with regard to both the frequency and the nonlinear deflection. This indicates that there is adequate resolution in the modelling of the required mode-shapes. The strain value shows poorer convergence behavior, but the difference is still in the 10% range. Amongst the various stresses due to thermal loading studied by Locke [144], the membrane stress at the edge midpoint showed the poorest convergence behavior. Given adequate resolution in modal representation, the strain values can be expected to vary with element sizes, as they represent averages over progressively smaller areas.

Th 10×10 mesh size, resulting in 1805 degrees-of-freedom, is a large problem for the eigenvector computation method that was used here. In this regard it is preferable to use the 8×8 mesh. The difference in strain data between the two is within a reasonable range. Hence, for the most part, the 8×8 mesh is chosen in the following examples.

5.3.2 Modal Analysis

The modal analysis leading to the random results in the above section is detailed here. The same analysis for the symmetric laminate to be used is also presented in this section. This symmetric laminate has no coupling between bending and membrane mode-shapes and, therefore, will involve modal convergence studies for both the membrane and bending mode-shapes.

Modal convergence for the unsymmetric (0/90) laminate is carried out using the 8×8 mesh on the full clamped plate. The lowest ten mode-shapes in ascending order of their natural frequencies, are as follows: (1,1), (2,1), (1,2), (2,2), (3,1), (3,2), (1,3), (2,3), (4,1), and (4,2). Their frequencies ranged from $75.5\,hz$ for the fundamental frequency to $421.6\,hz$ for the tenth natural frequency. Random response simulations are run at 130db SPL, with increasing number of modes included. The modal rms values are computed along with rms maximum deflection, at the center, and

maximum strain, along y-axis. The element corresponding to the maximum strain is, for this mesh and load, not at the long edge midpoint. It was found to be one element away from the edge. This can be expected, since the maximum strain for a clamped plate is 'close' to the edge. A refined mesh picks this maximum value at an element away from the edge. Further discussion on this follows under section 5.3.3.

Figure 8 shows the modal convergence curves for deflection and strain for this case. Of all the lower modes listed above, no response was detected at modes (1,2) and (2,2), the third and fourth modes, respectively. The modal time-histories at these two modes showed rms values below 10^{-12}. Further, including or excluding them did not affect the deflection and strain responses. The deflection as well as strain data show reasonable convergence within the first four active modes itself. A more confident estimate of converged values is with seven modes, as there is modal activity, albeit weak, at modes beyond these.

The converged rms maximum deflection and strain values for this case are $\sigma/h = 1.737$ and $\epsilon_{rms} = 377.3\,\mu\epsilon$.

Baseline Plate

The modal convergence studies for the baseline plate are discussed next. The properties of the plate are the same as those listed in section 5.3.1. Its symmetric lay-up consists of eight layers, each $0.006in.$ thick, in a $(0/+45/-45/90)_s$ configuration. All other parameters, including the total thickness, remain the same. The plate is assumed fully clamped. Two finite element meshes are generated for this plate, the 8×8 mesh and a smaller 8×4 mesh. This smaller mesh has been chosen with the grazing load model in mind. Since the pressure-wave is assumed uniform along the y-axis, the number of elements along this direction is reduced. In all the results to

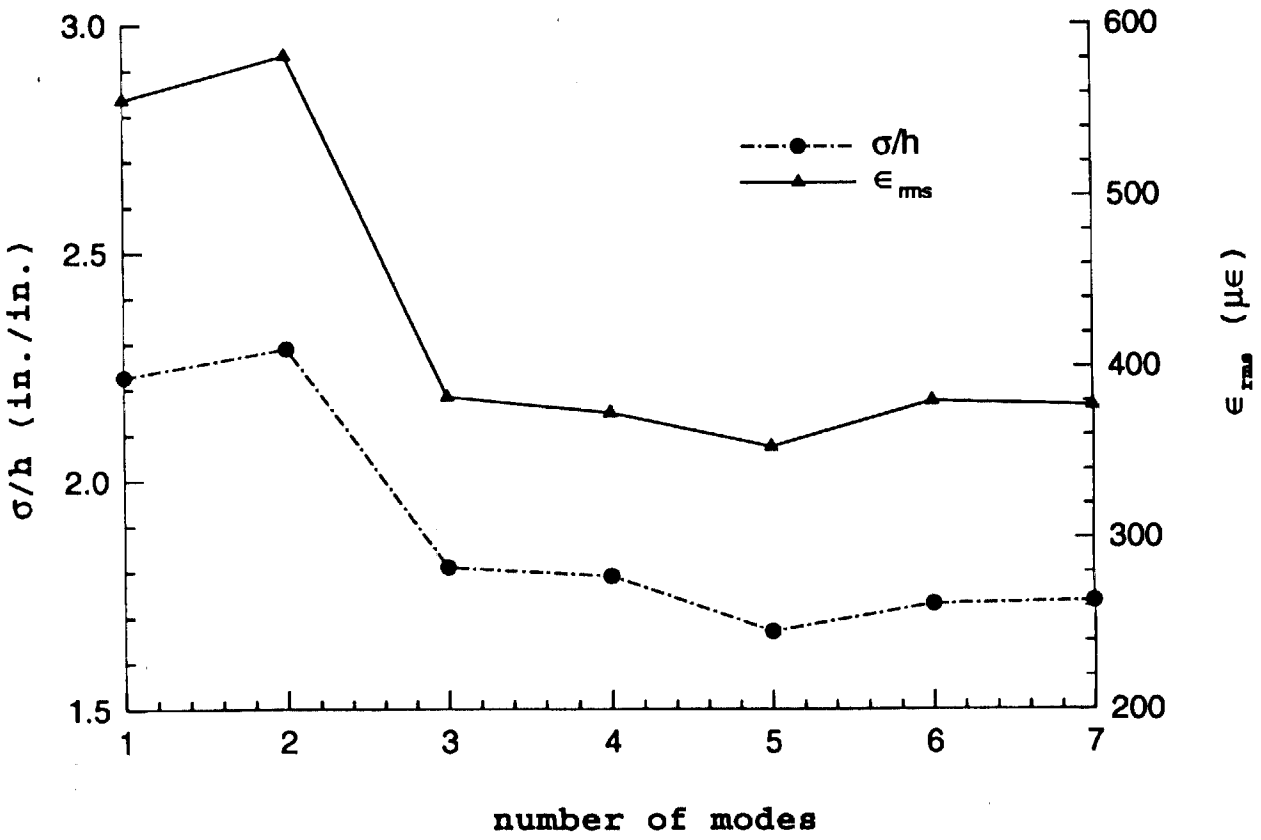

Fig.8 Modal Convergence for 0°/90° Clamped Plate

follow, the mesh and modal model used is specified for each case.

Free vibration eigenvalue problems were solved for both these meshes. An inspection of the bending modes indicated the presence of some 'skewness' in their shapes, despite the symmetric lay-up of the laminate. For instance, the fundamental (1,1) mode was found to be not perfectly symmetric. Neither are the anti-symmetric modes perfectly anti-symmetric. The (2,2) mode deviates from the classic single sine function curve as we approach the centerline of the plate. This can be observed in the figures for the first four modes plotted in Figs.9 and 10. An observation of the centerline for these mode-shapes [except mode (1,1)] shows the deviation from expected conventional shapes seen in isotropic or orthotropic laminates.

This type of skewness should be expected since the baseline laminate has angle-ply layers at $\pm 45^o$. These angle-ply layers result in non-zero values for D_{16}, D_{26} and their transpose positions (the twist-bending coupling terms) in the laminate bending stiffness matrix, D_{ij} (Eqs.2.3.9-11). Although the A_{16}, A_{26} positions of the extensional stiffness matrix are also non-zero, they are maximum for a three-layer angle-ply laminate and drop-off sharply as the number of layers increase. In keeping with this property, the A_{16}, A_{26} values were found to be negligible. A check of the membrane mode-shapes showed an absence of skewnesss, as there is no extension-twist coupling. The drop-off in the stiffness values with increasing number of layers is not so steep for the twist-bending coupling terms. They vary as L^2/L^3 for an L-layered laminate. The influence of this twist coupling on the skewness of the mode-shapes can be illustrated by redoing the eigenvalue analysis for the same laminate with D_{16}, D_{26} and its transposes set to zero. Fig.10 shows the (2,2) mode with and without twist coupling. The skewness has evidently vanished. Due to the presence of this skewness, all the lowest bending modes [(1,1), (1,2), (2,1), (2,2), (1,3), (3,1), ...] up until the twelfth natural frequency are saved for convergence

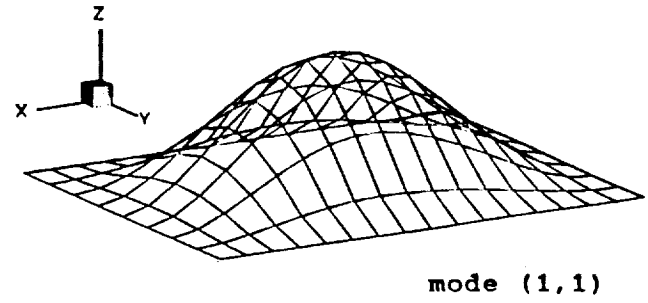

mode (1,1)

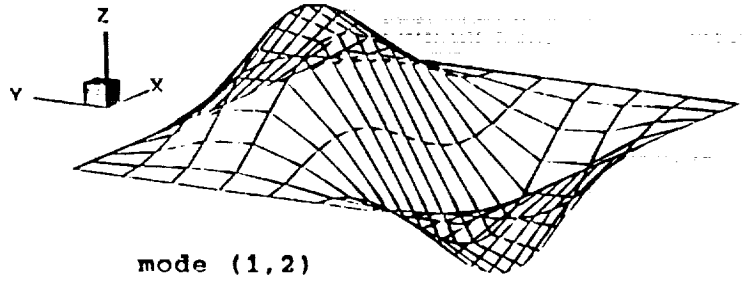

mode (1,2)

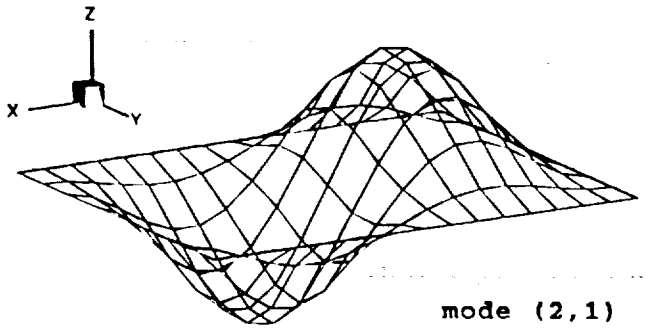

mode (2,1)

Fig.9 First Three Modes for Baseline Plate

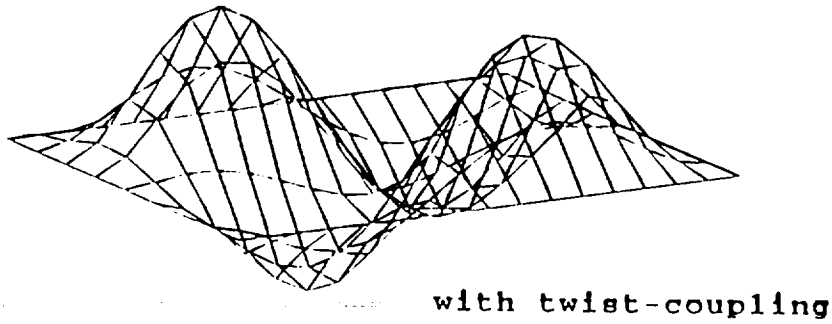

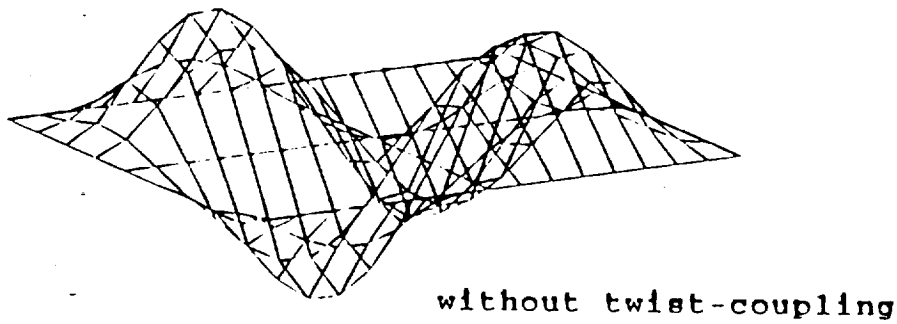

Fig.10 Mode (2,2) With and Without Twist-Coupling

studies. As the mode-shapes get more complicated [(3,3), (2,4), etc.], it is difficult to accurately label them so. Strictly speaking, it is rather erroneous to assign, say the mode (3,3), as done here, since the skewness seriously distorts its shape over the plate. The membrane mode-shapes are combinations of similar shapes for the x and y-direction displacements, u and v, respectively. For example, the lowest mode to be used here has shape (1,2) in x-direction and (2,1) in the y-direction. Convergence of nonlinear random deflection and strain responses are now done. In the interest of accuracy, all data presented are for the 8×8 elements mesh. Bending as well as membrane modes need to be picked. The modal convergence for number of membrane modes required is done using one bending mode, namely the first mode (1,1). A total of twelve membrane mode-shapes were saved ranging in frequency from $10207hz$ to $22336hz$. (It must be clarified here that, it is not the response solutions at these frequencies that are of interest, but the effect of these modes on the bending mode responses. This effect is represented in the modal equations through the nonlinear bending-membrane coupling tensor, $k1_{prs}$ (Eqs.2.5.13). Furthermore, the level of modal response at these frequencies is far smaller than those at the bending mode frequencies. This is why the excitation spectrum is not extended up to these high frequencies.) The highest mode amongst these has shapes (2,3) and (1,2) in the u and v displacements, respectively. Of these twelve membrane modes, six were found to be inactive, i.e., their modal rms values were zero and the deflection and strain results remained unaffected by their exclusion. Convergence results are with increasing number of *active* modes included.

Values for rms maximum deflection per unit thickness (σ/h), and maximum strain (ϵ_{rms}), at 130db SPL for increasing number of membrane modes are plotted in Fig.11. The maximum strain was found to be along the y-direction. The strain values are specified in micro-strain units. With the 8×8 mesh chosen, the element showing maximum y-axis strain at this load level is not at the long-edge mid-point,

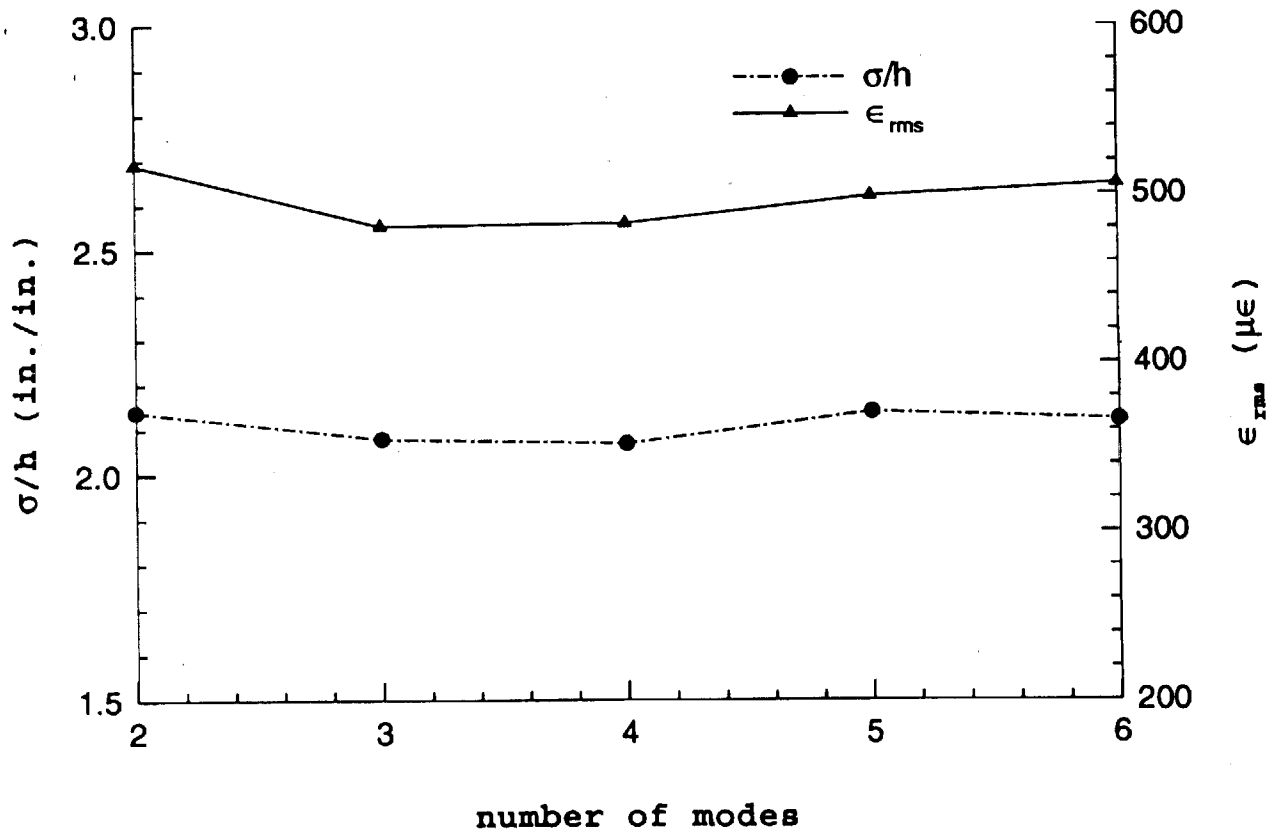

Fig.11 Membrane Mode Convergence for Baseline Plate

but at the next element towards the plate center, one row away from the edge. The sixth mode in the figure, where solutions have converged, in fact corresponds to the twelfth membrane natural frequency.

Bending mode convergence is studied next using linear and nonlinear simulations at 130db SPL. Nonlinear simulations use six membrane modes from the convergence shown above. Results for linear and nonlinear center deflection and y-axis strain are presented in Fig.12. As in the case of membrane modes, not all the lowest bending modes are active. The mode-shapes that were found to be active correspond to (1,1), (2,2), (1,3), (3,1), (3,3) and (2,4). Their natural frequencies are 102.3, 300.12, 338.45, 417.4, 594.0 and 652.9hz, respectively. In the case of the linear simulation, as seen in the figure, even single-mode solutions are fairly close to converged four-mode results. The convergence in the nonlinear simulation is not monotonic for both the deflection and strain curves. This is due to the presence of coupling between modes. This does indicate that the practice of neglecting cross-correlation terms in the modal equations, as done in most earlier analytical work, may lead to erroneous inferences on plate responses.

The converged rms values for σ/h and ϵ_{rms} are 6.4 and 628.0 $\mu\epsilon$, respectively in the linear case, and 1.86 and 438.5 $\mu\epsilon$, respectively for the nonlinear simulation.

Thus, the nonlinear solutions for the baseline plate at 130db SPL can be said to have converged with six membrane and six bending modes ($R = 12$). The various cases analyzed in the succeeding sections, use this set of modes for the 8×8 mesh. Since the center deflection value shows better convergence characteristics both in mesh size and number of modes than strain, the smaller 8×4 mesh with fewer modes has been used where only deflection data are presented. This smaller baseline plate model uses just two membrane modes based on the membrane convergence in Fig.11 and four bending modes based on the bending convergence in Fig.12.

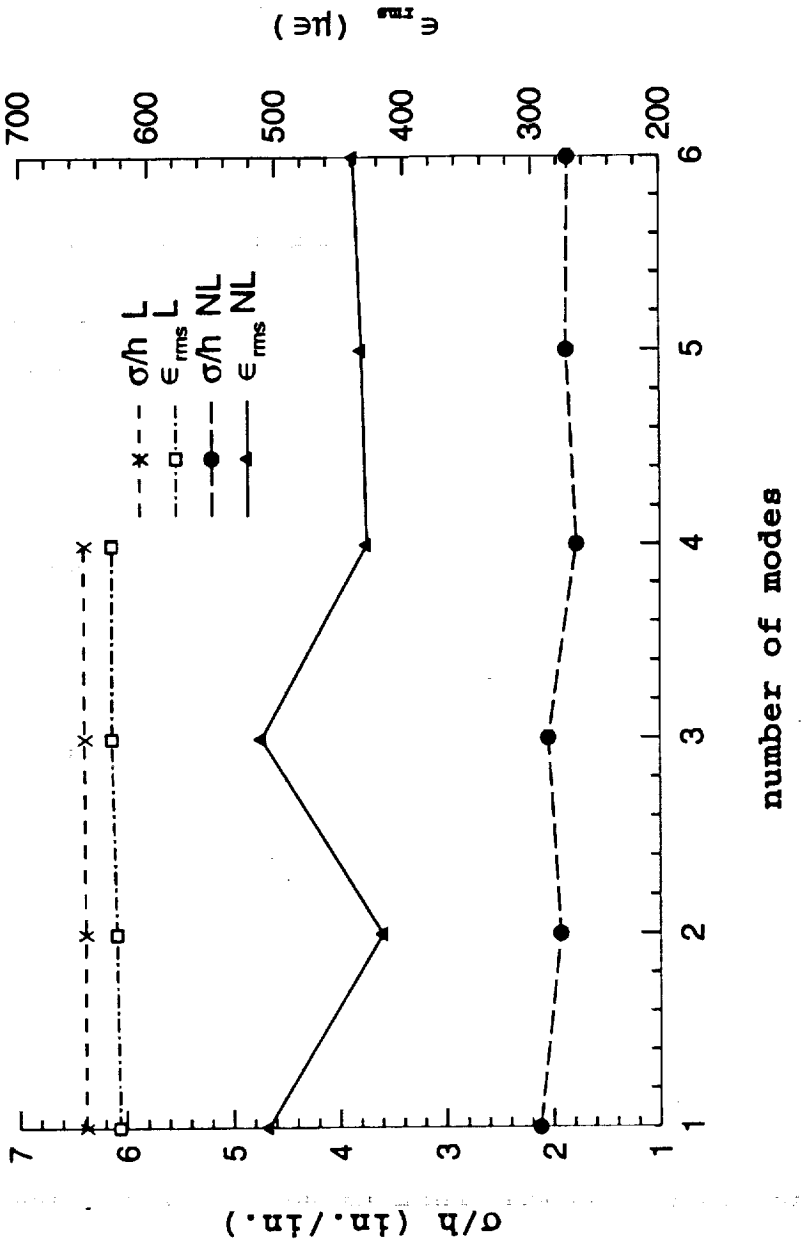

Fig.12 Bending Mode Convergence for Baseline Plate

C-2.

5.3.3 Load Variation

The next set of results displays the changing qualitative characteristics of panel responses under increasing sound pressure levels. The decibel levels used ranged from 90db SPL, where the deflections can be expected to remain within the linear regime of panel response, to 130db SPL, where as seen previously large deflections have set in ($\sigma/h \approx 2$). All the load levels had spectra similar to that in Fig.4. The pressure rms value obtained by integrating the frequency response function is simply scaled to suit the required SPL. The simulations were carried out with the 8×8 mesh plate model.

The variation of deflection response with SPL is shown in Fig.13. The hardening type nonlinearity is seen in the reduced nonlinear deflection values at higher loads. Data using the smaller baseline mesh defined earlier is also plotted in this figure. This gives a good estimate of the accuracy of a coarser mesh and fewer modes ($R = 6$), in predicting nonlinear deflection values. As can be seen the smaller mesh is fairly adequate as far as deflection values concerned. All other data in this section pertain to the 8×8 mesh model.

The effect of increasing load, and thereby, increasing nonlinearity, can also be seen in the power spectra for the center deflection shown in Fig.14. The spectrum for 90db SPL load shows distinct peaks corresponding to the (1,1), (3,1) (1,3) and (3,3) modes, respectively. The mode (2,2) which does show up in the modal rms values, here is a very small peak. The mode-shape in Fig.10 for this mode has a very small magnitude at the plate center. The spectra at loads 110db abd 130db show the hardening type nonlinearity, in the shift in their response peaks. There is significant broadening in these peaks, another indicator of nonlinear random response.

Table 5 shows the various statistics for rms maximum deflection at varying load levels. The standard deviation and rms coincide since mean deflection is zero.

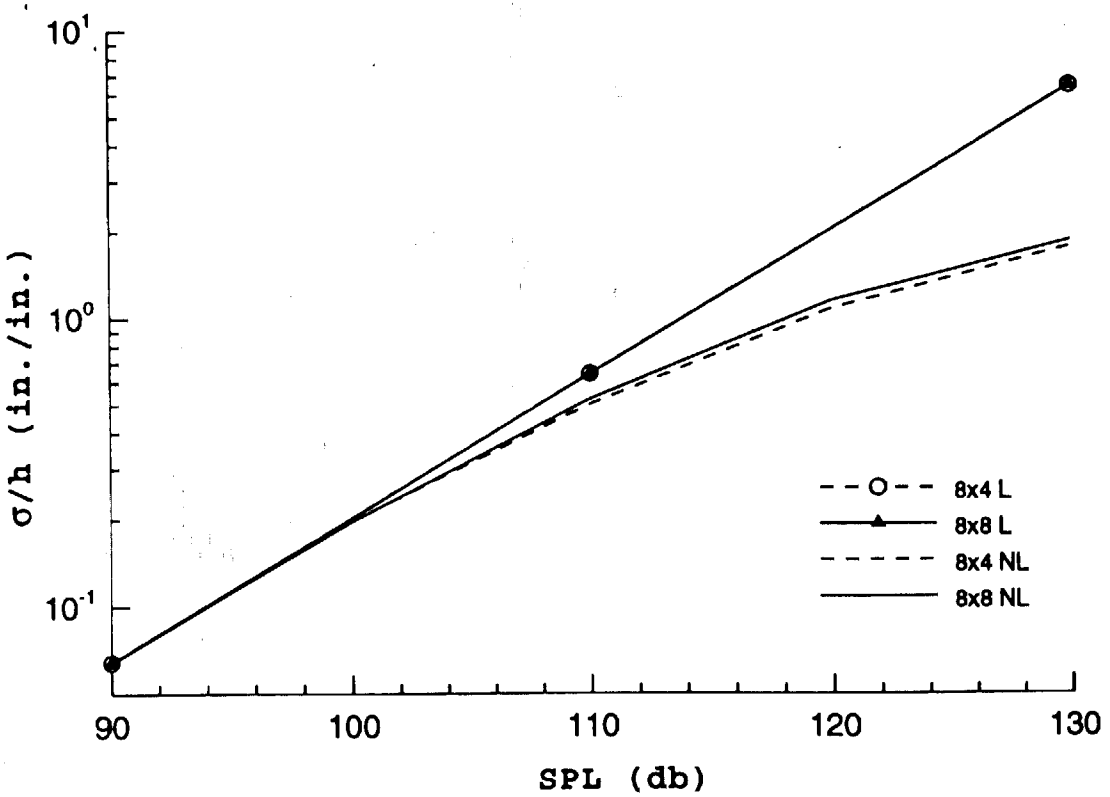

Fig.13 Rms Deflection vs SPL for Baseline Plate

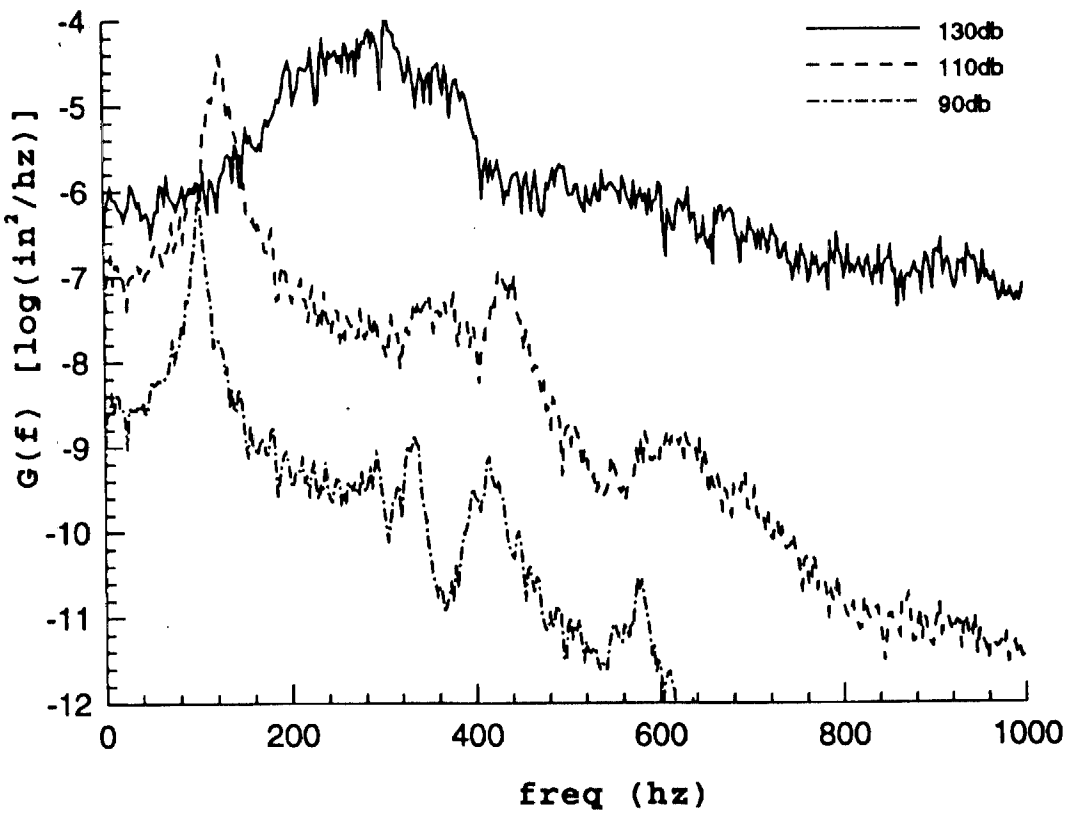

Fig.14 Power Spectrum for NL Deflection at Different SPL

The skewness and kurtosis, denoted by s and k, are non-dimensional quantities listed in columns 3 and 4.

SPL (db)	σ/h	s	k
90	0.0638	0.0558	0.614
100	0.1969	-0.004	0.32
110	0.524	-0.0026	-0.743
120	1.147	-0.008	-0.668
130	1.86	0.0152	-0.796

Table 5. Maximum Deflection Statistics vs Sound Pressure Level

For practical purposes the skewness values are very small and indicate a reasonably symmetric probability density distribution about the mean. Graphical illustrations of the probability density function (PDF) for the nonlinear deflection response at 90db and 130db load levels are displayed in Figs.15 and 16. The PDF of the linear response at 130db is shown in Fig.17 for comparison. As can be seen from these figures, the PDF is pretty symmetric about zero. A good indication of the increasingly high density of large magnitude responses is the trend in the kurtosis values. As mentioned in Chapter 4, a negative kurtosis indicates a 'bread-loaf' shape of the PDF and a positive kurtosis implies a narrower distribution peaking towards the center. The kurtosis numbers in Table 5 do reiterate the behavior seen in the figures. This nonlinearity as indicated by the kurtosis value at 130db is again reaffirmed in the peak probability density function for the large deflection response shown in Fig.18. Only positive peaks in the deflection time-history have been considered. A plot of the same for the linear deflection at 130db SPL is also shown in Fig.19. A comparison of the two shows a marked shift in the peaks towards higher

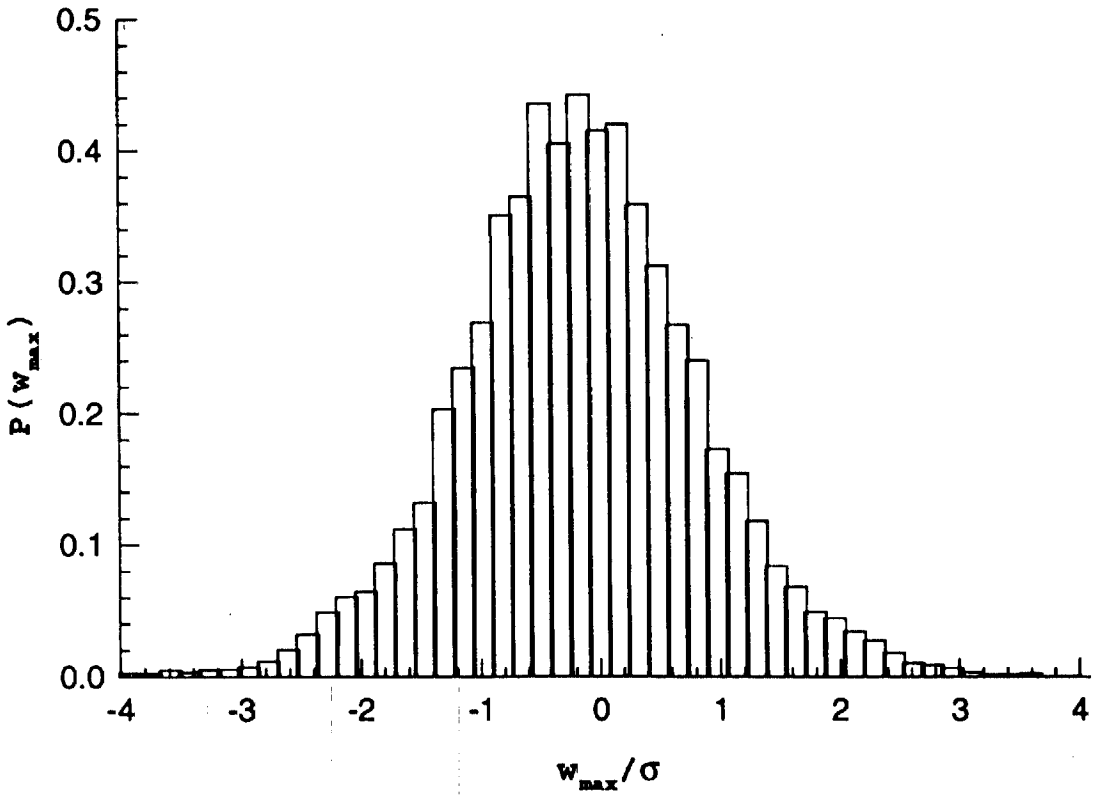

Fig.15 PDF of Nonlinear Deflection at 90db SPL

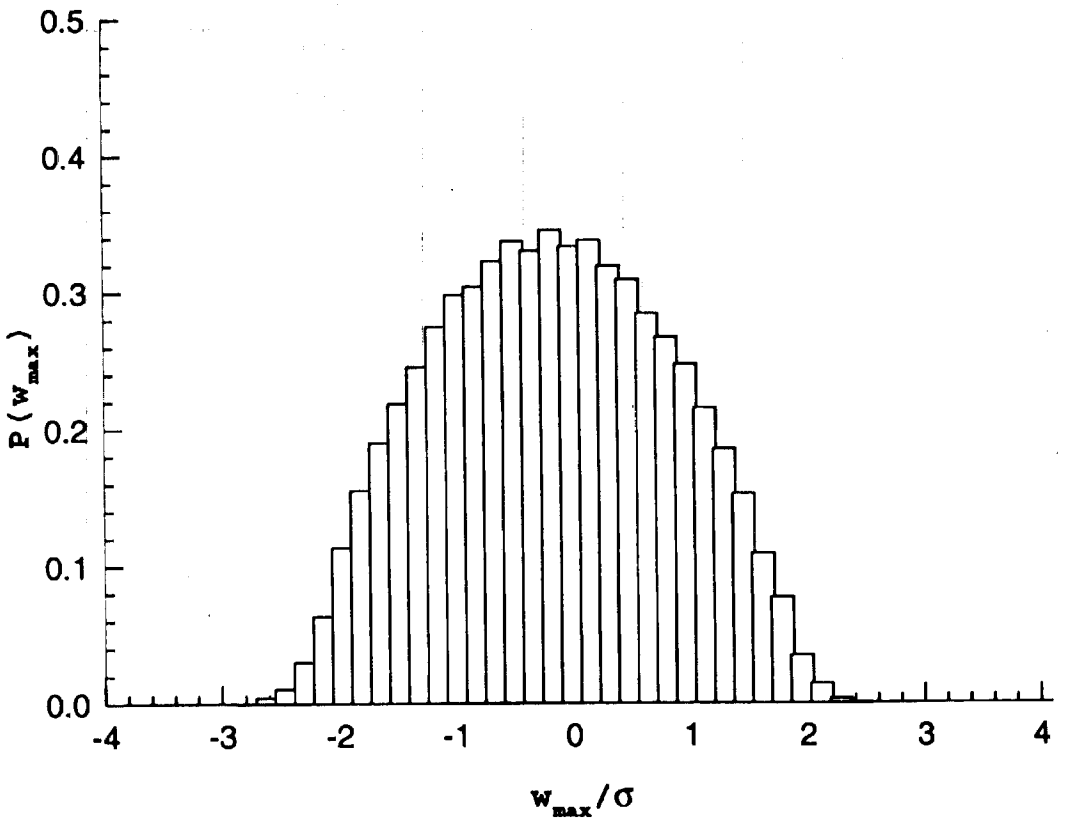

Fig.16 PDF of Nonlinear Deflection at 130db SPL

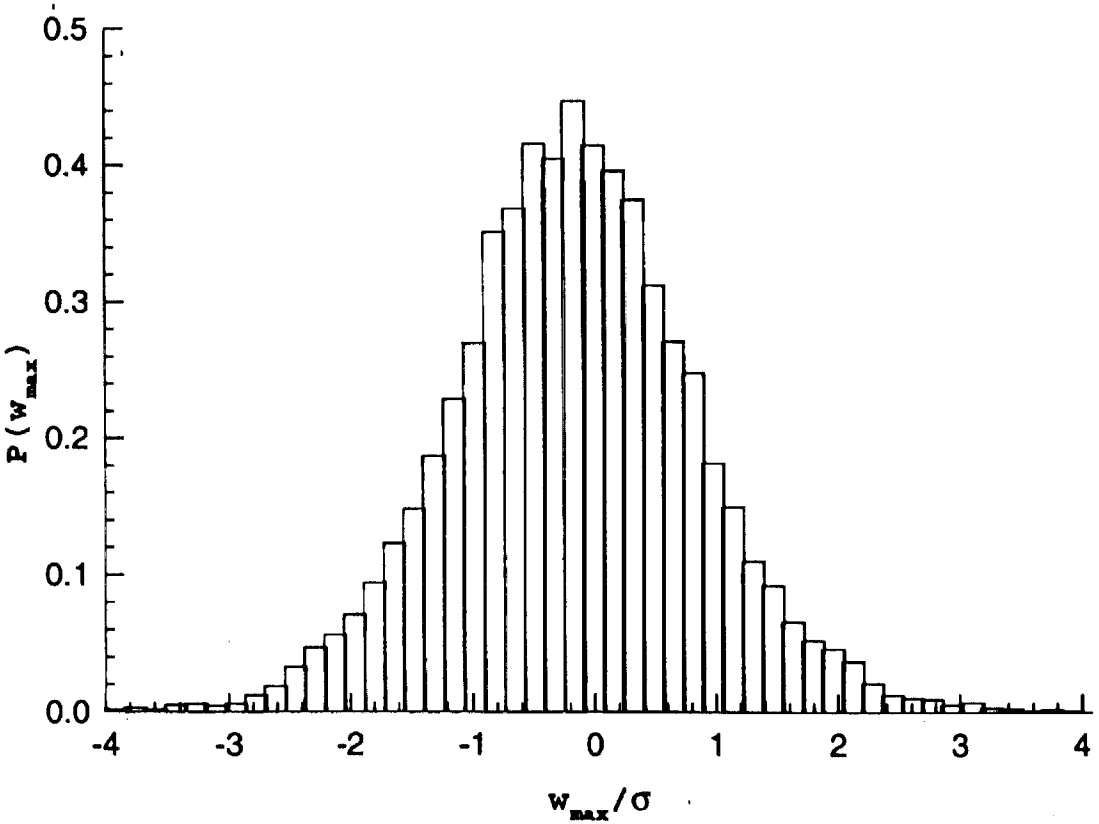

Fig.17 PDF of Linear Deflection at 130db SPL

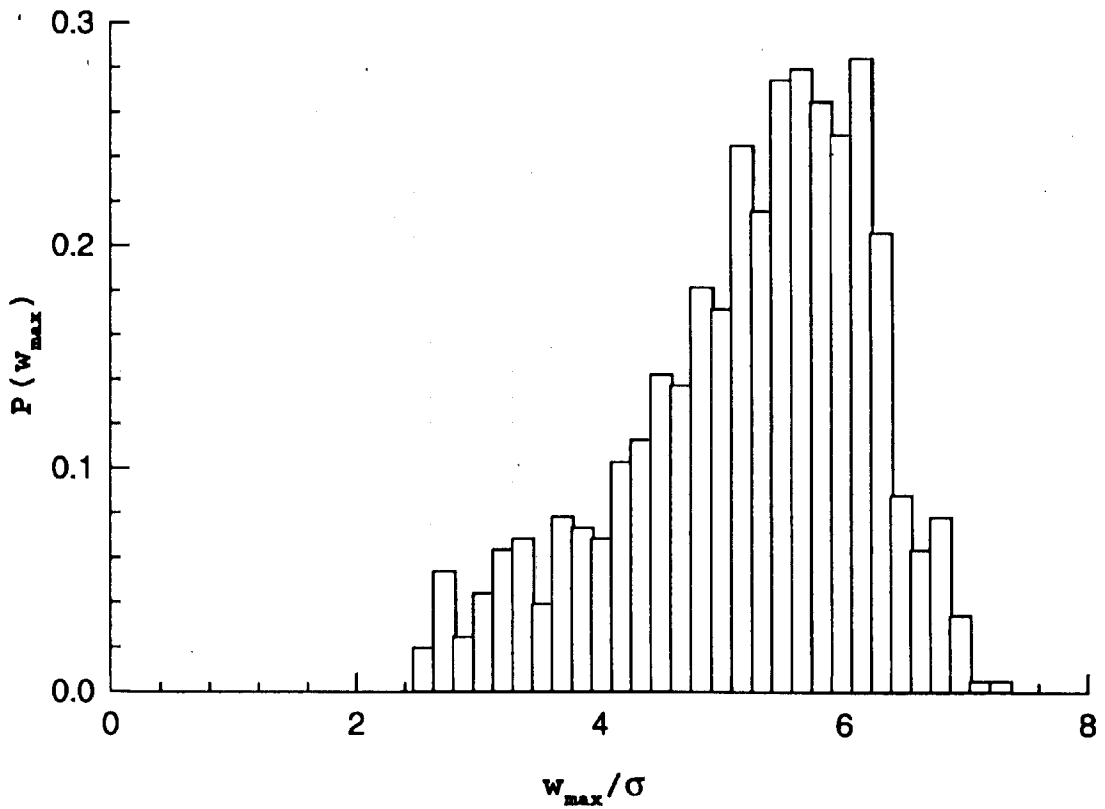

Fig.18 Peak PDF of Nonlinear Deflection at 130db SPL

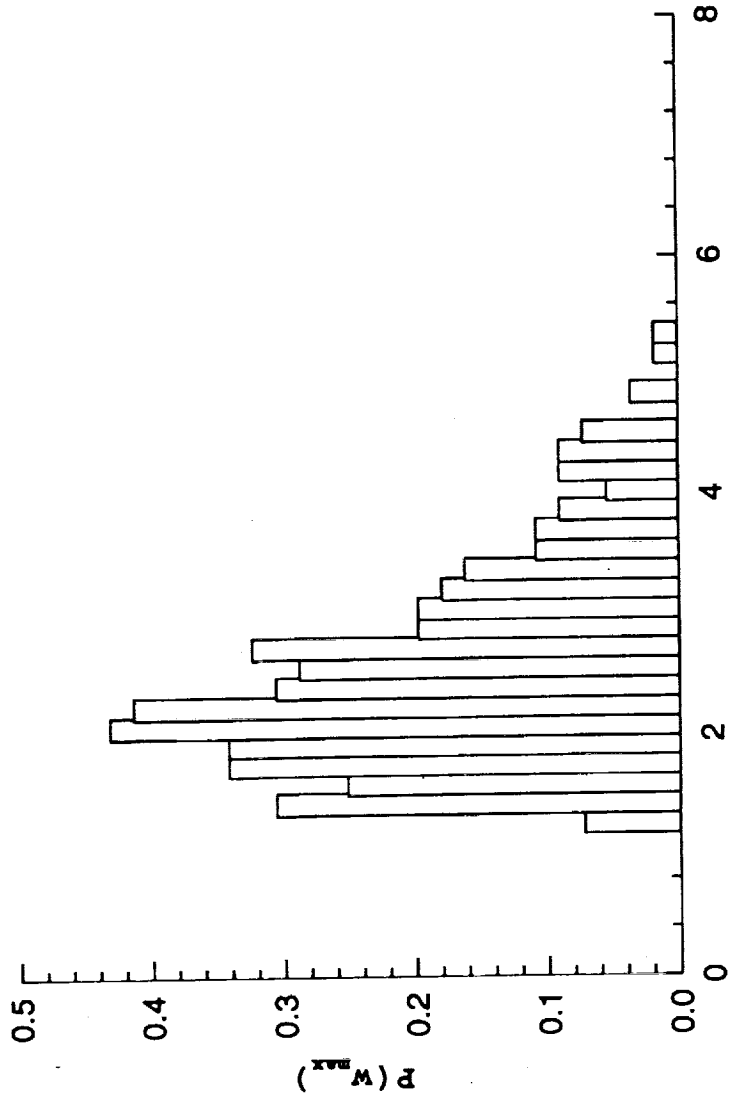

Fig.19 Peak PDF of Linear Deflection at 130db SPL

magnitudes in the nonlinear case. The Rayleigh distribution of the linear response peak density has also widened considerably.

The behavior of the normal strains in the plate with increasing load levels is next analyzed in a similar fashion. However, in this case, a breakdown of the various components in the maximum strain is presented. This clearly displays the changing quantities in the total strain with large deflection behavior setting in. The maximum strain was found to be in the y-direction (the shorter dimension), with x-direction strain reasonably well-behaved throughout. Therefore, the focus is on the maximum y-direction strain, ϵ_y. The maximum is computed at thickness, $z = h/2$. Unlike in the case of maximum deflection, which is at the center of the plate, the location of the maximum strain shifts with increasing load, for the 8×8 finite element mesh considered. The maximum strain is close to the mid-side of the long edge for all the load cases, since this is a clamped plate.

The power spectra at different loads for this strain are displayed in Fig.20. As in the case of deflection, the shift as well as widening in the response peaks is present here, too. The strain response at 130db SPL has almost reached a uniform broadband behavior, across the frequency spectrum. The power spectrum for strain at 90db generated using the smaller 8×4 mesh with a total of six modes, as mentioned before, has been included to draw attention to one important observation. A comparison of the 90db strain response spectra for this mesh with that for the 8×8 data shows a difference in the peak magnitudes. The higher magnitude for the second peak in the smaller mesh data indicates a greater contribution to strain at this mode. This indicates that this coarse mesh is too stiff to accurately predict strain contribution from this (1,3) mode.

Table 6 lists rms value of all the components of rms y-strain, ϵ_{rms}- ϵ^m, the linear membrane normal strain vector; ϵ^κ, the linear strain vector corresponding

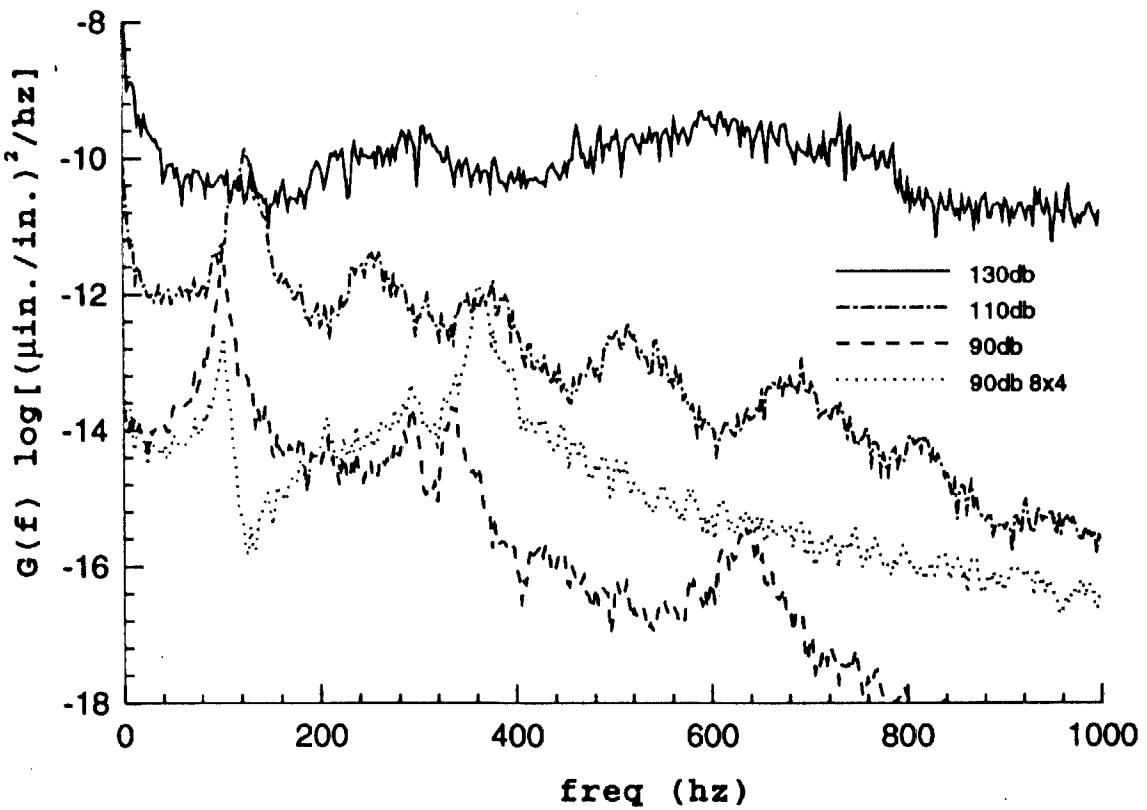

Fig.20 Power Spectrum of NL Y-strain at Different SPL

to curvature κ_i; and ϵ^w, the nonlinear strain vector due to large deflection (see Eqs. 2.2.6-10). The mean value of ϵ_y, denoted by ϵ_μ, is also included. All units are in micro-strains, $\mu\epsilon$. The skewness and kurtosis values are not presented for strain. They follow the trend in the deflection statistics but tend to be more extreme. All the statistics for the curvature component were found to be indicative of a zero-mean gaussian process at all loads.

At lower decibel levels, the dominant component in the total strain is the linear strain due to curvature, ϵ^κ. This is maximum at the edge. As the load level increases, the nonlinear strain component, ϵ^w, begins to gain magnitude. This component is highest a little away from the edge of the plate. This can be expected, since, right at the clamped edge, membrane extension is constrained. Therefore, at 120db and 130db levels, the element for which the strain reached a maximum has

SPL	ϵ_μ	ϵ_{rms}	ϵ^m_{rms}	ϵ^κ_{rms}	ϵ^w_{rms}
90	0.2285	6.248	0.035	6.245	0.4324
100	2.21	19.54	0.477	19.09	4.35
110	17.65	55.53	3.42	49.21	27.91
120	97.6	182.4	4.5	105.6	151.7
130	254.8	438.5	15.8	217.95	389.4

* *all in micro-strains*

Table 6. Rms Strain Components vs Sound Pressure Level

moved one row towards the interior of the plate.

The PDF distributions for this y-axis strain at 90db and 130db load levels are shown in Figs.21 and 22. The skewness in the strain at 130db is clearly noticeable. The peak PDF (positive peaks only) for 130db nonlinear strain response is given in Fig.23. Again, for comparison the linear peak PDF is displayed in Fig.24.

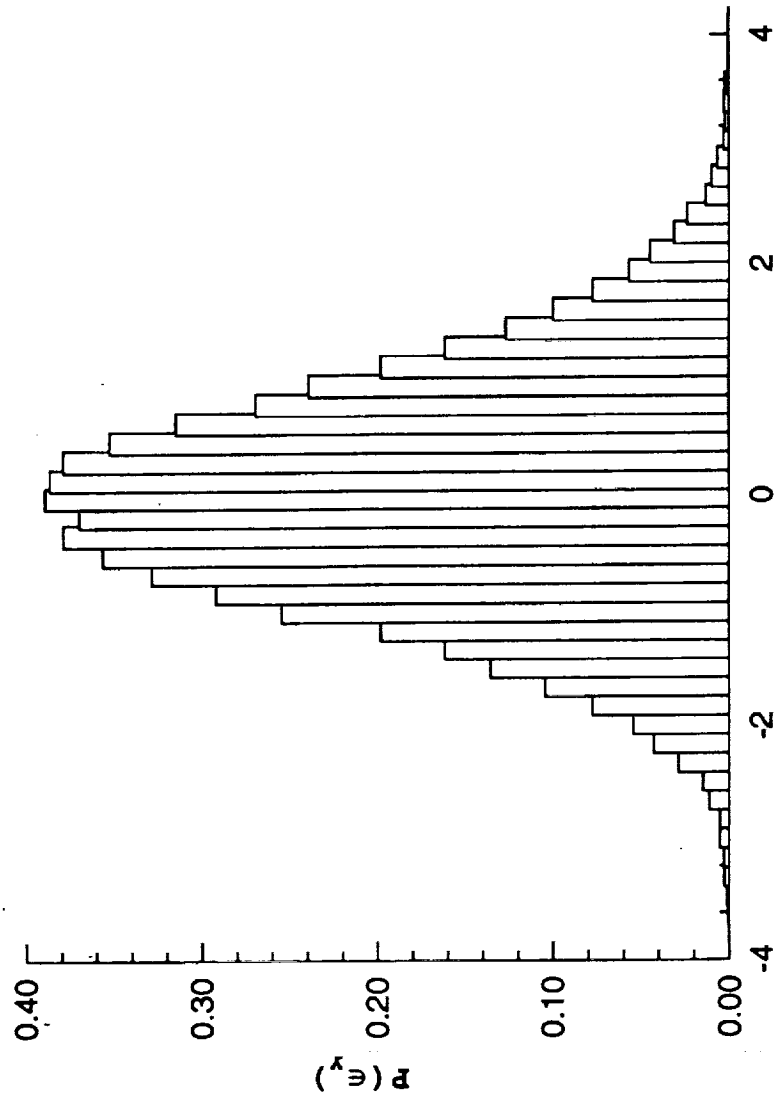

Fig.21 PDF of Nonlinear Y-strain at 90db SPL

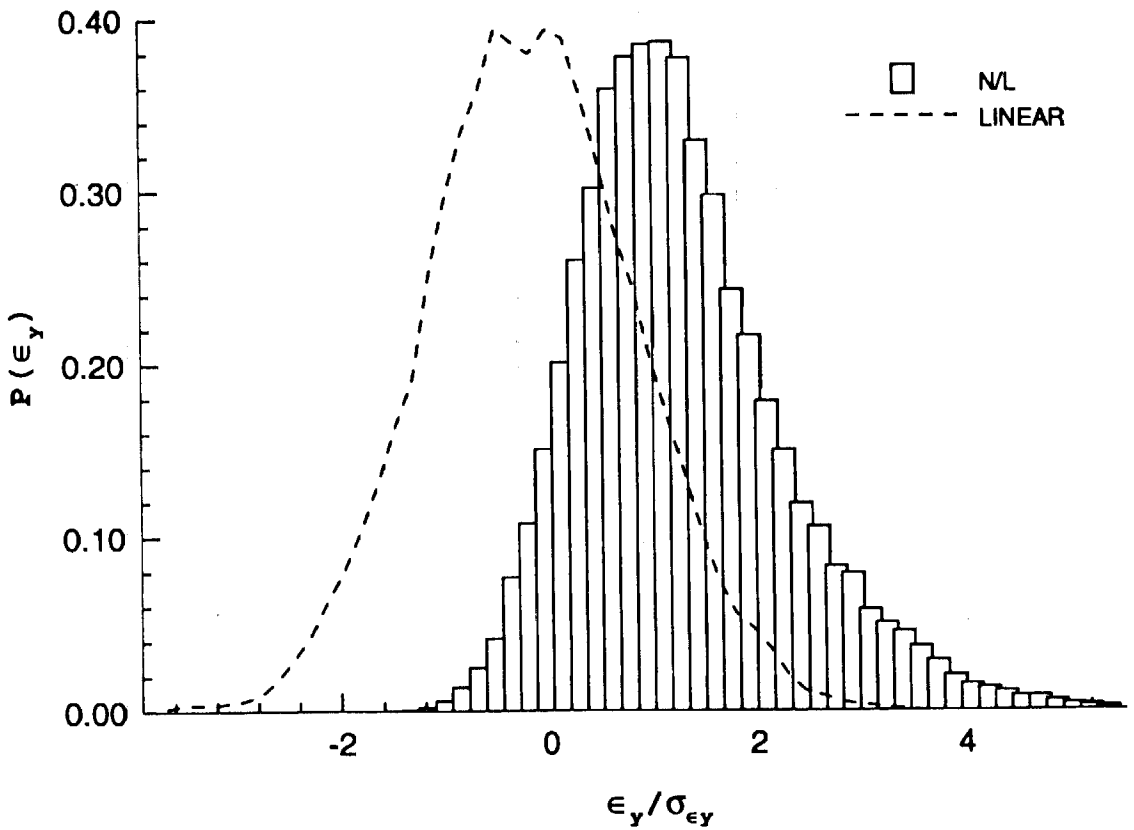

Fig.22 PDF of Linear and NL Y-strain at 130db SPL

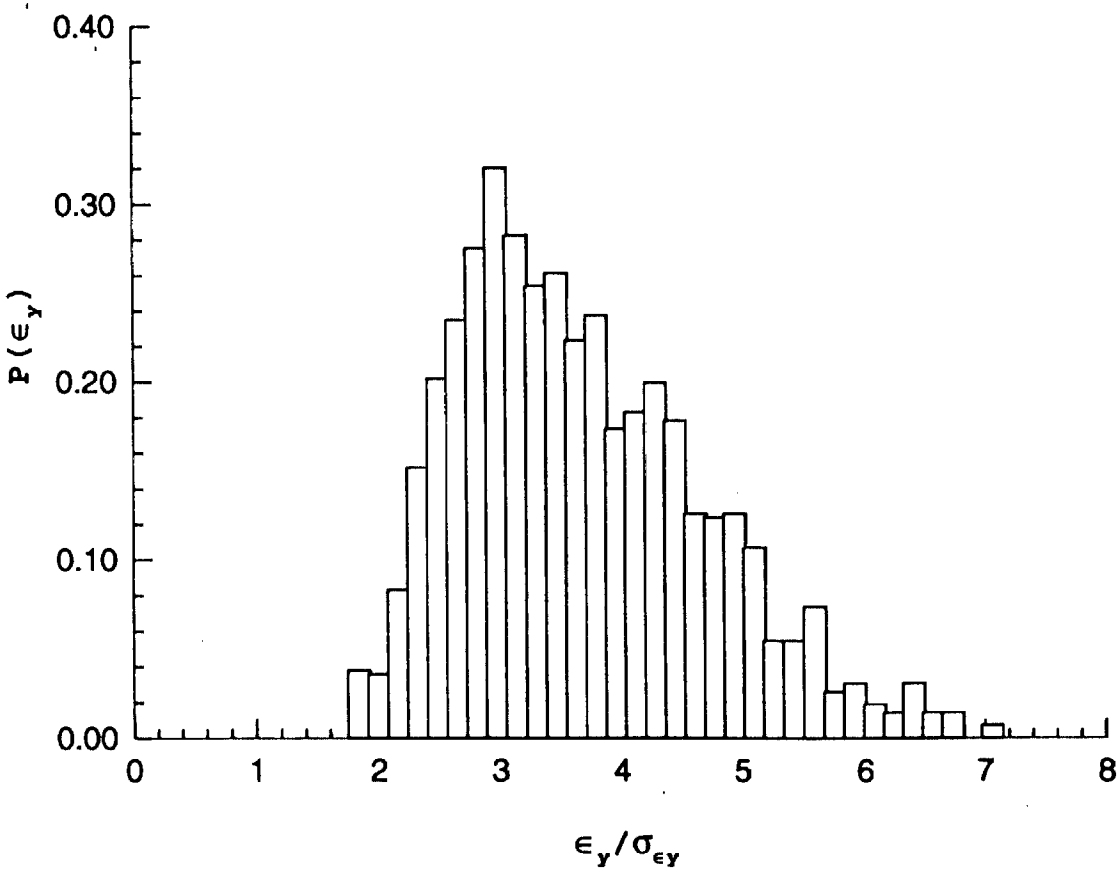

Fig.23 Peak PDF of Nonlinear Y-strain at 130db SPL

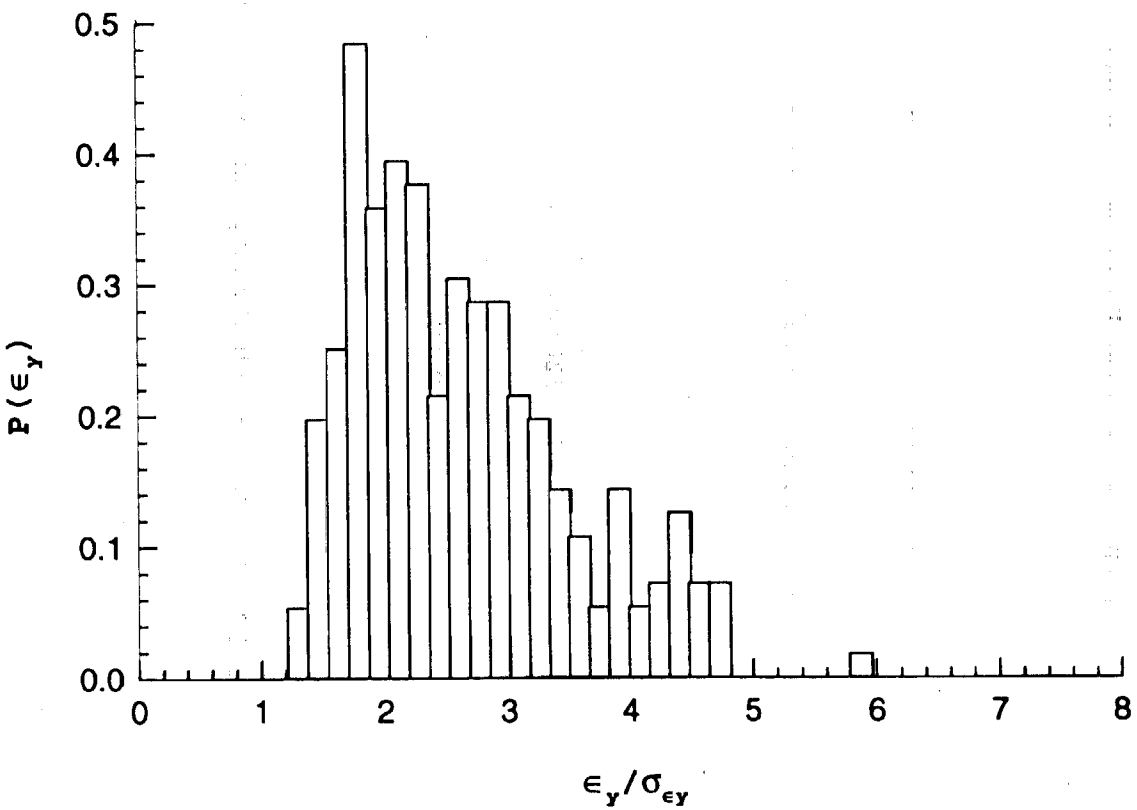

Fig.24 Peak PDF of Linear Y-strain at 130db SPL

As can be observed in the PDF figures, the increase in skewness is not accompanied by a strong deviation from a gaussian distribution. There is a slight move towards a Rayleigh distribution type shape in the nonlinear strain PDF. The wider distribution of strain in the nonlinear PDF is reflected in the peak density distribution of Fig.23. The broader range of peak magnitudes in the nonlinear peak PDF is concentrated in a smaller range in the linear response peak distribution of Fig.24. Further, there is a shift towards higher magnitudes in the nonlinear peak distribution. This shift is not as pronounced as in the case of deflection (Fig.18). The 'random' characteristics of nonlinear strain response are, for the most part still determined by its linearly-behaving curvature component. The nonlinear membrane action contributes to the strain primarily as a mean value increase.

5.3.4 Variation of Temperature

The changing responses under increasing temperature loads are now analyzed. The baseline plate is used with load at 130db SPL. The smaller 8×4 mesh is used here, since the results presented are for deflection behavior only. The total number of modes used to approximate the deflection is $R = 6$, as described before in section 5.3.2. The comparison in Fig.13 has shown that the center deflection rms values are reasonably accurate even with this model. The lowest few buckling temperatures were determined for this baseline plate configuration using Eq.4.2.6. The values obtained are

$$\Delta T_{cr_1} = 37^o\,F$$
$$\Delta T_{cr_2} = 49^o\,F$$
$$\Delta T_{cr_3} = 83^o\,F$$

Simulation results are generated at increasing levels of ΔT, ranging from 0^o to $80^o F$. A total of 15 different temperatures are considered, keeping in mind the buckling values above. These results combine both the dynamic random response as

well as the thermal response. The variation of rms deflection (σ) with temperature is shown in Fig.25. Strain results, although not presented here, did follow the same pattern of behavior. The peaks in the deflection response, denoted as ΔT_1, ΔT_2 and ΔT_3, approximately correspond to the above three buckling temperatures. When the same simulations were done with a single bending mode, the peaks more closely matched the buckling temperatures. These peaks are indicators of reduced modal (vibration modes) stiffnesses, at those temperatures. As the temperature passes the buckling value, the response increases and then decreases as the panel stiffness starts increasing again. These peaks are results for a system that includes the nonlinear stiffnesses, the inertia and damping terms. Therefore, it can be expected that the temperature values at which they occur do not exactly match the buckling eigenvalues given above.

This multiple peak characteristic of response under combined loading is not identified with a thermal post-buckling analysis. The buckled plate is modelled by the equivalent of its critical buckling temperature mode-shape. This eliminates the singularities that occur in the $[K - K^{\Delta T}]$ system at higher eigenvalues.

Snap-Through Motion

At temperatures much higher than those used above, snap-through motion in the large-amplitude deflection has been reported ([109], [125], [134]). A simulation at 130db SPL with temperature increased to $\Delta T = 350^o F$, did result in such a deflection response. The baseline plate model has six modes in an 8×4 mesh.

The time-history for maximum deflection, $w_{max}(t)$, at snap-through is displayed in Fig.26. A very short segment of about 0.1 *sec*, out of a sample of over 3 *sec*, has been extracted. The 'oil-canning' phenomenon, where vibration occurs about some non-zero amplitude for short bursts of time is clearly visible. The parallel segment for nonlinear time-history at $\Delta T = 0^o F$, is shown in Fig.27 for a

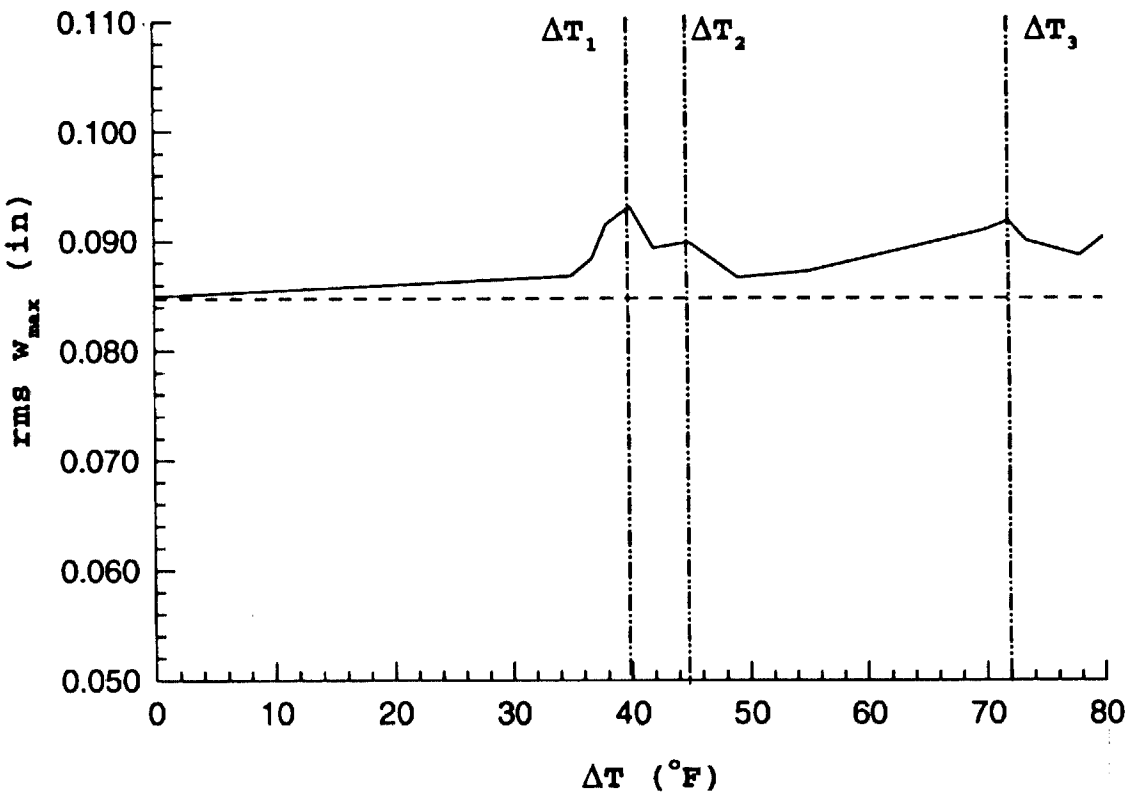

Fig.25 Nonlinear Deflection vs Uniform Temperature at 130db

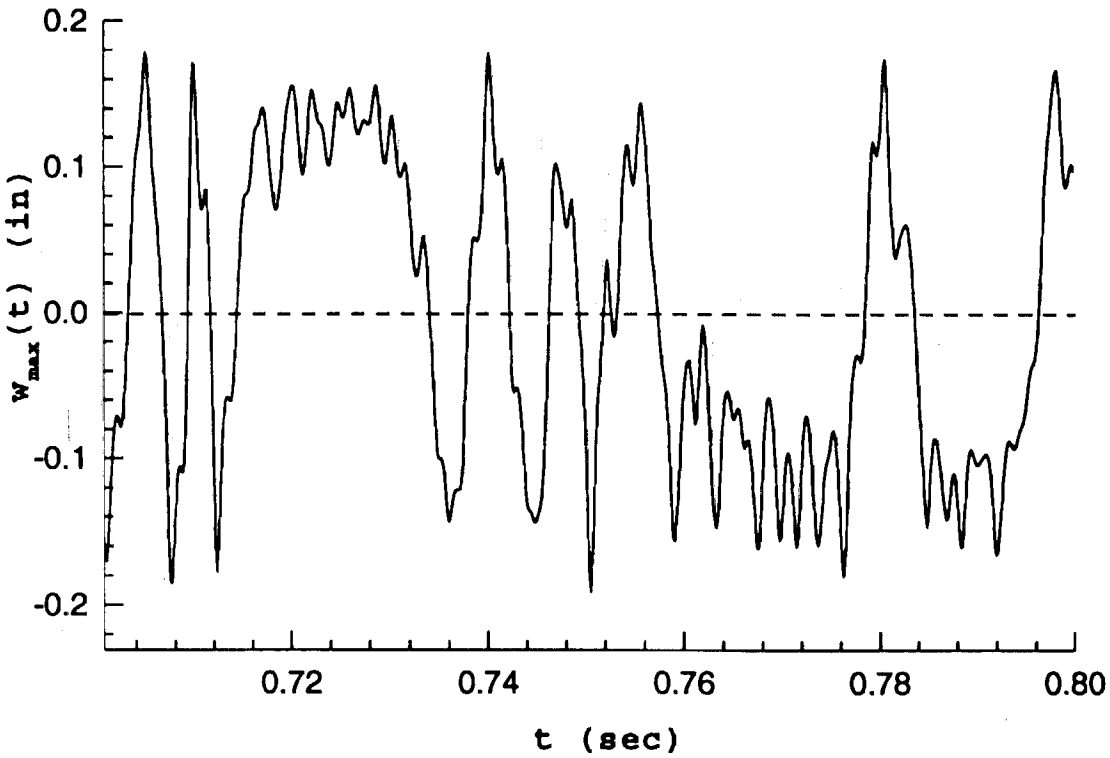

Fig.26 Snap-Through Motion in NL Deflection at 130db/350°F

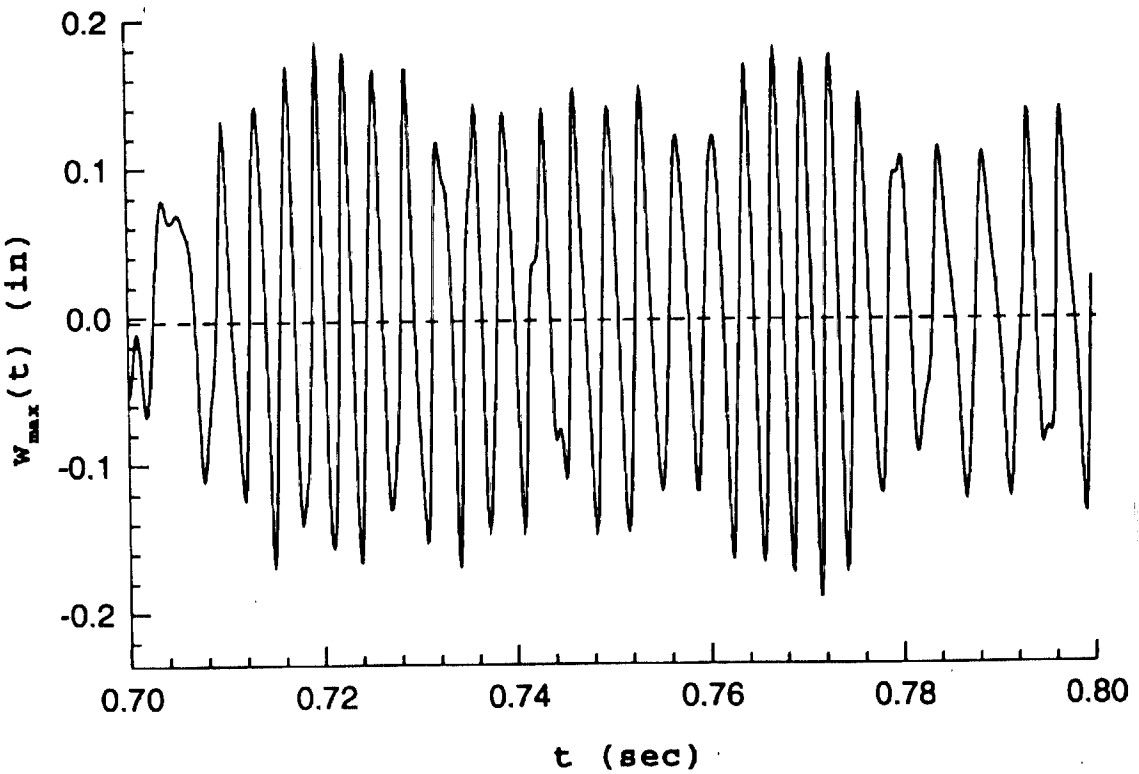

Fig.27 Nonlinear Deflection Time-history at 130db/0°F

comparison. A linear simulation time-history at the same load and with no temperature is shown in Fig.28. This figure shows a much slower moving curve since the response is dominated by low frequency oscillations. A comparison of the former two with Fig.28, gives an idea of the large high frequency content in the nonlinear response.

The power spectrum for the snap-through response is, in fact, very similar to the 130db response spectrum with no thermal load (Fig.14), except for some very low frequency content. This is due to the snap-through oscillation being picked up as a very slow-moving mode.

Uniform Temperature at Different Loads

The response data for nonlinear deflection at 130db load under uniform temperature, does not deviate much from the zero temperature response values at the same random load. Earlier research has stated that thermal loading effects are dominant at lower random load levels [83]. This aspect of plate behavior is now studied.

Two load levels are used - 130db and 90db SPL. Random response time-histories at these loads with $\Delta T = 80°F$ are generated. For the sake of better accuracy in strains, the larger model of twelve modes ($R = 12$) in the 8×8 mesh is used to generate data. Table 7 below lists rms deflection and strain values for both these load cases, at $\Delta T = 0°$ and $80°\ F$. The statistics include the non-dimensional mean and rms deflection values and the mean and rms values for the maximum y-axis strain, ϵ_y, and its curvature component, ϵ^κ. This component has been included to show its reaction to thermal load.

The maximum strain location is different for these two load cases. In the case of 130db, it is in the element close to mid-point of the long-edge one row away from the edge. In the 90db case, maximum is at the element on the edge itself.

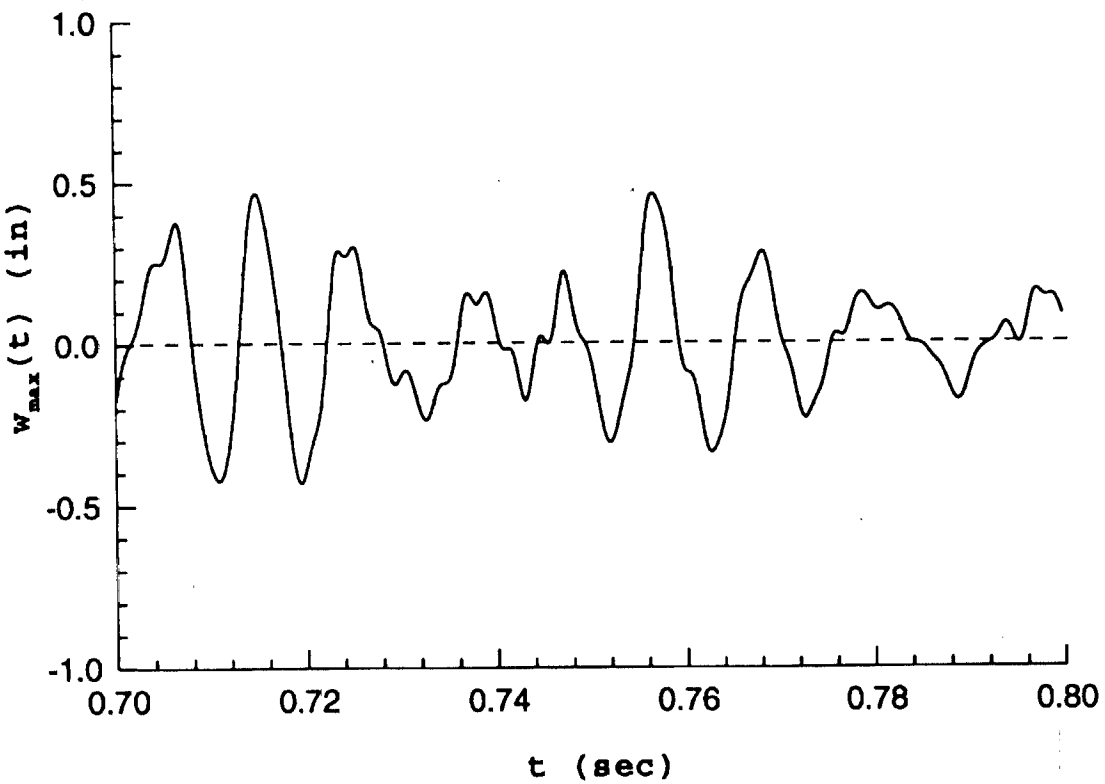

Fig.28 Linear Deflection Time-history at 130db/0°F

	130db		90db	
	$0°F$	$80°F$	$0°F$	$80°F$
$\mu\ w_{max}/h$	-0.007	-0.01	-4.31×10^{-5}	-1.101
$rms\ w_{max}/h$	1.86	1.94	0.0637	1.103
$\epsilon_\mu\ (\mu\epsilon)$	254.8	278.1	0.228	165.07
$\epsilon_{rms}\ (\mu\epsilon)$	438.47	479.12	6.25	165.6
$\epsilon_\mu^\kappa\ (\mu\epsilon)$	-0.527	-1.3	0.0043	111.9
$\epsilon_{rms}^\kappa\ (\mu\epsilon)$	217.95	244.256	6.245	112.05

Table 7. Statistics at 90db and 130db SPL

The influence of the thermal load at 90db is very pronounced, whereas at 130db there is a very small difference. Both the deflection and strain show a high mean at $80°F$. A big increase in the linear component, ϵ^κ is also observed.

The change in the responses at the lower load level is also shown in Figs.29 and 30. The first is a comparison between the power spectrum for the nonlinear deflection with and without thermal load at 90db SPL. The spectrum in this figure can be understood by the time-histories plotted in Fig.30. The vibration at $80°F$ takes place about some buckled position. This type of change is not present at 130db SPL.

Non-uniform Temperature $\Delta T = T(x, y, z)$

The thermal load modifications to model a non-uniform temperature distribution are now implemented. Data from experimental setups suggests that a panel exposed to a bank of heat lamps intended to create a temperature distribution as close to being uniform over the plate surface as possible, is, in reality, not at a uniform

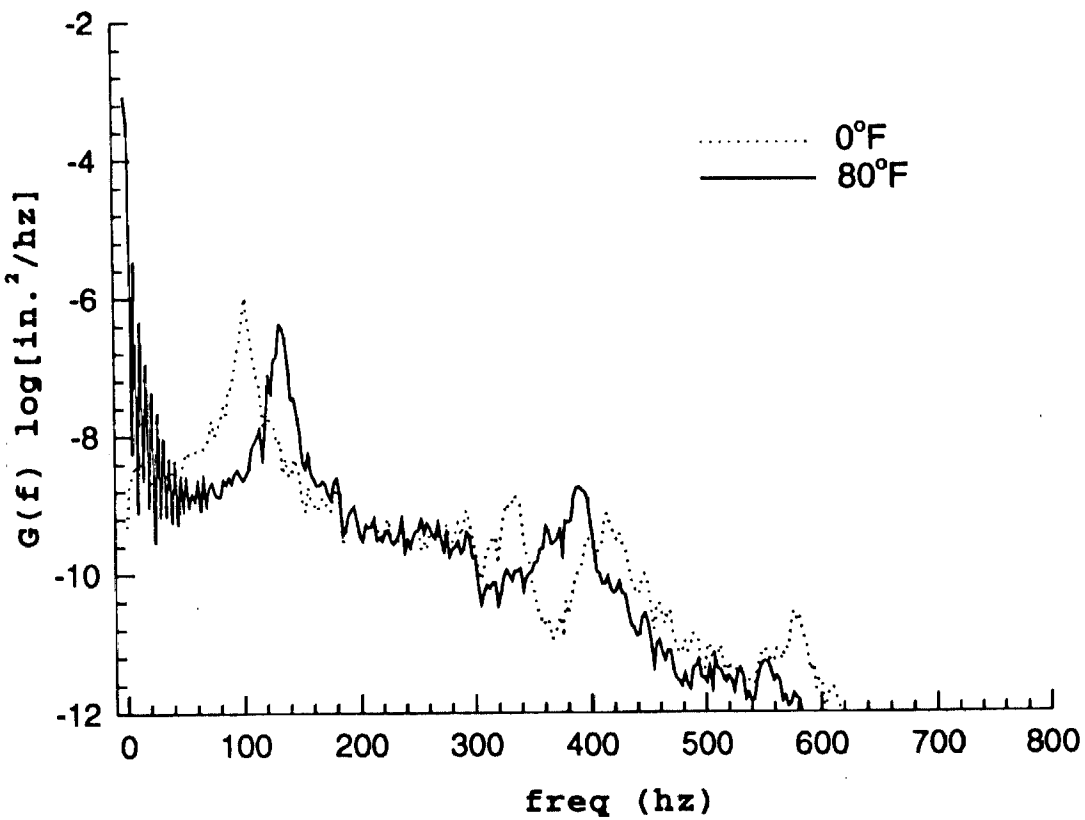

Fig.29 Power Spectrum for NL Deflection at 90db/ΔT=80°F

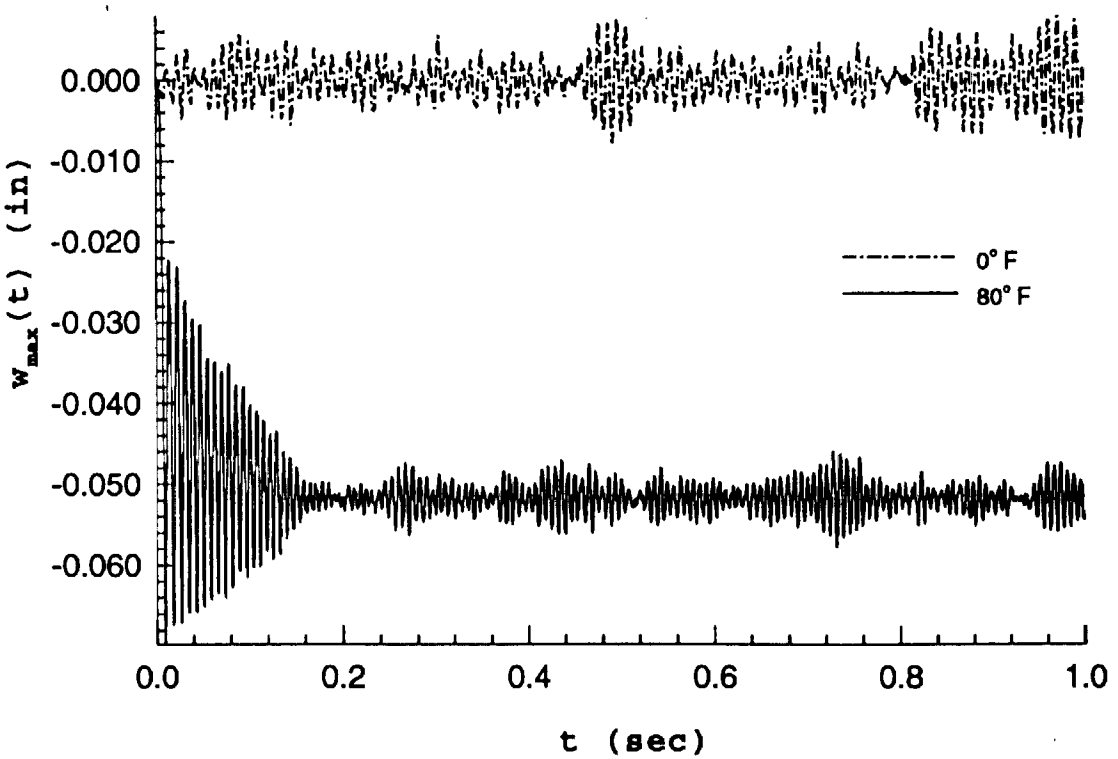

Fig.30 Time-history of NL Deflection at 90db/ΔT=0°F,80°F

temperature. There is a drop in temperature near the edges of the clamped panel [145]. This type of distribution, which is symmetric over the $x-y$ plane, is modelled here. Figure 31 shows the temperature variation assumed along both the x-axis and the y-axis for the baseline plate.

The gradient through the thickness of the plate is known to be quite small. Since the plates are thin, and the duration of exposure is sufficiently long, this seems reasonable. This gradient usually does not exceed about $20^o F$. Hence, a linear variation along the z-axis is assumed, with the maximum being on the external surface (Fig.3). Therefore, the expression for the temperature variation in the plate can be written as

$$\Delta T(x,y,z) \;=\; T(x)\,T(y)\left[\,T_o + \frac{T_1}{h}z\,\right]$$

where T_o is a constant, corresponding to the temperature increase above ambient atmospheric temperature. The slope in the z-direction is given by T_1/h.

As mentioned in the introduction, this study is motivated by the structural design requirements for the proposed high speed civil transport aircraft. It is estimated that the operating temperatures of interest are at about $350^o F$. Ambient temperatures are assumed to be $70^o F$. Therefore, if the temperature differential for the outside surface of the panel is at $280^o F$, the mid-plane temperature differential is set at $270^o F$, to accomodate the gradient. Thus $T_o = 270^o F$ and $T_1 = -20.0$. The surface distribution, $T(x,y) = T(x)T(y)$, is simply scaled by the T_o value assumed. For a uniform temperature distribution, these are set to unity and T_1 is set to zero.

Since the previous result of this section showed a small thermal load influence at the 130db baseline load level, this non-uniform temperature analysis is carried out at the lower 90db SPL load. The finite element model uses the baseline 8×8 mesh with twelve modes. The effect of each of the temperature distributions, namely, uniform temperature, $\Delta T = T_o$; temperature with surface variation only,

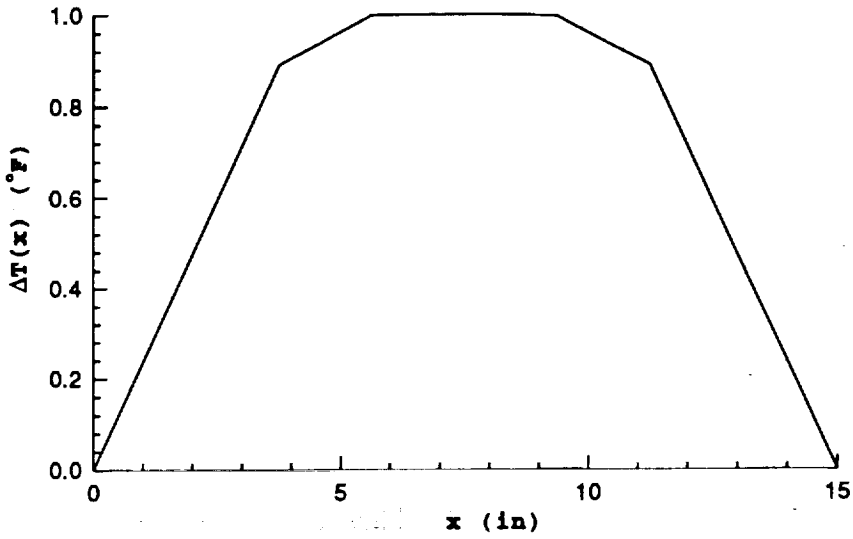

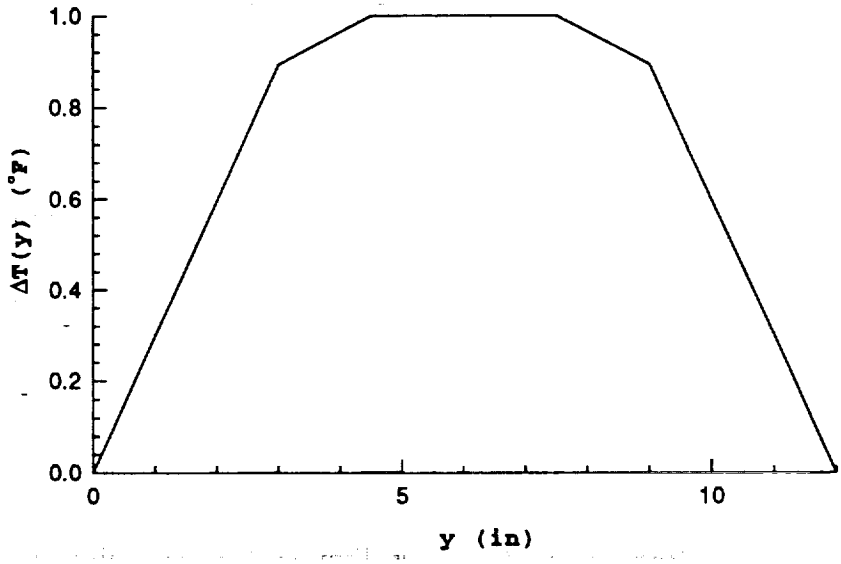

Fig.31 Components of Non-uniform Temperature Distribution

$\Delta T = T(x,y)$; and temperature with variation on the surface and through the thickness, $\Delta T = T(x,y,z)$ is studied. Results for mean and rms deflection and strain are compared for these three themal load assumptions. Table 8 lists the rms values for this case. The element with maximum strain is one row away from the edge in this case.

Overall, the differences in the temperature loadings do not seem to have affected the response characteristics to a great degree. A quantity to observe, though, is the curvature component of the strain, ϵ^{κ}. It shows a significant increase from a uniform temperature distribution to a surface gradient distribution. (In fact, at the very edge of the plate, this component was found to be larger than the numbers above, although the total strain still remained lower.) The temperature distribution, T(y), shown in Fig.31, has the largest gradient along the y-direction close to this edge. This surface gradient can be expected to create high thermal strain in this vicinity. This possibly explains the change in ϵ^{κ} seen above.

	T_o	$T(x,y)$	$T(x,y,z)$
$\mu\ w_{max}/h$	2.575	2.53	2.53
$rms\ w_{max}/h$	2.58	2.53	2.58
$\epsilon_{\mu}\ (\mu\epsilon)$	578.86	581.7	581.7
$\epsilon_{rms}\ (\mu\epsilon)$	580.6	582.7	582.7
$\epsilon^{\kappa}_{rms}\ (\mu\epsilon)$	76.6	103.3	103.3
$\epsilon^{w}_{rms}\ (\mu\epsilon)$	514.6	489.1	489.1

Table 8. Statistics vs Temperature Distribution - 90db

The inclusion of a gradient of this particular magnitude in the z-direction does not have any effect on the response statistics. The motion of the plate is so dominated by the thermal force, that the thermal moment countering the moment due to the dynamic load, makes very little difference. This may not be the case for higher gradients.

5.3.5 Grazing Load

In this section results are presented for the pressure modelled as a plane-wave travelling along the length of the plate. It is assumed that the angle of incidence of Fig.3 is fixed at 90^o. In effect, the direction of propagation is tangential to the surface of the plate, along the x-direction. The speed of sound is set at 343 m/s ($1.3504 \times 10^4 in./s$). The case of a grazing pressure distribution is no longer symmetric over the plate. The lower anti-symmetric modes, (1,2) and (2,1) must, therefore, be included in the modal transformation matrix. Similarly, the lowest membrane modes that were inactive under a normal load, may no longer be so. The plate model used in this case is of an 8×4 mesh with the first six bending modes [(1,1), (1,2), (2,1), (2,2), (1,3) and (3,1)] and four membrane modes. Thus, the total number of modes used for the grazing load model is $R = 10$.

Response data are generated at 130db SPL. Apart from the center of the plate, deflection time-histories are recorded at every node along the x-axis centerline (a total of 15 non-zero nodal values). A linear simulation with grazing angle, $\beta = 90^o$, with the six bending modes above is first carried out. The modal activity can now be compared against the modal results for $\beta = 0^o$, normal load linear analysis. Given below are rms modal displacement, $rms\ q_r$, values relative to $rms\ q_1$, the fundamental mode response. i.e.,

$$\frac{rms\ q_r}{rms\ q_1}\ , \qquad r = 1, 2, \ldots, 6$$

	(1,1)	(1,2)	(2,1)	(2,2)	(1,3)	(3,1)
$\beta = 0^o$	1.0	0.0	0.0	0.0392	0.0948	0.0638
$\beta = 90^o$	1.0	0.0261	0.1295	0.0350	0.0866	0.0279

$\frac{rms\ q_1(0^o)}{rms\ q_1(90^o)} = 1.0099$

Table 9. Rms Modal ratios

The contributions from each of these modes must be assessed with the individual mode-shapes in mind (Figs.9 and 10). The participation from modes (1,2) and (2,1) when the load is modelled with angular incidence is expected. From the modal rms values above it is clear that response in mode (1,2) is very weak. Mode (2,1) is the strongest mode of response, apart from the fundamental mode. This mode, as seen in Fig.9, has a trough and then a crest as one progresses along x-direction. Response over the plate in this shape, then, is a direct consequence of the left-to-right travelling wave assumption. The power spectrum for this grazing load response is shown in Fig.32. The spectrum at a node $3.75in.$ away from the leading edge is shown for both normal and grazing load models. This point was chosen as neither of the two additional modes, (1,2) and (2,1), will show up in the center deflection spectrum. Mode (1,2), is present in the response spectrum as a very small peak. A look at this mode in Fig.9 will show that its amplitude along the x-axis *centerline*, is small. Compounded with the relatively low modal rms level for this mode, the modal contribution in the spectrum for that particular location is negligible. The same is true for mode (2,2).

Deflection curves in Fig.33 show the centerline rms deflections recorded at each node. They are plotted for both the normal and grazing load models. There is a slight change in the shape but overall response behavior shows no significant difference. Similarly, it was found that the PDF, power spectra and peak PDF

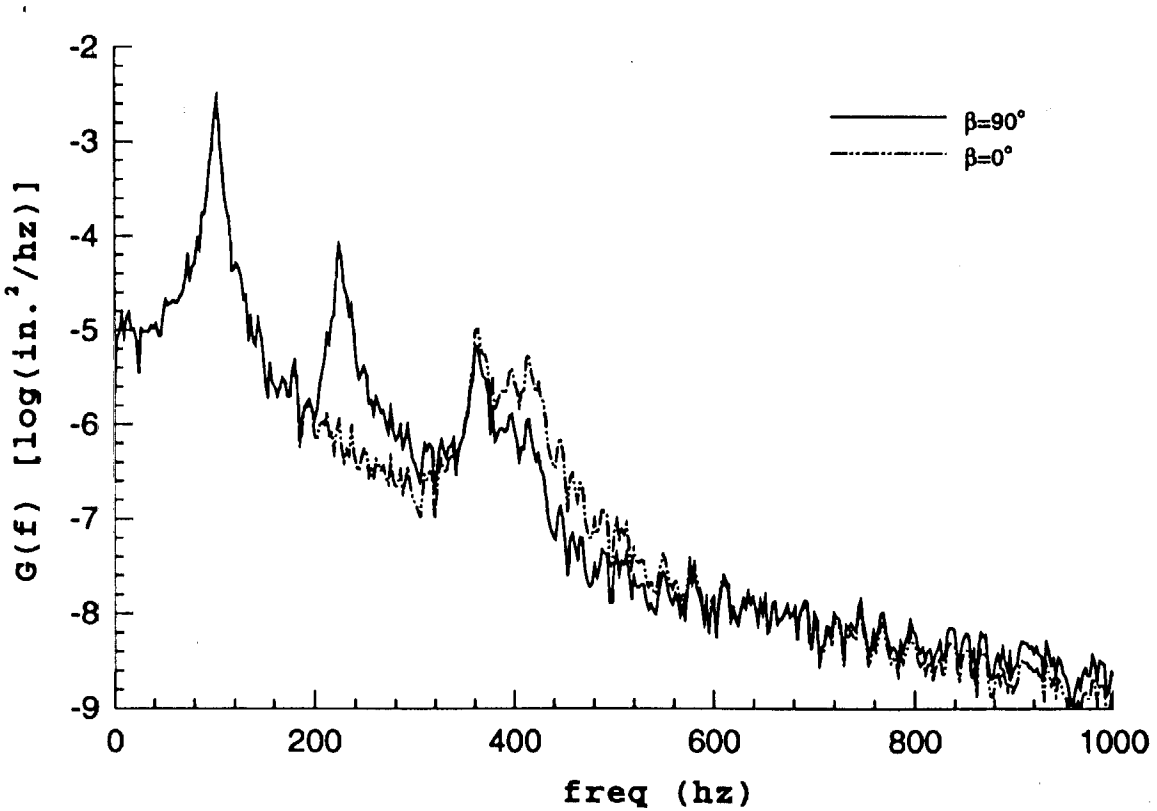

Fig.32 Power Spectrum of Linear Deflection at x=3.75in.

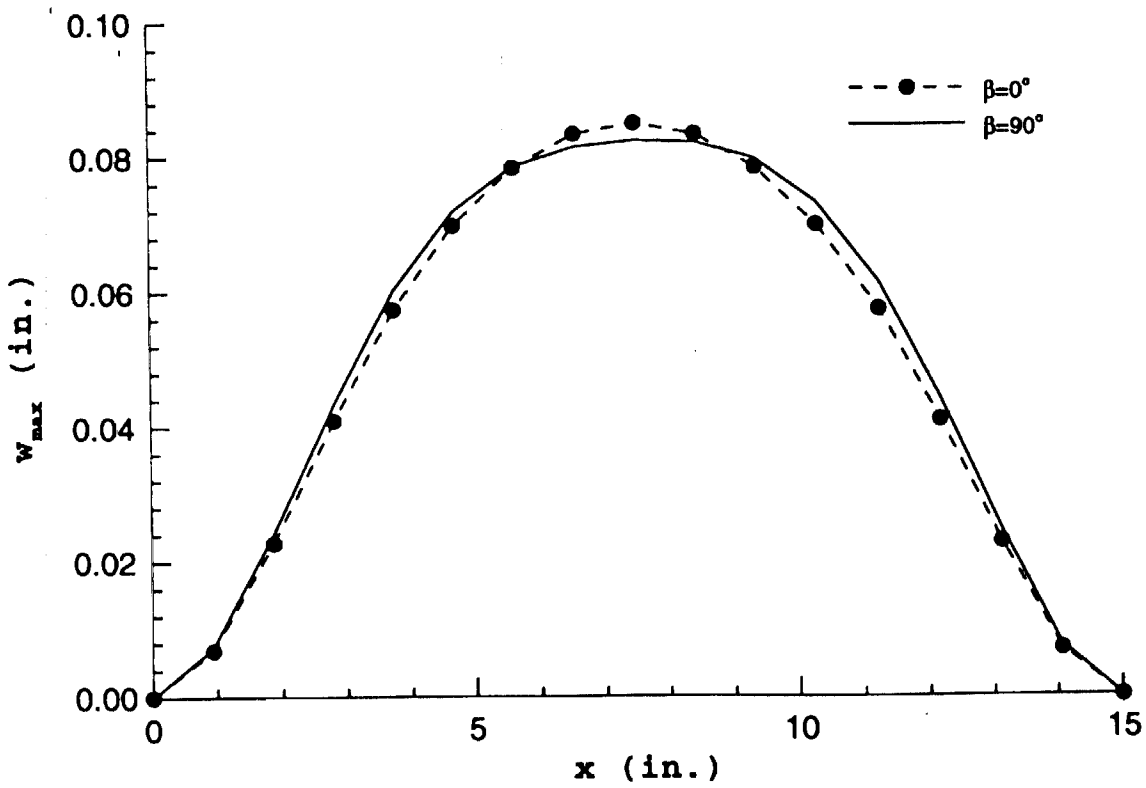

Fig.33 Centerline Nonlinear Deflection Shape at 130db SPL

distributions for maximum deflection showed little change. The power spectrum in the case of the grazing load model drops off a little more than for the normal load model, after about 500hz. The same trend was noticed in the strain response comparisons, too. None of these plot are displayed since the changes are rather insignificant.

5.3.6 Variation of Other Parameters

A few additional cases, involving parameters such as initial stresses from static compressive loads, N^s, quadrilateral elements, and plate thickness are studied and results are presented here.

Plate Thickness

The thickness parameter is studied by increasing the thickness of the baseline plate configuration ten-fold. The thickness of each layer is increased from 0.006 in. to 0.06 in., resulting in total plate thickness, $h = 0.48$ in., with an a/h ratio of 31.25. The 8×4 mesh with a total of six modes (4 bending and 2 membrane) is used. Linear and nonlinear simulations at 130db SPL are conducted. The centerline deflection values are $\sigma/h = 0.002$ for both the linear and nonlinear simulations. The strain data, too, were found to be the same for both the linear and nonlinear simulations. This implies that the responses of the plate are in the linear regime even at 130db SPL. The power spectral densities, as expected, were found to be identical in the two cases. As a matter of fact, although four bending modes were used, the modal response at the first mode seemed to be the strongest.

Initial Stress

The nonlinear random responses of the baseline panel under an initial stress distribution are dealt with next. The initial stress distribution is accounted for using constant static compressive loads on all its edges. There is, thus, no initial moment

distribution in the plate. All other parameters of the simulation are the same as used in the previous example. Simulation is at 130db SPL using a total of six modes (4 bending and 2 membrane). The critical buckling static load for all four clamped edges under compression was computed at N_x, $N_y = N_{cr} = 20.23\,lbs/in$. Therefore, an edge load, $N^s = N_{cr}/2$ is used for this case. It may be recalled here that edge loads are set to be less than critical buckling load in the problem definition (see Eqs.2.3.4 and 2.3.9).

The rms results for maximum deflection show the reduced stiffness in the plate due to this additional load. The value obtained is $\sigma/h = 1.88$. The corresponding figure when edge loads are absent is 1.77.

Quadrilateral Elements

The Lagrangian element used in the finite element model in this study has so far been used only as a rectangular element. This element can actually be used, more generally, as a quadrilateral. This feature of the finite element model is demonstrated with an example. Fig.34 displays the mesh structure used. The size of the mesh used was dictated by the necessity to generate quadrilateral shaped elements without any of them being too skewed. The mesh uses five elements along y-axis and 8,6 elements along the longer x-axis edges, respectively. The lower number of elements, along the y-axis makes the model stiffer along this direction, compared to the 8×8 mesh. The modal transformation matrix used, consisted of 4 bending modes and 2 membrane modes ($R = 6$). In order to compare data from this model against the 8×8 baseline data, the four bending mode solution from the convergence studies (Fig.12) is used here. Nonlinear simulation at 130db produced the following rms results

$\sigma/h = 1.78$ vs 1.78 for rectangular 8×8 mesh

$\epsilon_{rms} = 497\ \mu\epsilon$ vs $430\ \mu\epsilon$ for rectangular 8×8 mesh

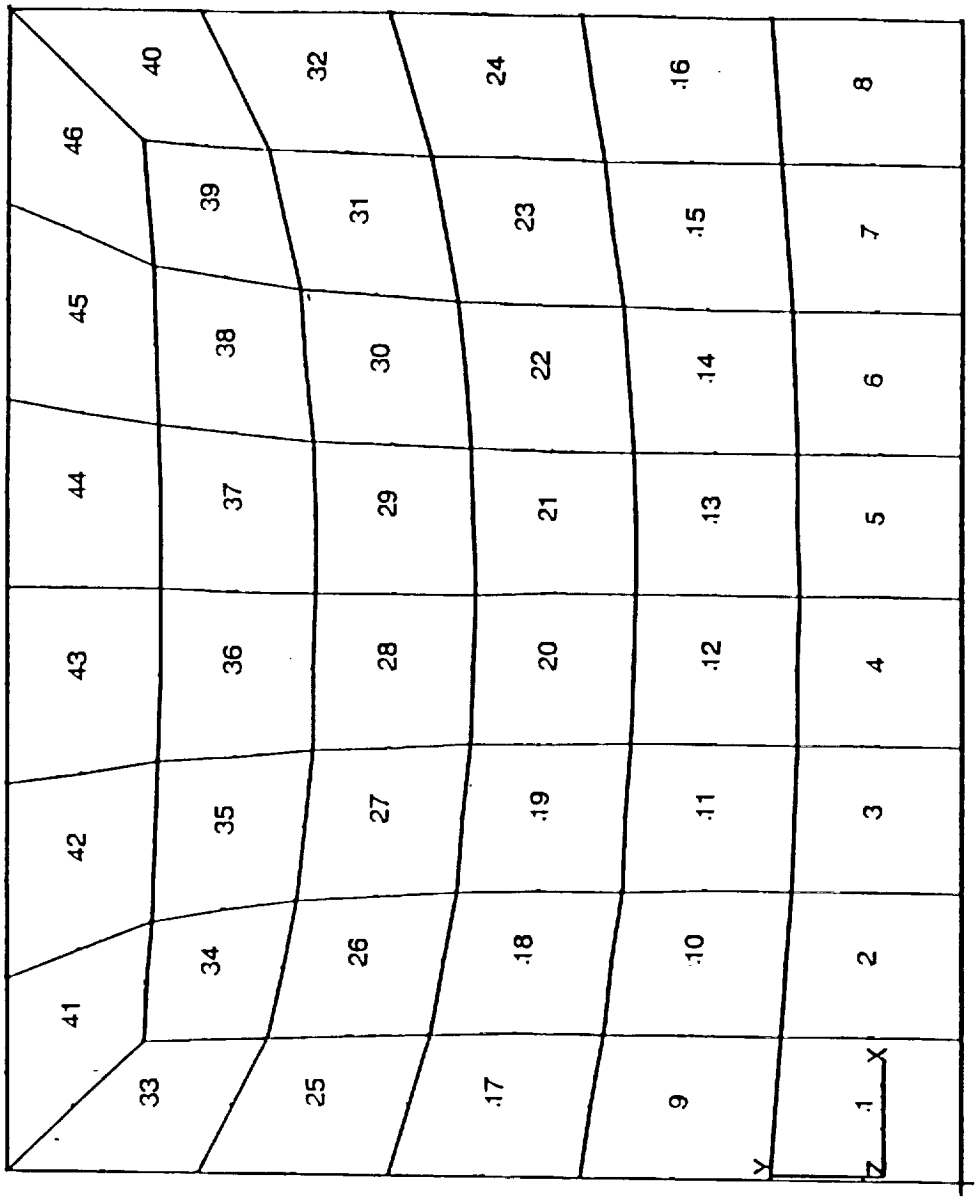

Fig.34 Quadrilateral Element Mesh for Baseline Plate

The deflection numbers above are compared at almost exactly the same location. The strain data are for elements of slightly different sizes. It is safe to say that most of the change in results is due to the change in mesh size. It was observed that the x-axis strain rms showed a similar degree of change.

Chapter 6

CONCLUSIONS

A Monte Carlo simulation technique to study the response of composite plates under combined acoustic and thermal loading has been implemented. Finite element equations in the physical degrees of freedom were reduced to a smaller set of modal equations of motion. An implicit numerical integration routine using a weighting function was encoded. A modified pressure distribution model was also generated. Response characteristics were obtained under realistic temperature distribution assumptions.

The modal decomposition of the large degree of freedom finite element model proved very effective in reducing the number of equations used for obtaining solutions. The formulation facilitated the inclusion of nonlinear stiffnesses without having to build them up at every time-step. Especially for a time-domain simulation procedure this technique is quite definitely a necessity. The computational time required otherwise will make the simulation method impractical.

The numerical algorithm used appears to be a very useful tool [106]. The extension of the Wilson-θ method to the nonlinear dynamic equation has worked effectively. The algorithm is stable for fairly large nonlinearities at time-steps that are not too small, ($\Delta t = 10^{-4}$). But the step-size cannot probably be reduced further since this is pretty close to the limit where amplitude decay and period elongation are small. The use of a nonlinear algebraic equation at each time-step

may be problem dependent. It was observed that for cases with moderate degrees of nonlinearity (low σ/h), solution of linearized equations at every time-step gave acceptable results. These results showed consistently higher rms deflection values. It is not likely, however, that strain results will be as accurate by using linearized equations within each time-step. In general, doing away with the iterations within time-steps, in effect becoming an explicit integration scheme, may be quite acceptable for systems with moderate nonlinearities.

The modified load model was an effective tool in bringing out the complete spectrum of modal response. The implementation of this space-time correlated distribution did not add significantly to the computational cost. There was not much difference in the overall response characteristics, although the strain response shows a small degree of change. This is only true for the dimensions of the plate used in this study, relative to acoustic wavelengths. The grazing load model may show greater differences for a large or long plate. It will probably be more realistic to use a completely random (spatial and temporal) pressure distribution over the plate with this simulation scheme, since it can be implemented without much increase in computational effort.

The results of simulations under combined acoustic and thermal loads have shown some response features not reported before. The influence of higher thermal buckling temperatures has been observed here, due to the unrestricted nature of the formulation. The data presented in Chapter 5, were at a high random load of 130db. The same analysis at 90db, may have shown the behavior around buckling temperatures in a more dramatic fashion. The phenomenon of snap-through behavior has also been simulated, although there is no way to approximately predict its onset. The surface variation used for the temperature increment gives a more realistic estimate of the temperature distribution in a plate. It would be interesting to record strain data at locations where the surface thermal gradients are the

steepest. Under a more severe thermal loading condition it is quite likely that the maximum strain location will no longer be close to the long-edge mid-point for this type of plate.

The consideration of thermal moments induced by a temperature gradient through the plate thickness, does not seem to be much of a factor in the response behavior. Due to the direction of gradient used (normal to the heated surface is opposite to the dynamic load direction), there is probably a counteracting effect from the thermal moments. But the alteration in the response characteristics due to this gradient is still negligible. This is more so when the thermal load dominates the dynamic load, at low decibel levels [83].

A significant observation of this study has been the sensitivity of strain response characteristics to almost every parameter that influences the response behavior, including element type and mesh size used, membrane interpolation functions used, number of bending and membrane modes used, temperature distribution and load model used. In practical applications under such loading conditions as discussed in this work, it is the fatigue life performance of these structural components which is of critical importance. This needs accurate information on the strain response behavior of structures. Hence, it is important that strain response prediction models are accurate.

In this context, the selection of mode-shapes to obtain converged solutions, is a critical part of the model definition process. In turn, it depends on the criterion chosen for modal convergence, namely, frequencies, deflection or strain. The number of modes required, in turn, decides the mesh refinement procedure. Given the sensitivity of strain responses to all these factors, it is imperative that the convergence criterion, for both mesh refinement and modal convergence studies, be based on strain rather than deflections or natural frequencies. This tends to be the most time-consuming aspect of problem solution. The mesh required to provide accurate

strain results usually turns out to be large. In this study the eigenvector computation algorithms used were all full-system solution methods. The computation time for such solution processes for large degree-of-freedom systems, as we know, increases tremendously. It is therefore recommended for future applications that the eigenvalue-eigenvector computation algorithm used, be of the type that generates a limited number of modes, say, one based on the Rayleigh quotient method. Once a good finite element modal transformation matrix has been obtained, the solution for any type of loading case for that particular laminate follows through with no restrictions. It is, therefore, recommended that future work focus on improved treatment of all these factors.

Another aspect dealing with the particular type of laminate used in this study is with regard to boundary conditions. It has been observed that the presence of angle-ply layers removes the symmetry along the x, y-axes that a cross-ply laminate would have. This, therefore, precludes the use of quarter-plate models in the finite element mesh. The use of a quarter-plate model enforces symmetry conditions on all rotations and displacements, where no such symmetry exists.

The simulation technique in combination with modal decomposition is probably the best tool to build on, for analytical comparison with test data. It is also the best way to expand into coupled structural-acoustic prediction models. Its strength lies in its ability to model complicated problems with a minimum number of assumptions and restrictions imposed. A vast library of time-histories can be used to give a wide range of statistical and spectral information that puts the response characteristics in clear perspective. In the process, one can observe behavioral phenomena not otherwise detected by other analytical approaches. Such a simulation, with a thorough modelling and statistical analysis of random responses under combined loading conditions is, possibly, the major contribution of this work.

REFERENCES

1. Lighthill, M. J., "On sound generated aerodynamically I: General Theory", Proc. Roy. Soc., 1952, A211, pp. 564-587.

2. Lansing, D. L., Drischler, J. A., Brown, T. J., Mixson, J. S., "Dynamic loading of aircraft surfaces due to jet exhaust impingement", AGARD CP 113, 1972.

3. Scholton, R., "Influence of the ground on the the near field noise levels of a jet supported V/STOL", AGARD CP 113, 1973.

4. Bull, M. K., "Wall pressure fluctuations associated with subsonic turbulent boundary-layer flow", J. Fluid Mech., 28, 1967, p 719.

5. Coe, C. F., Chyu, W. J., "Pressure fluctuation inputs and response of panels underlying attached and separated supersonic turbulent boundary-layers", NASA TM-X-62189, 1972.

6. Hess, R. W., Herr, R. W., Mayes, W. H., "A study of the acoustic fatigue characteristics of some flat and curved panels exposed to random and discrete noise", NASA TN D1, 1959.

7. Nelson, T. F., "An investigation of the effects of surrounding structure on sonic fatigue", NASA CR 1536, 1970.

8. Clarkson, B. L., Ford, R. D., "The response of a typical aircraft structure to jet noise", J. Roy. Aero. Soc, 66, 1962, pp. 31-40.

9. Clarkson, B. L. "The design of structures to resist jet noise fatigue", J. Roy. Aero. Soc, 66, 1962, pp. 603-616.

10. McGowan, P. R., "Structural design for acoustic fatigue", ASD TDR 63-820, 1963.

11. Rudder, F. F., Plumbee, H. E., " Sonic fatigue design guide for military aircraft", AFFDL TR 74-112, 1974.

12. Jacobson, M. J. "Sonic fatigue design data for bonded aluminum aircraft structures", AFFDL 77-45, 1977.

13. Holehouse, I., " Sonic fatigue of diffusion bonded titanium sandwich structure", AGARD CP-113, 1973.

14. Jacobson, M. J., van der Hyde R. C. W., "Acoustic fatigue design information for honeycomb panels with fiber reinforced facings", J. Aircraft, 9, 1972, pp. 31-42.

15. Wolfe, N. D., Jacobson, M. J.," Design and sonic fatigue characteristics of composite material components", AGARD CP-113, 1973.

16. White, R. G., "A comparison of some statistical properties of the responses of aluminum alloy and CFRP plates to acoustic excitation", Composites, 9 1978, pp. 251-258.

17. White, R. G., Mousley, R. F., "Dynamic response of CFRP plates under the action of random acoustic loading", Proc. 4th Int. Conf. Composite Structures, Paisley College of Technology, July 1987, pp. 1519-1535.

18. Holehouse, I., " Sonic fatigue design techniques for advanced composite aircraft structures", AFWAL-TR 80-3019, 1980.

19. Soovere, J., "Sonic fatigue testing of an advanced composite aileron", J. Aircraft, 19, 1982, pp. 304-310.

20. Jacobson, M. J., "Sonic fatigue of advanced composite panels in thermal environments", J. Aircraft, 20, 1083, pp. 282-288.

21. Roussos, L. A., Heitman, H. E., Rucker C. E., "Predicted and measured strain response of rectangular panels due to acoustic loading", AIAA, 86-1931, 1986.

22. Roussos, L. A., Brewer, T. K., "Effect of boundary conditions on dynamic response of rectangular panels", AIAA, 87-0935, 1987.

23. van der Hyde, R. C. W., Kolb, A. W., "Sonic fatigue resistance of lightweight aircraft structures", AGARD CP 113, 1973.

24. Mei, C., Wentz, K. R., "Analytical and experimental nonlinear response of rectangular panels to acoustic excitation", AIAA, 82-0733, 1982, pp. 514-520.

25. Bennouna, M. M., White, R.G., "The effects of large vibration amplitudes on the dynamic strain response of a clamped-clamped beam with consideration of fatigue life", J. Sound Vibn., 96(3), Oct 1984, pp. 281-308.

26. Ng, C. F., White, R. G., "Dynamic behavior of postbuckled composite plates under acoustic excitation", AIAA, 86-0933, 1986, pp. 435-444.

27. White, R. G., Teh, C. E., "Dynamic behavior of isotropic plates under combined acoustic excitation and static in-plane compression", J. Sound Vibn., 75, 1981, pp. 527-547.

28. Robinson, J. H., Rizzi, S. A., Clevenson, S. A., Daniels, E.F., "Large deflection random response of flat and blade stiffened carbon-carbon panels", AIAA, 92-2390, 1992.

29. Mei, C.,"Large amplitude response of complex structures due to high intensity noise", AFFDL-TR-79-3028, 1979.

30. Miles, J. W.,"On structural fatigue under random loading", J. Aero. Sc., 21(11), 1954, pp. 753-762.

31. Powell, A., "On the fatigue failure of structures due to vibrations excited by random pressure fields", JASA, 30, 1958, 1130-1135.

32. Samuels, J. C., Eringen, A. C., "Response of simply supported Timoshenko beam to a purely random gaussian process", J. Appl. Mech., 25, 1958, pp. 496-500.

33. Eringen, A. C., "Response of beams and plates to random loads", J. Appl. Mech., 24, 1957, pp. 46-52.

34. Clarkson, B. L., "Stresses in skin panels subjected to random acoustic loads", J. Roy. Aero. Soc., 72, 1968, pp. 1000-1010.

35. Blevins, R. D., "An approximate method for sonic fatigue analysis of plates and shells", J. Sound Vibn., 129(1), 1989, pp. 51-71.

36. Bogdanoff, J. C., Goldberg, J. E., "On Bernouli-Euler beam theory with random excitation", J. Aero. Sc, 27, 1960, pp. 371-376.

37. Crandall, S. H., Yildiz, A., "Random vibration of beams", J. Appl. Mech., 29, 1962, pp. 267-275.

38. Mercer, C. A., "Response of a multi-supported beam to a random pressure field", J. Sound Vibn., 2 (3), 1965, pp. 293-306.

39. Elishakoff, I., "Random vibrations of orthotropic plates clamped or simply supported all around", Acta Mechanica, 28, 1977, pp. 165-176.

40. Caughey, T. K., "Nonlinear theory of random vibrations", Adv. Appl. Mech., 11, 1971, pp. 209-253.

41. Crandall, S. H., "The envelope of random vibration of a lightly damped nonlinear oscillator", Zagadnienia Drgan Neilinionwych, 5, 1964, pp. 120-130.

42. Caughey, T. K., "Derivation and application of the Fokker-Planck equation to discrete nonlinear dynamic systems subjected to white random excitation", JASA, 35(11), 1963, pp. 1683-1692.

43. Lyon, R. H., "On the vibration statistics of a randomly excited hard spring oscillator", JASA, 32, 1960, pp. 716-719.

44. Lyon, R. H., "On the vibration statistics of a hard spring oscillator II", JASA, 33, 1961, pp. 1395-1403.

45. Caughey, T. K., Ma, F., "The exact steady-state solution of a class of nonlinear stochastic systems", Int. J. Nonlinear Mech., 17(3), 1982, pp. 137-142.

46. Nash, W. A., "Response of structures to random noise", AFOSR-TR-73-2280, 1973.

47. Ahmadi, G., Tadjbakhsh, Farshad, M., "On the resposne of nonlinear plates to random loads", Acustica, 40(5), 1978, pp. 316-322.

48. Ariaratnam, S. T., "Response of a loaded nonlinear spring to random excitation", J. Appl. Mech., 29, 1962, pp. 483-485.

49. Herbert, R. E., "Random vibrations of a nonlinear elastic beam", JASA, 36(11), 1964, pp. 2090-2094.

50. Herbert, R. E., "Random vibrations of plates with large amplitudes", J. Appl. Mech., 32, 1965, pp. 547-552.

51. Crandall, S. H., "Perturbation techniques for random vibration of nonlinear systems", JASA, 35(11), 1963, pp. 1700-1705.

52. Tung, C. C., "The effects of runway roughness on the dynamic response of airplanes", J. Sound Vibn., 5(1), 1967, pp. 164-172.

53. Newland, D. E., "Energy sharing in the random vibration of nonlinearly coupled modes", J. Inst. Math. Appl., 1(3), 1965, pp. 199-207.

54. Lyon, R. H., "Response of a nonlinear string to random excitation", J. Appl. Mech., 42, 1975, pp. 891-893.

55. Stratonovitch, R. L., "Topics in the theory of random noise", vol.1, Gordon and Breach, 1964.

56. Iwan, W. D., Spanos, P.-T. D., "Response envelope statistics for nonlinear oscillators with random excitation", J. Appl. Mech., 45, 1978, pp. 170-174.

57. Roberts, J. B., "The energy envelope of a randomly excited nonlinear oscillator", J. Sound Vibn., 60, 1978, pp. 177-185.

58. Roberts, J. B., Spanos, P.-T. D., "Stochastic averaging: An approximate method for solving random vibration problems", Int. J. Nonlinear Mech., 21(2), 1986, pp. 111-134.

59. Maymon, G., "Response of geometrically nonlinear elastic structures to acoustic excitation - an engineering oriented computational procedure", Computers and Structures, 18(4), 1984, pp. 647-652.

60. Booton, R. C., "Nonlinear control systems with random inputs", IRE Trans., Circuit Theory, CT-1, 1954, pp. 9-18.

61. Caughey, T. K., "Equivalent linearization techniques", JASA, 35(11), 1973, pp. 1706-1711.

62. Atalik, T. S., Utku, S., "Stochastic linearization of multi-degree of freedom nonlinear systems", Int. J. Earthquake Engg. and Struc. Dynm., 4, 1976, pp. 411-420.

63. Kazakov, I. E., "Generalization of the method of statistical linearization to multi-dimensional systems" Automation Remote Control, 26, 1965, pp. 1201-1206.

64. Crandall, S. H., "The spectrum of random vibration of a nonlinear oscillator", Proc. 11th Int. Cong. Appl. Mech., Munich, 1964.

65. Smith, P. W., Jr, "Response of nonlinear structures to random excitation", JASA, 34, 1962, pp. 827-835.

66. Lyon, R. H., "Equivalent linearization of the hard-spring oscillator", JASA, 32, 1960, pp. 1161-1162.

67. Iwan, W. D., Yang, I.-M., "Application of statistical linearization techniques to nonlinear multi-degree-of-freedom systems", J. Appl. Mech., 39(2), 1972, 545-550.

68. Dimentberg, M. F., "Oscillations of a system with nonlinear cubic characteristics under narrow-band random excitation", Mech. Solids., 6(2), 1971, pp. 142-146.

69. Caughey, T. K., "Response of nonlinear string to random loading", J. Appl. Mech., 26, 1959, pp. 341-344.

70. Caughey, T. K., "Nonlinear theory of random vibrations", Adv. Appl. Mech., 11, 1971, pp. 209-253.

71. Iwan, W. D., Yang, I.-M., "Statistical linearization for nonlinear structures", ASCE J. Engg. Mech. Div., 97, 1971, pp. 1609-1623.

72. Iwan, W. D., "A generalization of the method of equivalent linearization", Int. J. Nonlinear Mech., 8, 1973, pp. 279-287.

73. Spanos, P.-T. D., "Formulation of stochastic linearization for symmetric or asymmetric M.D.O.F. nonlinear systems", J. Appl. Mech., 47, 1980, 209-211.

74. Roberts, J. B., "Stationary response of oscillators with non-linear damping to random excitation", J. Sound Vibn., 50, 1976, pp. 145-156.

75. Busby, H. R., Weingarten, V. I., "Response of a nonlinear beam to random excitation", ASCE J. Engg. Mech. Div., 99, 1973, pp. 55-68.

76. Langley, R. S., "Stochastic linearization of geometrically non-linear finite element models", Computers and Structures, 27(6), 1987, pp. 721-727.

77. Seide, P., "Nonlinear stresses and deflections of beams subjected to random time dependent uniform pressure", J. Engg. for Industry, 98(3), 1976, pp. 1014-1020.

78. Mei, C., Prasad, C. B., "Effects of nonlinear damping on random response of beams to acoustic loading", J. Sound Vibn., 117(1), 1987, pp. 173-186.

79. Mei, C., Prasad, C. B., "Multimode large deflection random response of beams with nonlinear damping subjected to acoustic loading", AIAA, 87-2712.

80. Mei, C., Paul, D. B., "Nonlinear multimode response of clamped rectangular plates to acoustic loading", AIAA Journal, 24(4), 1986, pp. 643-648.

81. Mei, C., "Response of nonlinear structural panels subjected to high intensity noise", AFWAL-TR-80-3018, 1980.

82. Mei, C., "Large deflection multimode response of clamped rectangular panels to acoustic excitation", AFWAL-TR-83-3121, 1, 1983.

83. Lee, J., "Large-amplitude plate vibration in an elevated thermal environment", WL-TR-92-3049.

84. Miles, R. N., "Equivalent linearization for fatigue life estimates of a nonlinear structure", AIAA, 89-1355.

85. Wentz, K. R., Paul, D. B., Mei, C., "Large deflection random response of symmetrically laminated composite plates", Shock and Vibn. Bulletin, 52, 1982, pp. 99-111.

86. Gray, C. E., Jr., Decha-Umphai, K., Mei, C., "Large deflection, large amplitude vibrations and random response of symmetrically laminated rectangular plates", J. Aircraft, 22, 1985, pp. 929-930.

87. Mei, C., Wentz, K. R., "Large amplitude random response of angle-ply laminated composite plates", AIAA Journal, 20, 1982, pp. 1450-1458.

88. Mei, C., Prasad, C. B., "Response of symmetric rectangular composite laminates with nonlinear damping subjected to acoustic loading", AIAA, 86-1933.

89. Mei, C., Prasad, C. B., "Effects of large deflection and transverse shear on response of rectangular symmetric composite laminates subjected to acoustic loading", J. Comp. Mtls., 23, 1989, pp. 606-639.

90. Prasad, C. B., Mei, C., "Large deflection random response of cross-ply laminated plates with elastically restrained edges and initial imperfections", AIAA, 88-2239.

91. Prasad, C. B., Mei, C., "Effects of transverse shear on large deflection random response of symmetric composite laminates with mixed boundary conditions", AIAA, 89-1356.

92. Crandall, S. H., Zhu, W. Q., "Random vibration: A survey of recent developments", J. Appl. Mech., vol.50, 1983, pp. 953-962.

93. Roberts, J. B., "Response of nonlinear mechanical systems to random excitation, Part I: Markov methods", Shock and Vibn. Digest, 13(4), 1981, pp. 17-28.

94. Roberts, J. B., "Response of nonlinear mechanical systems to random excitation, Part II: Equivalent linearization and other methods", Shock and Vibn. Digest, 13(5), 1981, pp. 15-29.

95. To, C. W. S., "Random vibration of nonlinear systems", Shock and Vibn. Digest, 19(3), 1987, pp. 3-9.

96. Jacobs, L. D., Lagerquist, D. R., "A finite element analysis of simple panel response to turbulent boundary layers", AFFDL-TR-67-81, 1967.

97. Olson, M. D., Lindberg, G. M., "Jet noise excitation of an integrally stiffened panel", J. Aircraft, 8, 1971, pp. 847-855.

98. Olson, M. D., "A consistent finite element method for random response problems", Computers and Structures, 2, 1972, pp. 163-180.

99. Dey, S. S., "Finite element method for random response of structures due to stochastic excitation", Comp. Meth. Appl. Mech. and Engg, 20, 1979, pp. 173-194.

100. Newsom, C. D., Fuller, J. R., Sherrer, R. E., "A finite element approach for the analysis of randomly excited complex elastic structures", AIAA, 67-23696, 1967, pp. 125-134.

101. Hwang, C., Pi, W. S., "Nonlinear acoustic response analysis of plates using the finite element method", AIAA Journal, 10(3), 1972, pp. 276-281.

102. Mei, C., Chiang, C. K., "A finite element large deflection random response analysis of beams and plates subjected to acoustic loading", AIAA, 87-2713, 1987.

103. Chiang, C. K., Mei, C., "A finite element large deflection multiple-mode random response analysis of beams subjected to acoustic loading", Proc. 3rd Int. Conf. Recent Advances in Struc. Dynm., University of Southampton, UK, 1988, pp. 769-779.

104. Locke, J. E., Mei, C., "A finite element formulation for the large deflection random response of thermally buckled beams", AIAA, 89-1354, 1989.

105. Locke, J. E., "Finite element large deflection random response of thermally buckled plates", J. Sound Vibn., 160(2), 1993, pp. 301-312.

106. Robinson, J. H., "Variational finite element-tensor formulation for the large deflection random vibration of composite plates", AIAA, 91-1240, 1991.

107. Chen, C. C.-T., "Geometrically nonlinear random vibrations of structures", PhD Dissertation, Purdue University, 1990.

108. Chen, C. C.-T., Yang, H. T. Y., "Geometrically nonlinear random vibrations of laminated composite plate", Proc. 8th Int. Conf. on Comp. Mtls., Honolulu, HI, 1991, pp. 34-B-1 to 34-B-10.

109. Seide, P., Adami, C., "Dynamic stability of beams in a combined thermal-acoustic environment", AFWAL-TR-83-3072, 1983.

110. Dowell, E. H., "Transmission of noise from a turbulent boundary layer through a flexible plate into a closed cavity", JASA, 46, 1969, pp. 238-252.

111. Dyer, I., "Response of plates to a decaying and convecting random pressure field", JASA, 31(7), 1959, pp. 922-928.

112. Iwankiewicz, R., Sobczyk, K., "Dynamic response of linear structures to correlated random impulses", J. Sound Vibn., 86(3), 1983, pp. 303-317.

113. Belz, D. J., "A numerical study of non-linear vibrations induced by correlated random loads", Int. J. Non-linear Mech., 1, 1966, pp. 139-145.

114. Zienkiewicz, O. C., Wood, W. L., Hines, N. W., Taylor, R. L., "A unified set of single-step algorithms, Part I: General formulation and applications", Int. J. Num. Meth. in Engg., 20, 1984, 1529-1552.

115. Shinozuka, M., "Simulation of multivariate and multidimensional random processes", JASA, 49(1), 1971, pp. 357-367.

116. Shinozuka, M., Jan, C. M., "Digital simulation of random processes and its applications", J. Sound Vibn., 25(1), 1972, pp. 111-128.

117. Shinozuka, M., "Monte Carlo solution of structural dynamics", Computers and Structures, 2, 1972, pp. 855-874.

118. Shinozuka, M., Wen, Y.-K., "Monte Carlo solution of nonlinear vibrations", AIAA Journal, 10(1), 1972, pp. 37-40.

119. Wittig, L. E., Sinha, A. K., "Simulation of multicorrelated random processes using the FFT algorithm", JASA, 58(3), 1975, pp. 630-634.

120. Sengupta, G., "Vibration response and sound radiation from beams, plates and cylinders excited by nonhomogeneous random pressure fields", AIAA, 84-2327, 1984.

121. Vaicaitis, R., Jan, C. M., Shinozuka, M., "Nonlinear panel response and noise transmissions from a turbulent boundary layer by a Monte Carlo approach", AIAA, 72-199, 1972.

122. Vaicaitis, R., Dowell, E. H., Ventres, C. S., "Nonlinear panel response by a Monte Carlo approach", AIAA Journal, 12(5), 1974, pp. 685-691.

123. Vaicaitis, R., "Acoustic fatigue: A Monte Carlo approach", AIAA, 87-0916, 1987.

124. Vaicaitis, R., Choi, S. T., "Nonlinear response and fatigue of stiffened panels", Prob. Engg. Mech., 4(3), 1989, pp. 150-160.

125. Vaicaitis, R., Choi, S. T., "Sonic fatigue and nonlinear response of stiffened panels", AIAA, 89-1101, 1989.

126. Vaicaitis, R., Kavallieratos, P. A., "Nonlinear response of composite panels to random excitation", AIAA, 93-1426-CP.

127. Schneider, C. W., "Acoustic fatigue of aircraft structures at elevated temperatures", AFFDL-TR-73-155, parts I and II, 1973.

128. Soovere, J., "The effect of acoustic/thermal environments on advanced composite fuselage panels", J. Aircraft, 22, 1985, pp. 257-263.

129. Schneider, C. W., Rudder, F. F., "Acoustic fatigue resistance of aircraft structures at elevated temperatures", AIAA, 73-994, 1973.

130. Jacobson, M. J., Maurer, O. F., "Oil-canning of metallic panels in thermal-acoustic environments", AIAA, 74-982, 1974.

131. Ng., C. F., Clevenson, S. A., "High intensity acoustic tests of a thermally stressed aluminum plate in TAFA", NASA TM 101552, 1989.

132. Ng., C. F., Wentz, K. R., "The prediction and measurement of thermoacoustic response of plate structures", AIAA, 90-0988, 1990.

133. Clarkson, B. L., "Review of sonic fatigue technology", NASA CR 4587, 1994.

134. Vaicaitis, R., "Time domain approach for nonlinear response and sonic fatigue of NASP thermal protection systems", AIAA, 91-1177, 1991.

135. Zienkiewicz, O. C., "The Finite Element Method"

136. Jones, R. M., "Mechanics of Composite Materials"

137. Wilson, E. L., Farhoomand, I., Bathe, K. J., "Nonlinear dynamic analysis of complex structures", Earthquake Engg. and Structural Dyn., 1, 1973, pp. 241-252.

138. Kinderman, A. J., Ramage, J. G., "Computer generation of normal random variables", J. Amer. Statistical Assn., 71(356), 1976, pp. 893-896.

139. Press, W. H., Flannery, B. P., Teukolsky, S. A., Vetterling, W. T., "Numerical Recipes - The Art of Scientific Computing"

140. Hardin, J. C., "Introduction to Time-Series Analysis", NASA Reference publication 1145

141. Hughes, T. R., Caughey, T. K., Liu, W. K., "Finite element methods for nonlinear elastodynamics which conserve energy", J. Appl. Mech, 45, 1978, pp. 366-370.

142. Hamdan, S. M., Patampongs, N., "Stability and convergence of some finite element algorithms for nonlinear elastodynamics", Int. J. Num. Meth. Engg., 21, 1985, 975-999.

143. Robinson, J. H., "Finite element formulation and numerical simulation of the large deflection random vibration of laminated composite plates", M.S. Thesis, Old Dominion University, 1990.

144. Locke, J. E., "A finite element formulation for the large deflection random response of thermally buckled structures", PhD Dissertation, Old Dominion University, 1988.

145. Istenes, R. R., "Comparison of experimental and analytical thermal deflections of composite panels with non-uniform temperature distributions", submitted to SDM '95.

Appendix A

Finite Element Shape Functions

The Lagrangian quadratic interpolation functions for a 9-node quadrilateral isoparametric element are listed below [135]. The variables ξ, η are natural coordinates whose range is $-1 \leq (\xi, \eta) \leq 1$. They are defined such that

$$(x, y) = \sum_{i=1}^{9} (x_i, y_i) N_i \qquad (u, v, w, \psi_x, \psi_y) = \sum_{i=1}^{9} (a_i^u, a_i^v, a_i^w, a_i^{\psi_x}, a_i^{\psi_y}) N_i$$

are valid transformations.

$$\begin{aligned}
N_1 &= \frac{1}{4}(1-\xi)(1-\eta)\xi\eta \\
N_2 &= -\frac{1}{2}(1-\xi^2)(1-\eta)\eta \\
N_3 &= -\frac{1}{4}(1+\xi)(1-\eta)\xi\eta \\
N_4 &= -\frac{1}{2}(1-\xi)(1-\eta^2)\xi \\
N_5 &= (1-\xi^2)(1-\eta^2) \\
N_6 &= \frac{1}{2}(1+\xi)(1-\eta^2)\xi \\
N_7 &= -\frac{1}{4}(1-\xi)(1+\eta)\xi\eta \\
N_8 &= \frac{1}{2}(1-\xi^2)(1+\eta)\eta \\
N_9 &= \frac{1}{4}(1+\xi)(1+\eta)\xi\eta
\end{aligned}$$

Appendix B

Formation of Element Matrices

Mass matrix

This matrix is detailed first. The inertias, I, and shape functions, N_i, have been defined earlier (Chapter 2 and Appendix A).

$$[M]\{\ddot{a}\} = \sum^{elements} [M^e]\{\ddot{a}^e\} =$$

$$\sum^{elements} \begin{bmatrix} m^{mm} & 0 & 0 \\ 0 & m^{ww} & 0 \\ 0 & 0 & m^{\psi\psi} \end{bmatrix} \begin{Bmatrix} \ddot{a}^m \\ \ddot{a}^w \\ \ddot{a}^\psi \end{Bmatrix} = \tag{1}$$

$$\sum^{elements} \int_{\Omega^e} \begin{bmatrix} I_1 N_i N_j & 0 & 0 & 0 & 0 \\ 0 & I_1 N_i N_j & 0 & 0 & 0 \\ 0 & 0 & I_1 N_i N_j & 0 & 0 \\ 0 & 0 & 0 & I_3 N_i N_j & 0 \\ 0 & 0 & 0 & 0 & I_3 N_i N_j \end{bmatrix} d\Omega^e \begin{Bmatrix} \ddot{a}_j^u \\ \ddot{a}_j^v \\ \ddot{a}_j^w \\ \ddot{a}_j^{\psi_x} \\ \ddot{a}_j^{\psi_y} \end{Bmatrix}$$

where $i, j = 1, \ldots, 9$; Ω^e is the area over an element; $[M^e]$ is a 45×45 element mass matrix consisting of sub-matrices $[m^{mm}]$, $[m^{ww}]$ and $[m^{\psi\psi}]$. The element acceleration vector $\{\ddot{a}^e\}$ in turn consists of the corresponding sub-vectors $\ddot{a}^m$, $\ddot{a}^w$, and $\ddot{a}^\psi$. The global matrix, $[M]$ is of order N_{df}.

Load Vector

At a single time-step, say the n^{th} time-step, the global load vector is given by

$$\{ P^n(t) \} = \mathbf{p}_n(t) \sum^{elements} \int_{\Omega^e} \begin{Bmatrix} 0 \\ 0 \\ N_i \\ 0 \\ 0 \end{Bmatrix} d\Omega^e$$

$$= \mathbf{p}_n(t) \sum^{elements} \{ F^e \} = \mathbf{p}_n(t) \{ F \} \tag{2}$$

where $\mathbf{p}_n(t)$ is the magnitude of the pressure distribution at the n^{th} time-step. The vector $\{ F \}$ is a global vector of length N_{df}, representing unit pressure acting over the surface of the plate. The final form $\{ P(t) \}$ is also of length N_{df}.

Note that of the 5 degrees of freedom per node, all terms for integration within an element (for the element load vector) except the one corresponding to the a^w degree of freedom are set to zero. Load in the transverse direction is the only one being treated in this work.

Linear Stiffness Matrices

The terms in Eq.(2.4.10) generate the following submatrices at the element level. Indices $p, r, s, t = 1, \ldots, 9$ and $l, k = 1, \ldots, 18$.

$$\int_{\Omega^e} A_{ij} \epsilon_j^m \delta\epsilon_i^m \, d\Omega^e$$

$$= \int_{\Omega^e} A_{ij} C_{il} C_{jk} \, d\Omega^e \; a_k^m \, \delta a_l^m$$

$$= k_{lk}^{mm} \, a_k^m \, \delta a_l^m \tag{3}$$

$$\int_{\Omega^e} A_{ij}\epsilon_j^o \delta\epsilon_i^m \, d\Omega^e$$

$$= \int_{\Omega^e} A_{ij} C_{il} C_{jp}^o \, d\Omega^e \; a_p^w \, \delta a_l^m$$

$$= k_{lp}^{mo} \, a_p^w \, \delta a_l^m \tag{4}$$

and

$$\int_{\Omega^e} B_{ij}\kappa_j \delta\epsilon_i^m \, d\Omega^e$$

$$= \int_{\Omega^e} B_{ij} C_{il} C_{jk} \, d\Omega^e \; a_k^\psi \, \delta a_l^m$$

$$= k_{lk}^{m\psi} \, a_k^\psi \, \delta a_l^m \tag{5}$$

correspond to δa_l^m rows, with a_l^m including a_p^u, a_p^v. Similarly, a_l^ψ includes $a_p^{\psi_x}$ and $a_p^{\psi_y}$.

$$\int_{\Omega^e} N_i^s \, \delta\epsilon_i^w \, d\Omega^e$$

$$= \int_{\Omega^e} N_i^s C_{irs}^w \, d\Omega^e \; \delta(a_r^w a_s^w)$$

$$= \int_{\Omega^e} N_i^s C_{irs}^w \, d\Omega^e \; (\delta a_r^w a_s^w + a_r^w \delta a_s^w)$$

$$= [\bar{k}_{rs}^{ws} + \bar{k}_{sr}^{ws}] a_s^w \, \delta a_r^w$$

$$= k_{rs}^{ws} a_s^w \, \delta a_r^w \tag{6}$$

and

$$\int_{\Omega^e} N_i^{\Delta T}\, \delta\epsilon_i^w\, d\Omega^e$$

$$= \int_{\Omega^e} N_i^{\Delta T} C_{irs}^w\, d\Omega^e\, \delta(a_r^w a_s^w)$$

$$= \int_{\Omega^e} N_i^{\Delta T} C_{irs}^w\, d\Omega^e\, (\delta a_r^w a_s^w + a_r^w \delta a_s^w)$$

$$= [\bar{k}_{rs}^{w\Delta T} + \bar{k}_{sr}^{w\Delta T}] a_s^w\, \delta a_r^w$$

$$= k_{rs}^{w\Delta T} a_s^w\, \delta a_r^w \tag{7}$$

are linear matrices corresponding to δa_r^w rows.

$$\int_{\Omega^e} A_{ij} \epsilon_j^m\, \delta\epsilon_i^o\, d\Omega^e$$

$$= \int_{\Omega^e} A_{ij} C_{ir}^o C_{jk}\, d\Omega^e\, a_k^m\, \delta a_r^w$$

$$= k_{rk}^{om}\, a_k^m\, \delta a_r^w \tag{8}$$

where $[k^{om}]$ is the transpose of the matrix in Eq.(4),

$$\int_{\Omega^e} A_{ij} \epsilon_j^o \delta\epsilon_i^o\, d\Omega^e$$

$$= \int_{\Omega^e} A_{ij} C_{ir}^o C_{jp}^o\, d\Omega^e\, a_p^w\, \delta a_r^w$$

$$= k_{rp}^{oo}\, a_p^w\, \delta a_r^w \tag{9}$$

and

$$\int_{\Omega^e} B_{ij}\kappa_j \delta\epsilon_i^o \, d\Omega^e$$

$$= \int_{\Omega^e} B_{ij} C_{ir}^o C_{jk} \, d\Omega^e \; a_k^\psi \, \delta a_r^w$$

$$= k_{rk}^{o\psi} \, a_k^\psi \, \delta a_r^w \tag{10}$$

all from w_o, correspond to δa_r^w rows.

$$\int_{\Omega^e} B_{ij}\epsilon_j^m \delta\kappa_i \, d\Omega^e$$

$$= \int_{\Omega^e} B_{ij} C_{il} C_{jk} \, d\Omega^e \; a_k^m \, \delta a_l^\psi$$

$$= k_{lk}^{\psi m} \, a_k^m \, \delta a_l^\psi \tag{11}$$

where $[k^{\psi m}]$ is the transpose of the matrix in Eq.(5),

$$\int_{\Omega^e} B_{ij}\epsilon_j^o \delta\kappa_i \, d\Omega^e$$

$$= \int_{\Omega^e} B_{ij} C_{il} C_{jp} \, d\Omega^e \; a_p^w \, \delta a_l^\psi$$

$$= k_{lp}^{\psi o} \, a_p^w \, \delta a_l^\psi \tag{12}$$

where $[k^{\psi o}]$ is the transpose of the matrix in Eq.(10), and

$$\int_{\Omega^e} D_{ij}\kappa_j \delta\kappa_i \, d\Omega^e$$

$$= \int_{\Omega^e} D_{ij} C_{il} C_{jk} \, d\Omega^e \; a_k^\psi \, \delta a_l^\psi$$

$$= k_{lk}^{\psi\psi} \, a_k^\psi \, \delta a_l^\psi \tag{13}$$

correspond to δa_l^ψ rows. Linear matrices from shear energy terms are

$$\int_{\Omega^e} \mathcal{K}^2 A_{mn} \gamma_n^\psi \delta\gamma_m^\psi \, d\Omega^e$$

$$= \int_{\Omega^e} \mathcal{K}^2 A_{mn} B_{ml}^\psi B_{nk}^\psi \, d\Omega^e \; a_k^\psi \, \delta a_l^\psi$$

$$= ks_{lk}^{\psi\psi} \, a_k^\psi \, \delta a_l^\psi \tag{14}$$

$$\int_{\Omega^e} \mathcal{K}^2 A_{mn} \gamma_n^w \delta\gamma_m^\psi \, d\Omega^e$$

$$= \int_{\Omega^e} \mathcal{K}^2 A_{mn} B_{ml}^\psi B_{np}^w \, d\Omega^e \; a_p^w \, \delta a_l^\psi$$

$$= ks_{lp}^{\psi w} \, a_p^w \, \delta a_l^\psi \tag{15}$$

$$\int_{\Omega^e} \mathcal{K}^2 A_{mn} \gamma_n^{\psi} \delta\gamma_m^{w} \, d\Omega^e$$

$$= \int_{\Omega^e} \mathcal{K}^2 A_{mn} B_{nk}^{\psi} B_{mr}^{w} \, d\Omega^e \; a_k^{\psi} \, \delta a_r^{w}$$

$$= ks_{rk}^{w\psi} \, a_k^{\psi} \, \delta a_r^{w} \tag{16}$$

where $[ks^{w\psi}]$ is the transpose of the matrix in Eq.(15), and

$$\int_{\Omega^e} \mathcal{K}^2 A_{mn} \gamma_n^{w} \delta\gamma_m^{w} \, d\Omega^e$$

$$= \int_{\Omega^e} \mathcal{K}^2 A_{mn} B_{mr}^{w} B_{np}^{w} \, d\Omega^e \; a_p^{w} \, \delta a_r^{w}$$

$$= ks_{rp}^{ww} \, a_p^{w} \, \delta a_r^{w} \tag{17}$$

Nonlinear Stiffness Matrices

Other than one second-order term which is a cubic function of $\{a^w\}$, all the other nonlinear energy expressions are first-order terms, quadratically dependent on $\{a^w\}$. These are all listed below.

$$\int_{\Omega^e} A_{ij} \epsilon_j^{w} \delta\epsilon_i^{m} \, d\Omega^e$$

$$= \int_{\Omega^e} \frac{1}{2} A_{ij} (C_{jps}^{w} + C_{jsp}^{w}) C_{il} \, d\Omega^e \; a_p^{w} a_s^{w} \, \delta a_l^{m}$$

$$= k1_{lps}^{mw} a_p^{w} \, a_s^{w} \, \delta a_l^{m} \tag{18}$$

corresponds to δa_l^m rows. The nonlinear strain tensor C_{jps}^w has been made symmetric to be consistent with $w_{,x}\, w_{,y} = w_{,y}\, w_{,x}$.

$$\int_{\Omega^e} A_{ij}\epsilon_j^m \delta\epsilon_i^w \, d\Omega^e$$

$$= \int_{\Omega^e} A_{ij} C_{jk} C_{irs}^w \, d\Omega^e \; a_k^m \, \delta(a_r^w a_s^w)$$

$$= \int_{\Omega^e} A_{ij} C_{jk} C_{irs}^w \, d\Omega^e \; a_k^m \, (a_r^w \delta a_s^w + a_s^w \delta a_r^w)$$

$$= [\bar{k}_{rsk}^{wm} + \bar{k}_{srk}^{wm}] a_s^w \; a_k^m \, \delta a_r^w$$

$$= k1_{rsk}^{wm} a_s^w \; a_k^m \, \delta a_r^w \tag{19}$$

This is twice the transpose of $k1_{lps}^{mw}$. The second-order nonlinear function of $\{a^w\}$ is given by,

$$\int_{\Omega^e} A_{ij}\epsilon_j^w \delta\epsilon_i^w \, d\Omega^e$$

$$= \int_{\Omega^e} A_{ij} C_{jpt}^w C_{irs}^w \, d\Omega^e \; a_p^w a_t^w \, \delta(a_r^w a_s^w)$$

$$= \int_{\Omega^e} A_{ij} C_{jpt}^w C_{irs}^w \, d\Omega^e \; a_p^w a_t^w \, (\delta a_r^w a_s^w + a_r^w \delta a_s^w)$$

$$= [\bar{k}_{rspt}^{ww} + \bar{k}_{srtp}^{ww}] a_s^w a_p^w \; a_t^w \, \delta a_r^w$$

$$= k2_{rspt}^{ww} a_s^w a_p^w \; a_t^w \, \delta a_r^w \tag{20}$$

The other first-order functions of $\{a^w\}$ are,

$$\int_{\Omega^e} A_{ij}\epsilon^o_j \delta\epsilon^w_i \, d\Omega^e$$

$$= \int_{\Omega^e} A_{ij} C^o_{jp} C^w_{irs} \, d\Omega^e \; a^w_p \, \delta(a^w_r a^w_s)$$

$$= \int_{\Omega^e} A_{ij} C^o_{jp} C^w_{irs} \, d\Omega^e \; a^w_p \, (a^w_r \delta a^w_s + a^w_s \delta a^w_r)$$

$$= [\bar{k}^{wo}_{rsp} + \bar{k}^{wo}_{srp}] a^w_s \; a^w_p \; \delta a^w_r$$

$$= k1^{wo}_{rsp} a^w_s \; a^w_p \; \delta a^w_r \qquad (21)$$

$$\int_{\Omega^e} B_{ij}\kappa_j \delta\epsilon^w_i \, d\Omega^e$$

$$= \int_{\Omega^e} B_{ij} C_{jk} C^w_{irs} \, d\Omega^e \; a^\psi_k \, \delta(a^w_r a^w_s)$$

$$= \int_{\Omega^e} B_{ij} C_{jk} C^w_{irs} \, d\Omega^e \; a^\psi_k \, (a^w_r \delta a^w_s + a^w_s \delta a^w_r)$$

$$= [\bar{k}^{w\psi}_{rsk} + \bar{k}^{w\psi}_{srk}] a^w_s \; a^\psi_k \; \delta a^w_r$$

$$= k1^{w\psi}_{rsk} a^w_s \; a^\psi_k \; \delta a^w_r \qquad (22)$$

and

$$\int_{\Omega^e} A_{ij}\epsilon_j^w \delta\epsilon_i^o \, d\Omega^e$$

$$= \int_{\Omega^e} \frac{1}{2} A_{ij}(C_{jps}^w + C_{jsp}^w)C_{ir}^o \, d\Omega^e \; a_p^w a_s^w \, \delta a_r^w$$

$$= [k1_{rps}^{ow} a_s^w] \, a_p^w \, \delta a_r^w \tag{23}$$

As in an earlier relation, $k1_{rps}^{ow}$ is half the transpose of $k1_{rsp}^{wo}$. And

$$\int_{\Omega^e} B_{ij}\epsilon_j^w \delta\kappa_i \, d\Omega^e$$

$$= \int_{\Omega^e} \frac{1}{2} B_{ij}(C_{jps}^w + C_{jsp}^w)C_{il} \, d\Omega^e \; a_p^w a_s^w \, \delta a_l^\psi$$

$$= [k1_{lps}^{\psi w} a_s^w] \, a_p^w \, \delta a_l^\psi \tag{24}$$

is half the transpose of $k1_{rsk}^{w\psi}$. This term corresponds to δa_l^ψ rows.

The constant terms in the strain energy are

$$\int_{\Omega^e} N_i^s \, \delta\epsilon_i^m \, d\Omega^e$$

$$= \int_{\Omega^e} N_i^s \, C_{il} \, \delta a_l^m \, d\Omega^e$$

$$= p_l^{ms} \, \delta a_l^m \tag{25}$$

$$\int_{\Omega^e} N_i^{\Delta T}\, \delta\epsilon_i^m \, d\Omega^e$$

$$= \int_{\Omega^e} N_i^{\Delta T}\, C_{il}\, \delta a_l^m \, d\Omega^e$$

$$= p_l^{m\Delta T}\, \delta a_l^m \tag{26}$$

$$\int_{\Omega^e} N_i^s \, \delta\epsilon_i^o \, d\Omega^e$$

$$= \int_{\Omega^e} N_i^o \, C_{ir}^o \, \delta a_r^w \, d\Omega^e$$

$$= p_r^{os}\, \delta a_r^w \tag{27}$$

$$\int_{\Omega^e} N_i^{\Delta T}\, \delta\epsilon_i^o \, d\Omega^e$$

$$= \int_{\Omega^e} N_i^{\Delta T}\, C_{ir}^o \, \delta a_r^w \, d\Omega^e$$

$$= p_r^{o\Delta T}\, \delta a_r^w \tag{28}$$

and

$$\int_{\Omega^e} M_i^{\Delta T}\, \delta\kappa_i \, d\Omega^e$$

$$= \int_{\Omega^e} M_i^{\Delta T} C_{il} \delta a_l^{\psi} \, d\Omega^e$$

$$= p_l^{\psi \Delta T} \delta a_l^{\psi} \tag{29}$$

Eqs.(3-29) can be put in a matrix form at the element level as follows

$$\left(\begin{bmatrix} k^{mm} & k^{mo} & k^{m\psi} \\ k^{om} & k^{oo} + ks^{ww} & k^{o\psi} + ks^{w\psi} \\ k^{\psi m} & k^{\psi o} + ks^{\psi w} & k^{\psi\psi} + ks^{\psi\psi} \end{bmatrix} + \begin{bmatrix} 0 & 0 & 0 \\ 0 & k^{ws} & 0 \\ 0 & 0 & 0 \end{bmatrix} \right.$$

$$- \begin{bmatrix} 0 & 0 & 0 \\ 0 & k^{w\Delta T} & 0 \\ 0 & 0 & 0 \end{bmatrix} + \begin{bmatrix} 0 & [k1^{mw}]\{a^w\} & 0 \\ [k1^{wm}]\{a^w\} & [k1^{wo} + k1^{ow}]\{a^w\} & [k1^{w\psi}]\{a^w\} \\ 0 & [k1^{\psi w}]\{a^w\} & 0 \end{bmatrix}$$

$$\left. + \begin{bmatrix} 0 & 0 & 0 \\ 0 & [k2^{ww}]\{a^w\}\{a^w\} & 0 \\ 0 & 0 & 0 \end{bmatrix} \right) \begin{Bmatrix} a^m \\ a^w \\ a^{\psi} \end{Bmatrix} + \begin{Bmatrix} p^{ms} \\ p^{os} \\ 0 \end{Bmatrix} - \begin{Bmatrix} p^{m\Delta T} \\ p^{o\Delta T} \\ p^{\psi\Delta T} \end{Bmatrix} \tag{30}$$

where all matrices and tensors are of order 45.

The linear stiffness matrix above is completely symmetric and so is the second-order nonlinear matrix. The submatrices corresponding to the $\{a^m\}$ and $\{a^{\psi}\}$ rows in the first-order matrix $[k1]$ (12 and 32 positions) are transposes and half of the submatrices in the corresponding transpose positions of $[k1]$ (21 and 23 positions). The rest of the submatrices are symmetric. Thus, at the global assembled level we now have

$$\sum^{elements} \Big([M^e]\{\ddot{a}^e\} + [C^e]\{\dot{a}^e\} + [K^e + K^{se} - K^{\Delta T e}]\{a^e\} + [K1^e]\{a^e\}\{a^e\}$$

$$+ [K2^e]\{a^e\}\{a^e\}\{a^e\} + \{P^{se}\} - \{P^{\Delta T e}\} \Big)$$

$$= \mathbf{p(t)} \sum^{elements} \{F^e\} \tag{31}$$

which results in the equation of motion

$$
\begin{aligned}
&[M]\{\ddot{a}\} + [C]\{\dot{a}\} + [K + K^s - K^{\Delta T}]\{a\} + [K1]\{a\}\{a\} \\
&+ [K2]\{a\}\{a\}\{a\} + \{P^s\} - \{P^{\Delta T}\} \\
&= \{P(t)\}
\end{aligned}
\tag{32}
$$

as in Eq.(2.5.1). This system is of order N_{df}.

Appendix C

Numerical Integration of Modal Equations

To proceed with deriving the nonlinear algebraic equations, the weighted integral of the modal system of equations within one time-step is rewritten below. Note that $p_i(t)$ between the two time-steps, t_{n+1} and t_n, has been replaced by $\bar{p}_i^n(t)$ as in Eq.(3.1.8). The time subscripts n and $(n+1)$ are used as superscripts for subscripted variables.

$$\int_{t_n}^{t_{n+1}} W(\tau) \Big\{ m_{ij}\ddot{q}_j^{n+1} + c_{ij}\dot{q}_j^{n+1} + \left(k_{ij} + k_{ij}^s - k_{ij}^{\Delta T}\right) q_j^{n+1}$$

$$+ \; k1_{ijk}\, q_j^{n+1} q_k^{n+1} + k2_{ijkl}\, q_j^{n+1} q_k^{n+1} q_l^{n+1} + \bar{p}_i(t) + p_i^o - p_i^{\Delta T} \Big\}\, d\tau = 0 \quad (1)$$

Each one of the terms in the integrand will now be integrated in the manner of Eq.(3.1.5). The integration of the inertia term upon substitution of Eqs.(3.1.3) is as follows

$$\frac{\int_{t_n}^{t_{n+1}} W(\tau)\, m_{ij}\, \ddot{q}_j^{n+1}\, d\tau}{\int_{t_n}^{t_{n+1}} W(\tau)\, d\tau}$$

$$= \frac{\int_{t_n}^{t_{n+1}} W(\tau)\, m_{ij} \left(\ddot{q}_j^n + \alpha_j^{(3)\,n} \tau\right) d\tau}{\int_{t_n}^{t_{n+1}} W(\tau)\, d\tau}$$

$$= m_{ij}\left(\ddot{q}_j^n + \alpha_j^{(3)n}\theta_1\Delta t\right)$$

$$= m_{ij}\left(\ddot{\tilde{q}}_j^n + \frac{6\theta_W}{\Delta t^2}d_j^n\right) \tag{2}$$

where d_j^n and $\alpha_j^{(3)n}$ are related as in Eq.(3.1.9). The free parameter θ_1 has been written in terms of the Wilson-θ parameter, θ_W, as defined in Eqs.(3.1.7).

In the same way, the damping term gives

$$\frac{\int_{t_n}^{t_{n+1}} W(\tau)\, c_{ij}\, \dot{q}_j^{n+1}\, d\tau}{\int_{t_n}^{t_{n+1}} W(\tau)\, d\tau}$$

$$= \frac{\int_{t_n}^{t_{n+1}} W(\tau)\, c_{ij}\left(\dot{q}_j^n + \ddot{q}_j^n\tau + \alpha_j^{(3)n}\tau^2/2\right) d\tau}{\int_{t_n}^{t_{n+1}} W(\tau)\, d\tau}$$

$$= c_{ij}\left(\dot{q}_j^n + \ddot{q}_j^n\,\theta_1\Delta t + \alpha_j^{(3)n}\,\theta_2\frac{\Delta t^2}{2}\right)$$

$$= c_{ij}\left(\dot{\tilde{q}}_j^n + \frac{3\theta_W^2}{\Delta t}d_j^n\right) \tag{3}$$

Note that the usage of $\dot{\tilde{q}}_j^n$ here includes the Wilson-θ parameter with $\theta_1 = \theta_W$. Similarly, the linear modal stiffness matrices together generate

$$\frac{\int_{t_n}^{t_{n+1}} W(\tau)\left[k_{ij} + k_{ij}^s - k_{ij}^{\Delta T}\right] q_j^{n+1}\, d\tau}{\int_{t_n}^{t_{n+1}} W(\tau)\, d\tau}$$

$$= \frac{\int_{t_n}^{t_{n+1}} W(\tau)\left[k_{ij} + k^s_{ij} - k^{\Delta T}_{ij}\right]\left(q^n_j + \dot{q}^n_j\tau + \ddot{q}^n_j\tau^2/2 + \alpha^{(3)\,n}_j\tau^3/6\right)d\tau}{\int_{t_n}^{t_{n+1}} W(\tau)\,d\tau}$$

$$= \left[k_{ij} + k^s_{ij} - k^{\Delta T}_{ij}\right]\left(q^n_j + \dot{q}^n_j\theta_1\Delta t + \ddot{q}^n_j\theta_2\frac{\Delta t^2}{2} + \alpha^{(3)\,n}_j\theta_3\frac{\Delta t^3}{6}\right)$$

$$= \left[k_{ij} + k^s_{ij} - k^{\Delta T}_{ij}\right]\left(\tilde{q}^n_j + \theta^3_W d^n_j\right) \tag{4}$$

Here again $\tilde{q}^n_j$ includes $\theta_1 = \theta_W$ and $\theta_2 = \theta^2_W$ in its expression. The $\{\tilde{\mathbf{q}}\}$ terms in Eqs.(2), (3) and (4) above, contribute to $A0_i$ and the d^n terms to A_{ij}.

The quadratic and cubic tensor terms will be dealt with next. When using Eqs.(3.1.7) for the free parameters after integration, θ_W and Δt occur together with like powers. This will be used in organizing the many terms as constant, linear, quadratic and cubic expressions of d^n.

The first-order nonlinear tensor term, thus results in

$$\frac{\int_{t_n}^{t_{n+1}} W(\tau)\,k1_{ijk}\,q^{n+1}_j q^{n+1}_k\,d\tau}{\int_{t_n}^{t_{n+1}} W(\tau)\,d\tau}$$

$$= \frac{\int_{t_n}^{t_{n+1}} W(\tau)\,k1_{ijk}\times}{\int_{t_n}^{t_{n+1}} W(\tau)\,d\tau}$$

$$\underline{\left(q^n_j + \dot{q}^n_j\tau + \ddot{q}^n_j\tau^2/2 + \alpha^{(3)\,n}_j\tau^3/6\right)\left(q^n_k + \dot{q}^n_k\tau + \ddot{q}^n_k\tau^2/2 + \alpha^{(3)\,n}_k\tau^3/6\right)d\tau}$$

$$= \left\{k1_{ijk}\left(q^n_j + \dot{q}^n_j\theta_W\Delta t + \ddot{q}^n_j\theta^2_W\frac{\Delta t^2}{2}\right)\left(q^n_k + \dot{q}^n_k\theta_W\Delta t + \ddot{q}^n_k\theta^2_W\frac{\Delta t^2}{2}\right)\right.$$

which are all constant terms contributing to $A0_i$,

$$+ k1_{ijk}\left[d_j^n\theta_W^3\left(q_k^n + \dot{q}_k^n\theta_W\Delta t + \ddot{q}_k^n\theta_W^2\frac{\Delta t^2}{2}\right) + d_k^n\theta_W^3\left(q_j^n + \dot{q}_j^n\theta_W\Delta t + \ddot{q}_j^n\theta_W^2\frac{\Delta t^2}{2}\right)\right]$$

which are linear terms contributing to A_{ij},

$$+ k1_{ijk}\, d_j^n d_k^n\, \theta_W^6\Bigg\} \tag{5}$$

which is the quadratic term from $k1_{ijk}$ contributing to $A1_{ijk}$.

In equation (5)

$$k1_{ijk}\left[d_j^n\theta_W^3\left(q_k^n + \dot{q}_k^n\theta_W\Delta t + \ddot{q}_k^n\theta_W^2\frac{\Delta t^2}{2}\right) + d_k^n\theta_W^3\left(q_j^n + \dot{q}_j^n\theta_W\Delta t + \ddot{q}_j^n\theta_W^2\frac{\Delta t^2}{2}\right)\right]$$

$$= \left(k1_{ijk} + k1_{ikj}\right)d_j^n\theta_W^3\left(q_k^n + \dot{q}_k^n\theta_W\Delta t + \ddot{q}_k^n\theta_W^2\frac{\Delta t^2}{2}\right) \tag{6}$$

This property will be directly used in case of the second-order tensor whose integration gives

$$\frac{\int_{t_n}^{t_{n+1}} W(\tau)\, k2_{ijkl}\, q_j^{n+1} q_k^{n+1} q_l^{n+1}\, d\tau}{\int_{t_n}^{t_{n+1}} W(\tau)\, d\tau}$$

$$= \frac{\int_{t_n}^{t_{n+1}} W(\tau)\, k2_{ijkl}\Big[\left(q_j^n + \dot{q}_j^n\tau + \ddot{q}_j^n\tau^2/2 + \alpha_j^{(3)\,n}\tau^3/6\right)\times}{\int_{t_n}^{t_{n+1}} W(\tau)\, d\tau}$$

$$\left(q_k^n + \dot{q}_k^n\tau + \ddot{q}_k^n\tau^2/2 + \alpha_k^{(3)\,n}\tau^3/6\right)\left(q_l^n + \dot{q}_l^n\tau + \ddot{q}_l^n\tau^2/2 + \alpha_l^{(3)\,n}\tau^3/6\right)\Big]d\tau$$

$$= \Bigg\{k2_{ijkl}\left(q_j^n + \dot{q}_j^n\theta_W\Delta t + \ddot{q}_j^n\theta_W^2\frac{\Delta t^2}{2}\right)\times$$

$$\left(q_k^n + \dot{q}_k^n\theta_W\Delta t + \ddot{q}_k^n\theta_W^2\frac{\Delta t^2}{2}\right)\left(q_l^n + \dot{q}_l^n\theta_W\Delta t + \ddot{q}_l^n\theta_W^2\frac{\Delta t^2}{2}\right)$$

which are constant terms contributing to $A0_i$,

$$+ \left(k2_{ijkl} + k2_{iljk} + k2_{iklj}\right) d_j^n \theta_W^3 \times$$

$$(q_k^n + \dot{q}_k^n \theta_W \Delta t + \ddot{q}_k^n \theta_W^2 \frac{\Delta t^2}{2})(q_l^n + \dot{q}_l^n \theta_W \Delta t + \ddot{q}_l^n \theta_W^2 \frac{\Delta t^2}{2})$$

which are linear terms contributing to A_{ij},

$$+ \left(k2_{ijkl} + k2_{iljk} + k2_{iklj}\right) d_j^n d_k^n \theta_W^6 \times$$

$$(q_l^n + \dot{q}_l^n \theta_W \Delta t + \ddot{q}_l^n \theta_W^2 \frac{\Delta t^2}{2})$$

which are quadratic terms contributing to $A1_{ijk}$,

$$+ k2_{ijkl}\, d_j^n d_k^n d_l^n \theta_W^9 \Bigg\} \tag{7}$$

which is cubic in d^n and gives $A2_{ijkl}$.

The rest of the terms in (1) are not dependent on τ and hence remain unchanged. They add to $A0_i$ to form

$$A0_i \equiv A0_i\left(\{\tilde{\mathbf{q}}\}, \bar{p}, p^o, p^{\Delta T}\right) \tag{8}$$

The vector $A0_i$ remains unchanged with iterations and is only updated at every successive time-step.

Therefore, grouping all the above terms as cubic, quadratic, linear and constant in d^n, we arrive at

$$A2_{ijkl}\, d_j^n d_k^n d_l^n + A1_{ijk}\, d_j^n d_k^n + A_{ij}\, d_j^n + A0_i \equiv \Psi_i(d) = 0 \tag{9}$$